# Control of an Electronic Power Steering system for people with reduced mobility

Valentina Ciarla

UNIVERSITÉ DE GRENOBLE

# THÈSE

Pour obtenir le grade de

## DOCTEUR DE L'UNIVERSITÉ DE GRENOBLE

Spécialité : **Automatique-Productique**

Arrêté ministériel : 7 août 2006

Présentée par


## Valentina CIARLA


Thèse dirigée par **M. Carlos CANUDAS DE WIT**
et codirigée par **M. Franck QUAINE et Mme. Violaine CAHOUET**

préparée au sein **GIPSA-Lab, Département Automatique**
et de **Électronique, Électrotechnique, Automatique, Traitement du Signal**

# Commande d'un système de puissance électrique pour de personne à mobilité réduite

Thèse soutenue publiquement le **10 Octobre 2013**,
devant le jury composé de :

**M., Michel Basset**
Professeur, Université de Haute Alsace, Président
**M., Xavier Moreau**
Professeur, Université Bordeaux 1, Rapporteur
**M., Philippe Gorce**
Professeur, Université du Sud Toulon, Invité
**Mme., Violaine Cahouet**
Maître de Conférences UJF, Encadrant
**M., Franck Quaine**
Maître de Conférences UJF, Encadrant

# Acknowledgements

This thesis is the result of several exchanges: technical, scientific and personal.
First, I am deeply grateful with my advisors Carlos Canudas de Wit, Violaine Cahouet and Franck Quaine. Orientation and support, that I received during these years were fundamental for my research.
I also feel grateful for the privilege of knowing and collaborating with many other people in Gipsa Lab, who became friends over the last three years.
Thanks to Gipsa Lab and the ANR VolHand for helping me to carry out my doctoral research and for their financial support.
Finally, I thank the members of my close family: my parents, my uncles and my hunts for their love and support.

*To my beloved family.*

”J’ai consacré ma vie entière à l’automobile,
ce triomphe de la liberté pour l’homme.”
Enzo Ferrari

# Table of contents

# List of Acronyms

**ANR** Agence Nationale de la Recherche

**CNRS** Centre National de la Recherche Scientifique

**CNSA** Caisse Nationale de Solidarité pour l'Autonomie

**CoG** Center of Gravity

**DACB** Data Acquisition and Control Buffer

**EHPS** Electro-Hydraulic Power Steering

**EMG** Electromyography

**EPAS** Electronic Power Assistance Steering

**EPS** Electronic Power Steering

**FFT** Fast Fourier Transform

**HIL** Hardware In the Loop

**HPAS** Hydraulic Power Assisted Steering

**INP** Institut Polytechnique de Grenoble

**INRIA** Institut National de Recherche en Informatique et en Automatique

**MVC** Maximum Voluntary Contraction

**LQ** Linear Quadratic

**NeCS** Network Control System

**PRBS** Pseudo-Random Binary Sequence

**PI** Proportional Integrative

**PID** Proportional Integral Derivative

**PD** Proportional Derivative

**RTX** Real Time eXecution

# French summary

Ce travail de thèse a été effectué au sein du Laboratoire GIPSA-Lab de Grenoble, sous la direction de Carlos Canudas de Wit et co-encadré par Franck Quaine et Violaine Cahouet. Ce travail a été réalisé dans le cadre du projet ANR-09-VTT-14-01/06 VolHand. Il s'inscrit dans le contexte général des nouvelles générations de Direction Assistée électrique (DAE, ou EPAS en anglais pour Electronic Power Assistance Steering) avec pour objectif spécifique de tenir compte des caractéristiques des conducteurs à mobilité réduite.

En effet, à ce jour, il n'existe pas de système de direction assistée adapté aux capacités articulaires (rhumatismes divers), musculaires (diminution de force, sénescence), ou encore aux douleurs ressenties par le conducteur, ce qui constitue une insuffisance dès lors que l'on s'intéresse à de telles populations. Le principal objectif de cette thèse est donc de proposer une méthodologie générale permettant d'adapter une DAE standard aux conducteurs à mobilité réduite.

En ce qui concerne le mémoire, il est organisé en cinq chapitres.

- **Chapitre 1**, intitulé **Context and objectives of the study**, présente, dans un premier temps le contexte, l'impact économique et sociétal, la problématique et l'objectif. Ensuite, la stratégie permettant d'atteindre l'objectif ainsi spécifié est précisée à travers l'organisation du mémoire où le contenu scientifique et méthodologique de chaque chapitre est résumé.
- **Chapitre 2**, intitulé **Models for simulation**, est dédié à l'établissement d'un modèle mathématique du système de direction assistée électrique prenant bien en compte l'élasticité en torsion de la colonne de direction due à la présence d'un capteur de couple.

  Parmi les entrées de ce modèle à deux degrés de liberté, et en raison de son influence importante sur le système de direction, une attention toute particulière est faite en ce qui concerne la description du couple de frottement du contact pneumatique-route. Ce couple résulte de la contribution de deux phénomènes principaux : la friction prépondérante aux basses vitesses du véhicule et l'auto-alignement prépondérant aux vitesses élevées. Un modèle de frottement dynamique, basé sur le modèle de LuGre, est développé pour décrire ces phénomènes. Une amélioration du modèle est propo-

sée en prenant en compte la vitesse du véhicule dans la formulation du couple pour vaincre les frottements selon l'axe z. Quelques simulations visant à vérifier la validité de l'amélioration apportée sont proposées pour différentes vitesses.

– **Chapitre 3**, intitulé **Oscillation annealing and torque observer design**, commence par mettre en évidence les conséquences de la présence du mode souple associé à l'élasticité en torsion du capteur de couple sur le ressenti au niveau du volant. Une commande LQ synthétisée à partir du modèle nominal de la direction est proposée pour limiter les oscillations dues à ce mode souple. En l'absence d'incertitude, les performances simulées obtenues pour l'état paramétrique nominal sont suffisamment satisfaisantes pour envisager par la suite (Chapitre 4) de négliger ce mode souple. Enfin, l'intérêt et la nécessité d'utiliser un observateur, notamment pour estimer le couple conducteur et le couple résultant du frottement pneumatique route, sont démontrés et illustrés en simulation pour l'état paramétrique nominal.
– **Chapitre 4**, intitulé **Power steering booster stage**, se focalise dans un premier temps sur la nature des courbes d'assistance utilisées dans le cadre des DAE. En effet, l'état de l'art sur le sujet met en évidence l'absence de justification de la forme de ces courbes généralement fonction de la vitesse du véhicule et du couple appliqué par le conducteur. L'étude de ces relations est très peu abordée dans la littérature et il résulte que, finalement, les lois actuelles ne font qu'imiter le comportement des premières assistances hydrauliques. Afin de proposer des lois plus génériques et réglables, à partir d'un état de l'art sur les critères liés au mouvement de l'humain, dans ce chapitre on propose de calculer de nouvelles lois en se fondant sur l'approche par optimisation (minimisation du jerk couplé avec la loi de puissance de Steven). Pour le modèle d'interface roue-sol, le modèle de Dahl est alors préféré à celui vu au chapitre 2, du fait de sa complexité. Une manoeuvre de parking, représentative de situation difficile pour les personnes à mobilité réduite, est d'abord retenue pour l'optimisation. Puis, la relation mathématique entre le couple exercé par le conducteur et l'assistance en couple fournie par l'EPAS est obtenue pour chacune des conditions de conduite stationnaire et transitoire. Les résultats obtenus montrent que la minimisation du critère fondé sur le jerk du volant et la loi de puissance de Steven peut permettre de reproduire les lois existantes d'assistance et leur apportent une justification. Ils confirment également la forte influence du frottement (couple) au niveau du contact roue-sol.
  La seconde partie de ce chapitre est consacrée au développement d'une méthodologie générale d'adaptation des lois d'assistance (cartographie standard initiale) aux exigences du conducteur à mobilité réduite (typiquement ici une personne présentant une asymétrie : 1 seul membre supérieur => cartographie modifiée). Afin d'estimer l'effort exercé sur le volant par le conducteur handicapé, une estimation de la masse du membre est nécessaire. Une méthode hors ligne est proposée à partir d'un modèle biomécanique du membre supérieur et de tables anthropométriques. Une formulation mathématique est alors proposée et une étude de son impact sur le modèle de conducteur est menée. Ces résultats sont utilisés pour pouvoir modifier les lois d'assistance

et ainsi compenser les déficiences musculaires.
Trois scénarii sont testés (manoeuvre de parking, vitesse stabilisée et évitement d'obstacle, à respectivement à 0 et 30 km/h) pour valider l'approche selon des critères définis sur le conducteur (respectivement énergie, force et précision). Les lois de commande sont ainsi activées en fonction de la vitesse du véhicule. Les résultats de simulation montrent l'intérêt de l'approche.

– **Chapitre 5**, intitulé **Experimental validation NeCS-Car benchmark**, commence par détailler la plateforme expérimentale présente au laboratoire GIPSA-LAB et utilisée pour évaluer et valider les nouvelles lois d'assistance adaptées au conducteur à mobilité réduite. Cette plateforme est de type Hardware-In-the-Loop (HIL). Elle permet, notamment, l'obtention d'un profil réel de couple de frottement pneumatique-route.
La plateforme NeCS-Car est d'abord décrite en précisant les différentes configurations possibles selon le choix d'intégration dans la simulation des composants virtuels ou réels. Puis, les adaptations nécessaires aux modèles pour être simulés sur le banc sont introduites. Pour pouvoir tester la stratégie d'assistance développée, les paramètres de viscosité et d'inertie du poste de conduite sont, ensuite, identifiés en comparant les résultats issus d'une réponse indicielle et ceux issus d'une SBPA donnant des résultats du même ordre de grandeur. Le système est testé en boucle ouverte pour vérifier la validité du modèle de la direction assistée puis en boucle fermée incluant l'observateur avec la stratégie de compensation des oscillations du chapitre 3, sur le banc HIL (poste de conduite réel avec interface roue-sol simulée).
Les résultats obtenus sont analysés pour montrer la validité des hypothèses faites et des simulations obtenues au chapitre 3. Afin de vérifier la performance du modèle d'interface roue-sol, l'observateur est à nouveau testé en incluant le véhicule NeCS dans la boucle. Finalement, la stratégie globale d'assistance de couple au volant pour un conducteur présentant une asymétrie, est testée sur le banc avec la NeCS-Car. Pour cela une nouvelle procédure d'estimation en ligne de la masse du membre supérieur est proposée. Les résultats issus du protocole montrent des premiers résultats intéressants. Les précédents scénarii sont testés et les résultats présentés montrent la validité de la stratégie proposée.

Ce mémoire se termine avec une partie **General conclusions and perspectives** où les principales contributions sont d'abord rappelées, puis où des perspectives pour compléter et prolonger ce travail sont proposées.

Quant à la production scientifique qui accompagne ce mémoire, elle est principalement composée de 2 communications (1 en 2011 et 1 en 2012) dans des conférences internationales IEEE avec actes et comité de lecture, ainsi que 5 rapports d'étude pour l'ANR.

# Chapitre 1

# Context and objectives of the study

This thesis has been developed thanks to the French agency *Agence Nationale de la Recherche* (ANR)[1], coordinated by the *Centre National de la Recherche Scientifique* (CNRS)[2], that founded the project ANR VolHand, *VOLant pour personne âgée et/ou HANDicapée : Direction Assistée Electrique Personnalisé adaptée au conducteur à mobilité réduite*[3].

This thesis was developed within the Control System Department of the Gipsa-lab, that is a multidisciplinary research lab created as a group between the CNRS, the *Institut Polytechnique de Grenoble* (INP)[4], the Joseph Fourier University and the Stendhal University. It also collaborates with the *Institut National de Recherche en Informatique et en Automatique* (INRIA)[5], the Grenoble Observatory and Pierre Mendès University. Gipsa-lab developments are focused especially on the automatic control, signal and images processing, voice and cognition fields.

## 1.1 Context of the study

People with reduced mobility face to some difficulty to turn the steering wheel when they drive their vehicle. In some cases, this difficulty may bring to the total loss of autonomy of the person, with consequences on the mood of the disabled person, on his family and, indirectly, on the society.

Existing adaptation systems are essentially mechanical (balls, forks, double steering

1. French National Research Agency
2. French National Center of Scientific Research
3. Steering wheel for elderly and/or disabled people : Personalized Electric Power Steering adapted for driver with reduced mobility
4. Grenoble Polytechnic Institute
5. National Institute for Research in Computer Science and Control

wheel..). They are imposed by the *Préfecture*[6] and they are installed in specialized centres with extra costs for patients. These systems are very simple and are widely diffused among drivers with reduced mobility with good results to improve the driving among these people. Besides, these equipments are standard : it is not possible to modify them according to the evolution of the disease, to the driver's effort or to his pain. We note also that there are no studies about the way to provide the correct steering assistance for drivers with reduced mobility.

The VolHand project was proposed to bring a solution to this problem. It is an industrial research project with the goal to develop an EPAS system for people with reduced mobility.

### 1.1.1 Context and impact on the economy and the society

Causes at the origin of the loss of autonomy can be multiples. Among others, a brutal accident that brings to the handicap of the driver or the passengers, a progressive neuromuscular disease that may affect the person or the physiological ageing of muscles and tissues.

Nowadays, the loss of autonomy may reveal dramatic among people with reduced mobility, because of recent changes of the society. For example, let us consider the case of aged people. In late 1950's, society based on family nucleus, where aged and young people lived together and they took care each-other. Nowadays, aged people do not live any-more with their sons, but they prefer living alone. Since 1960, the number of aged people (over 60 year old) living alone passed from 6% to 14%, with a majority among women (16%) w.r.t. men (12%), as it is explained in [84] and shown in Fig. 1.1.

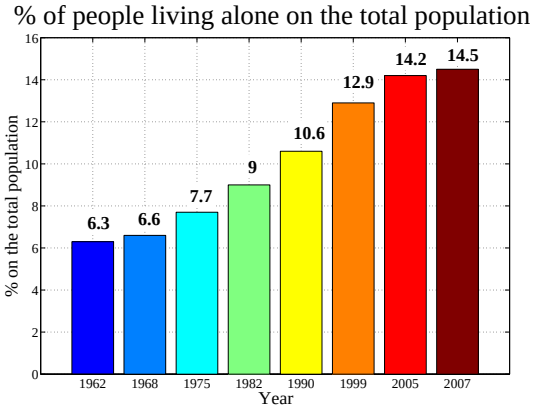


**Figure 1.1** – Graphs reporting the percentage of the people living alone on the total population (Source Insee [84])

6. French legislative institution, that represents the State at local level and has, among others, the duty to release the driving license.

For this part of the population, the experience of loss of autonomy is always painful. It translates into a loss of mental and physical capacity to do some tasks of daily life, but also into a loss of the freedom in accomplishing these tasks without the assistance of an external person. Fighting against isolation and depression, together with the possibility to go everywhere are among the main requests of the people with reduced mobility.

Since its introduction, the car is a vehicle of emancipation and the ability to drive the own vehicle is a symbol of autonomy, freedom and pleasure. Moreover, the car plays a fundamental role in daily life : it allows to move everywhere at every-time, with the only constraints in terms of traffic and driving ability. This last element may be affected from the visual-cognitive and musculoskeletal diseases. The force and the suppleness of muscles diminish, coordination is less efficient, rigours of the journey appear more quickly. Moreover, the risk of chronic and disabling diseases may bring people to abandon the driving of the vehicle, and, consequently, to lose their autonomy.

The task to turn the steering wheel is a critical point, because it requires a large amplitude of the movement, a minimum effort and a precise control. People with reduced mobility are faced to the difficulties to turn the steering wheel, because they are limited into their joint flexibility and into their capacity to produce a muscular force.
More generally, this problem concerns aged, disabled and handicapped people.
TNS Sofres [4] survey findings indicate that the 73% of French people older than 65 years have a vehicle and that the 30% of drivers will be over 60 in 2040.
There are not many informations concerning the driving among disabled people, but a study [87] estimates that 36.2% of the active population suffers of diseases to the upper limb and that these diseases are one of main causes that brings to interrupt the work. Finally, 3% of the driving licenses released in France concern people with handicaps to the musculoskeletal system. From an economic point of view, the *Caisse Nationale de Solidarité pour l'Autonomie* (CNSA) [5] reveals that the welfare due to the compensation of the loss of autonomy among aged and handicapped people augmented from 47.000.000.000 € in 2007 to 52.400.000.000 € in 2011. 36% of these resources was devoted to aged people, while 64% was for handicapped people.

Face to the suffering, the isolation and the social costs, all the technological innovations that may help to extend the driving ability for these people are welcome.

### 1.1.2 Current systems for the help to the driving

Let us consider the case of people with reduced mobility, because of a neuromuscular disease. Current systems to help the driving in these cases are imposed from the *Préfecture*, when it releases the driving license to the patient, according to the European directive

4. French leader into studies of marketing and opinion
5. National fund for the solidarity and the autonomy

2007/46/CE. This institution rules what is the adaptation mechanism to apply on the vehicle according to the specific disease of the patient. Then, a specialized manufacturer mounts the proposed system on the vehicle. It is possible to divide adaptation systems in two main categories, that identify the entity of the disease : unilateral disabilities, if the disease causes the partial or complete invalidity to one upper limb, and bilateral disabilities, if the disease affects both the upper limbs.

#### 1.1.2.1 Unilateral disabilities

This class includes patients who can drive with only one upper limb. For these people, three systems of adaptation, shown in Fig. 1.2, are proposed : the removable ball, the fork and the tripod. The ball on the steering wheel is used in case of total or partial invalidity

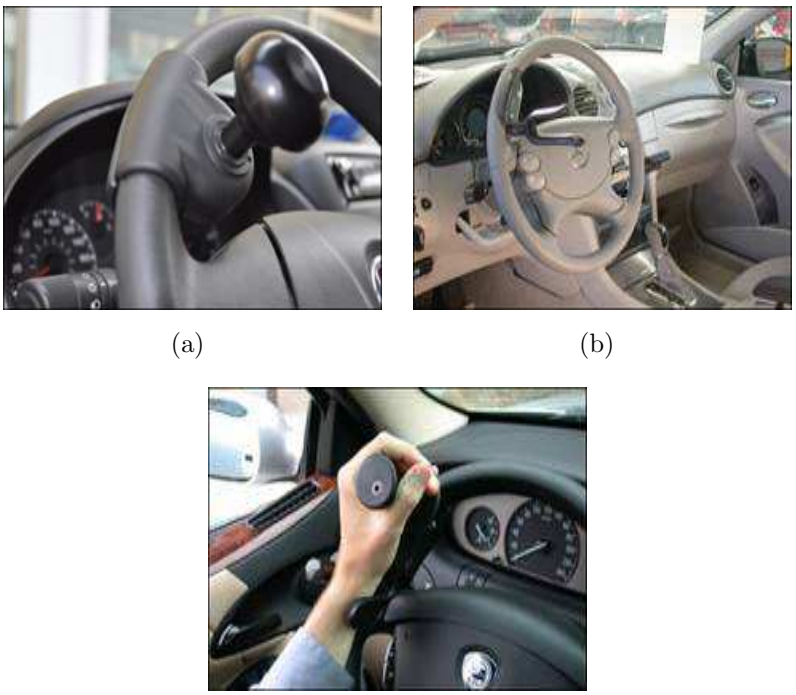

(a) (b)

(c)

**Figure 1.2** – Examples of ball (a), fork (b) and tripod (c), provided from the manufacturer Handi-Mobil. These adaptation mechanisms are employed in case of unilateral disabilities.

to one of the two arms. The fork on the steering wheel is used in case of patients with a good mobility of the wrist, but bad mobility of the fingers. Finally, the tripod is mounted in case of partial or complete invalidity of the wrist and the fingers.

There is no clear policy about the position of these systems on the steering wheel, because some manufacturers (such as Hand-drive) mount the ball at the top/center of the steering wheel, while some others (such as Hand-mobile or Ceremh) mount the ball on the side of

the healthy arm, with a position described in clock-code as 2 o'clock for the right hand and 10 o'clock for the left hand.

A radio command can be mounted close to the adaptation mechanism to allow the driver to activate the headlights or the flashes and to show the position. In some cases, a lever is mounted on the opposite side to brake or to accelerate the vehicle, in case of patients without problems of prehension (gripping ability) or quadriplegic. This lever is directly linked to the pedals of brake and acceleration.

#### 1.1.2.2 Bilateral disabilities

This class includes patients who can drive with both upper limbs, but with some difficulties due a certain pathology. For these patients, many mechanisms to unload the steering wheel are proposed. Among them, it is possible to find a steering wheel with a bigger inclination over the horizontal plane. This solution is adopted when the driver has a difficulty to exert the force at the level of the shoulder. This system is limited from the presence of the steering column and cannot be really used on cars. However, it is a solution that is widely used to improve the comfort of healthy drivers on trucks.

The steering wheel with a reduced radius can be installed at the place of the original steering wheel. This system requires a smaller amplitude of the arms, but its cost is quite high (about 10,000 €). Moreover, it requires a bigger force to steer it, because of its reduced radius.
It is also possible to substitute the steering wheel with a joystick, but this solution is also very expensive (about 30,000 €). The steering wheel with reduced radius and the joystick cannot be employed in case of a serious neurological pathology, because they both require a training phase and patients have to pass a specific exam to obtain the driving license. Examples of these adaptation systems are shown in Fig. 1.3. In every case, the

(a) (b)

**Figure 1.3** – Examples of mini steering wheel (a) and joystick (b), provided by the Handi-Mobil manufacturer. These adaptation mechanisms are used in case of bilateral disabilities.

adaptation requires the approval of the *Préfecture*, the installation in a specialized center

and significant extra costs. Moreover, the device is standard and cannot be modulated in function of the evolution of the disease.

As a concluding remark, nowadays, there is no a simple device that can be adapted to the muscular ability of the patient or that can diminish the strain of the driver.

## 1.2 Historical facts and state-of-art about EPAS systems

### 1.2.1 Introduction of EPAS systems on commercial vehicles

Power steering systems are basically a power-assisted standard steering system. Steering assistance is mandatory to reduce driver's steering effort and to improve steering feel in multiple situations. Steering feel is effectively defined by the steering wheel torque the driver senses during steering manoeuvres and by the vehicle response to steering inputs [92]. At stand-still or at low speeds of the vehicle, tire-road friction torque is the main responsible of the steering feel. Nevertheless, the low pressure of the tires, the radial tire, the tendency to front wheel drive and the consequent greater concentration of weight on the front part of the vehicle increase the static steering torque, with a bigger demand in terms of driver's exerted torque. The increased steering torque implies that the driver has more difficulties to move the steering wheel in all these situations. Therefore, power steering has to be employed to reduce the steering torque exerted by the driver through the assist torque provided by the external power unit. However, the assist torque cannot compensate the entire feedback torque to the driver, otherwise the driver would lose the driving sensation and, consequently, the control of the vehicle. One of the main challenge into the design of power steering systems consists into finding a good compromise between a good steering feel and the correct reduction of the driver's steering effort.

Hydraulic Power Assisted Steering (HPAS) direction was the first system of assisted direction for commercial vehicles, introduced in 1950's by Chrysler Corporation and General Motors. Hydraulic pressure typically comes from a rotary vane pump driven by the engine of the vehicle. A double-acting hydraulic cylinder applies a force to the steering gear, that in turn steers road wheels. The steering wheel operates on a valve to control the flow to the cylinder. The more torque the driver applies to the steering wheel and column, the more fluid the valves allow through to the cylinder, and so the more force is applied to steer the wheels. A torque sensor, that is made up of a torsion bar at the lower end of the steering column, measures the torque applied to the steering wheel. As the steering wheel rotates, so does the steering column, as well as the upper end of the torsion bar. Since the torsion bar is relatively thin and flexible and the bottom end usually resists being rotated, the bar will twist by an amount proportional to the applied

torque. The difference in position between opposite ends of the torsion bar controls the valve of the hydraulic pump. The valve allows the fluid to flow to the cylinder, that provides the steering assistance. The working liquid, also called "hydraulic fluid" or "oil", is the medium by which pressure is transmitted. Common working liquids are based on mineral oil.

The great space occupied from the hydraulic pomp inside the vehicle pushed Suzuki to introduce the first EPAS system in last 1980's. This system employs an electric motor, fixed on the transmission system, to produce the assistance torque, without the hydraulic contribution. Sensors detect the position and the torque of the steering column and a computer unit applies the assistance torque through the motor. This allows varying amounts of assistance to be applied depending on driving conditions. It is possible to tailor the steering-gear response to variable-rate and variable-damping suspension systems, optimizing ride, handling, and steering for each vehicle. EPAS systems have also the advantage in terms of fuel efficiency, because there is no belt-driven hydraulic pump constantly running, whether assistance is required or not.
Another advantage is the elimination of a belt-driven engine accessory and several high-pressure hydraulic hoses between the hydraulic pump, mounted on the engine, and the steering gear, mounted on the chassis. This greatly simplifies manufacturing and maintenance. By incorporating electronic stability control, EPAS systems can instantly vary torque assist levels to aid the driver in corrective manoeuvres.

In 1990's, many manufacturers developed the Electro-Hydraulic Power Steering (EHPS) systems, called "hybrid" systems. They use the same hydraulic assist technology as standard systems, but the hydraulic pressure comes from a pump driven by an electric motor instead of a drive belt at the engine. Evolution of this technology has seen the introduction of different electric motors (in continuous current or brush-less). Since 1999, Fiat introduced a "city" button on its vehicles that allows to activate only the electronic power assistance at low speeds. This button is automatically disabled when the cruise speed exceeds the 50 $\mathrm{km\,h^{-1}}$ to avoid loss of control of the vehicle. Recent researches [49] and [50] employ non-linear controllers to enhance the overall energetic efficiency of the steering system and the possibility of a variable steering assistance, while keeping the good steering feel of traditional hydraulic steering systems.

Last power steering technology is known as steer-by-wire or decoupled direction. Transmission tree between the steering wheel and the wheels is eliminated, but an electric motor drives the direction of the vehicle. Main difficulties of the steer-by-wire systems are the meager capacity to reproduce driver's feel and to guarantee its safety, as shown in ([1],[52],[78]).

Nowadays, HPAS systems are widely diffused on the market of the city vehicles, while EPAS systems still allow to the market of brand products. However, research focuses on EPAS systems for their advantages in terms of fuel consumption, road feel feedback

to the driver and return-to-center performance of the steering wheel. Moreover, EPAS systems and many researches about them base on the assumption to consider a general driver's profile. They are not conceived keeping into account symptoms due to a specific pathology, that may affect drivers with reduced mobility. This thesis deals with the problem to design EPAS systems, which are adapted to exigences of this class of drivers.

### 1.2.2 Control frameworks of EPAS systems

In literature, several research have been trained about EPAS systems, but they focus more on the control of the EPAS system than on the design of the assistance curves, used to allow the electronic motor to provide the assistance.

#### 1.2.2.1 Control framework with static booster curves

A typical control framework can be found in [42], where authors employ static maps to produce a reference steering torque $\tau_{ref}$, that is determined by a torque map and depends from driving conditions (i.e. driver's exerted torque $\tau_v$ and cruise speed of the vehicle $v$). This reference torque is used to calculate the error with respect to the current torque $\tau_{ass}$ provided by the electric motor. This error given in input to a feedback controller, that allows to the electric motor to generate an appropriate assist torque $\tau_{ass}$, that approaches to the reference torque. The scheme of this control framework is shown in Fig. 1.4.

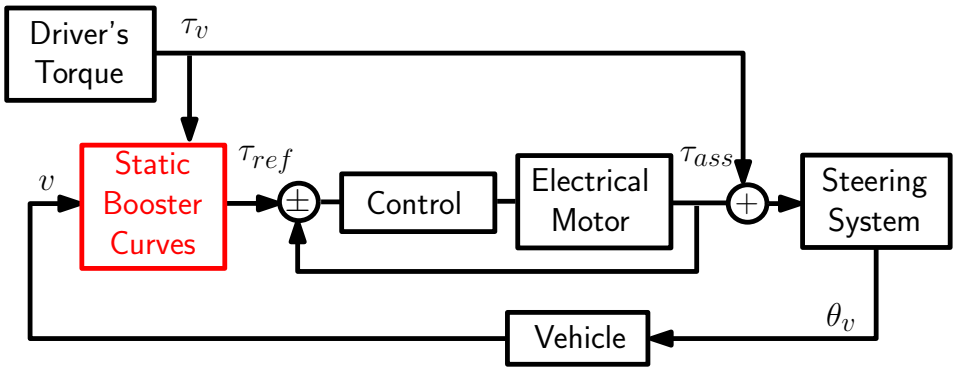


**Figure 1.4** – General control framework, where static maps are used as reference torque for the feedback control

In this thesis, an overview about most relevant research works using this control scheme is done. To this aim, let us consider the work in [92] where authors propose a procedure to design a fixed structure optimal controller to stabilize the system with high assist gain and to minimize the torque vibrations, that may affect driving feel and safety.

An optimal Linear Quadratic (LQ) controller for a dual pinion EPAS is proposed in [73] to ensure the stability and to reduce vibrations in response to the driver's torque.

To improve the steering feel, in [83] authors propose a method to transmit information of low frequency dynamics of the tire-road contact friction load. Feedback road information is regarded as a frequency band of tire and steering wheel transmission characteristics. In [83], a method of supplying road information to the driver using a robust controller is proposed. In addition, the suitability and effectiveness of this EPS control system in supplying road information, derived from a greater freedom in designing the steering characteristics, is experimentally proven.

To improve steering-wheel return-ability for EPS-equipped vehicles, in [55] authors developed a new control strategy based on the estimation of the alignment torque generated by tires and road surfaces. The steering feedback control gain is adjusted according to the estimated reaction torque.

To attenuate the road disturbance, authors in [25] propose a framework control structure with two cascade controllers. A H-infinity controller is used to address the driver's feeling and regulate the motion response, while a Proportional Integrative (PI) controller is used to produce the assist torque according to the command from the H-infinity controller.

A robust H-infinity controller is developed also in [24] to provide robust stability and to minimize effects of disturbances on the assist torque. A driver's torque estimator is introduced using the measurement of the pinion torque. This estimator uses improper transfer functions of the EPAS model, that are approximated as stable and proper transfer functions.

Recently, in ([61], [65]) authors applied a sliding control and a sliding observer to improve steering wheel return-ability and free control performance of the system.

All these publications employ linear static maps to generate the reference to control the electrical motor with various goals : ensuring stability of the system, improving steering feel or steering-wheel return-ability. These maps provide a simple linear relation between the assist torque $\tau_{ref}$ and the driver's torque $\tau_v$. This function varies according to the cruise speed of the vehicle $v$. A generic mathematical formulation that describes these reference maps is :

$$\tau_{ref} = \begin{cases} 0 & \text{if} \quad |\tau_v| \leq \tau_{v\,\min} \\ h(v) f(\tau_v - \tau_{v0\,\min}) & \text{if} \quad \tau_{v\,\min} \leq |\tau_v| \leq \tau_{v\,\max} \\ \tau_{ref\,\max} & \text{if} \quad |\tau_v| \geq \tau_{v\,\max} \end{cases} \tag{1.2.1}$$

where $\tau_{v\,\min}$ and $\tau_{v\,\max}$ are, respectively, lower and upper values of driver's torque, beyond which the steering assistance saturates. The saturation value of the electrical motor is given from $\tau_{ref\,\max}$.
Saturation of the steering assistance has been introduced to guarantee driver's safety, because a too high assistance torque may cause the control lost of the vehicle by the

driver. Moreover, a saturation is required also to prevent motor crash face to too high control inputs.

The function $h(v)f(\tau_v - \tau_{v0\,\min})$ describe the growth of the assistance $\tau_{ass}$ w.r.t. the sensed driver's torque $\tau_v$. Value of $\tau_{v0\,\min}$ corresponds to the lower limit for the driver's torque, beyond which the assistance starts to act.
In many cases that can be found in literature (i.e. [94], [42], [88], [73], [55], [26], [62], [64]), function $h(v)$ is a simple linear function, that changes according to the speed of the vehicle $v$, as it is shown in Fig 1.5. It is noted that the speed of the vehicle plays an important role, because the assistance steering torque required by the driver varies with respect to it. At low speeds (e.g. during parking manoeuvres), it is advisable to provide a great amount of assistance torque. At high speeds driving, more solid (and heavier) steering feel should be created for safe driving. One benefit of using a linear torque map is that it can be easily altered according to driving situations or the driver's requests. However, a linear map does not improve steering stiffness, i.e. the steering perception linked to the applied force and to the resulting movement of the steering wheel. Drivers occasionally perceive as unpleasant these phenomenon.

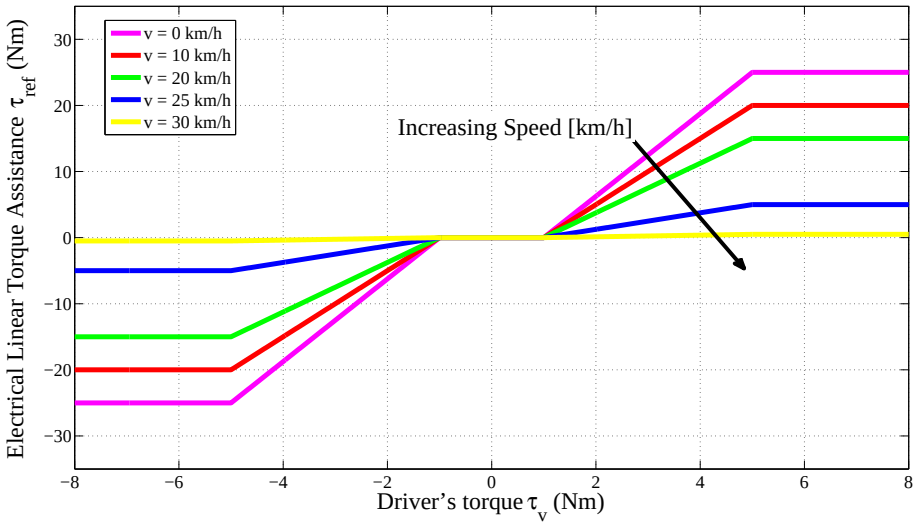


**Figure 1.5** – Example of the linear static booster curve, as used in ([94], [42], [88], [73], [55], [26], [62], [64]).

To improve steering stiffness, one solution consists into producing the reference assistance torque from a higher order polynomial. Torque assistance grows in a cubic or exponential way w.r.t. the driver's exerted torque or the steering wheel angle. This approach is introduced to imitate the opening curve of the hydraulic valve in HPAS systems with respect to the measured driver's torque. This approach is widely employed in ([66], [59], [24],[43], [85], [15]). Resulting booster curve is shown in Fig. 1.6. However, even through the use of very sophisticated control algorithms, the steering feel produced by these

curves is very different to that one provided by the hydraulic assistance. For this reason, a dynamic model for these booster curves is proposed, in order to mimic the complete assistance provided by HPAS systems.

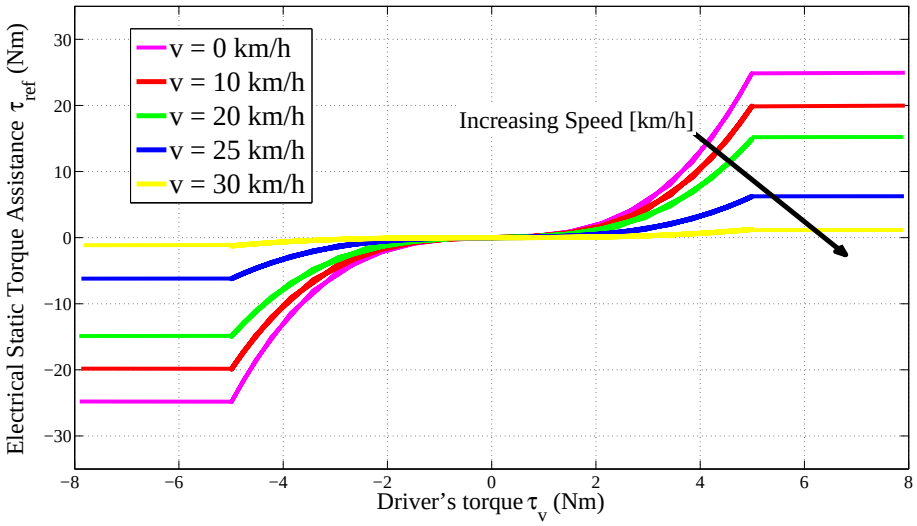


**Figure 1.6** – Example of the static booster curve, as used in ([66], [59], [24],[43], [85], [15]).

### 1.2.2.2 Control framework with hydraulic-mimic booster curves

The ultimate solution to improve steering stiffness and feedback consists into adopting a dynamic booster stage, that mimic the behaviour of the hydraulic valve, by reproducing the complete hysteresis cycle of the HPAS system.
Assistance coming from the booster stage is directly added in feed-forward to the exerted driver's torque, as it is shown in Fig. 1.7.

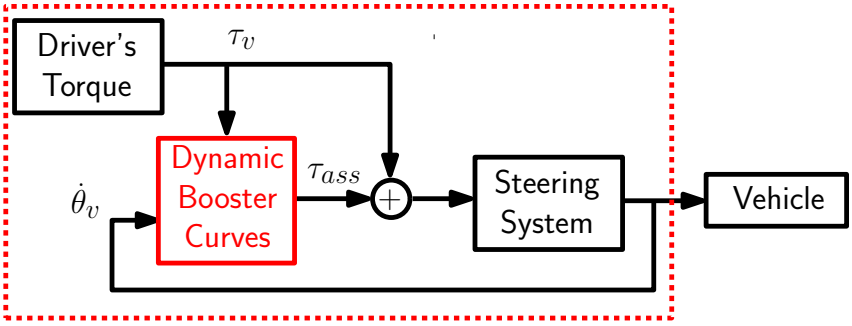


**Figure 1.7** – General control framework, that uses a dynamic booster stage to provide the steering assistance

To reproduce the hysteresis cycle of the hydraulic valve, the amplification torque $\tau_{ass}$ grows, according to the value of the driver's torque $\tau_v$ for different cruise speeds of the

vehicle $v$. If the driver's torque changes in direction, the downhill phase of the amplification torque is crossed. During this phase, the amplification torque decreases, until reaching the lower saturation value. An example of this hysteresis cycle is shown in Fig. 1.8.

The mathematical model used to obtain these amplification curves, shown in Fig. 1.8, was developed and tested experimentally in ([18], [19], [20], [21], [27]) and can be described with the following non-linear differential equation

$$\dot{\xi} = \begin{cases} \tau_{ass}(\xi) & \text{if} \quad |\xi| \leq \xi_{\max} \\ 0 & \text{else} \end{cases} \tag{1.2.2}$$

where

$$\tau_{ass}(\xi) = -a\xi - b\sqrt{|\xi|}\dot{\theta}_v + c\left(\sqrt{|\xi| + \epsilon}\right)\tau_v \tag{1.2.3}$$

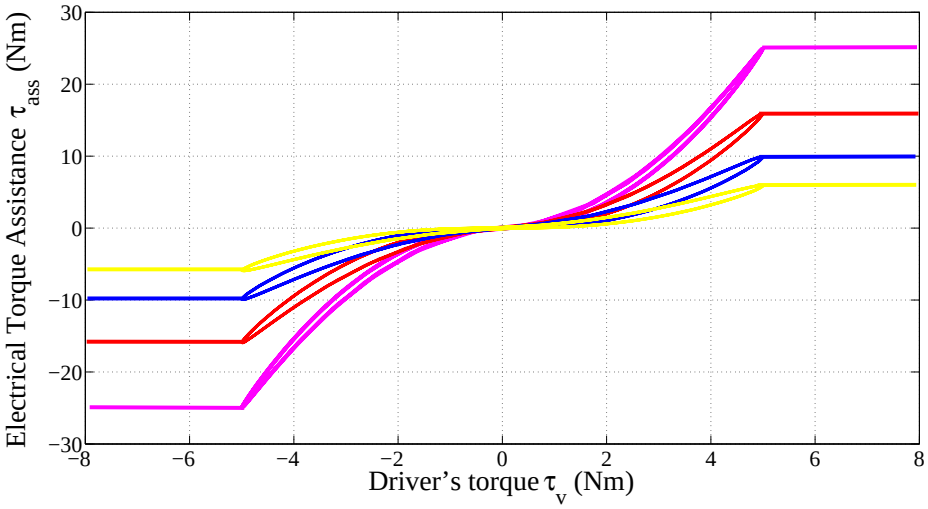


**Figure 1.8** – Dynamic booster curves, provided by the EPAS system, reported in ([18], [19], [20], [21], [27]).

The constant $a$ and the term $b\sqrt{|\xi|}\dot{\theta}_v$ represent the leakage flow. Both define the enclosed area of the hysteresis cycle. More in detail, $a$ defines the speed of reactivity of the booster stage, subjects to changes in driver's torque. High values of $a$ causes a fast response of the system. The sensation for the driver is a fast response of the steering system to his commands.
The value of $b$ influences the width of the hysteresis area. Low values of $b$ bring the system to behave as a static booster curve, with quadratic characteristic. High values of $b$ produce significant hysteresis effect, increasing the sensation of steering stiffness, felt

by the driver.
Constant $c$ can be obtained by imposing steady-state conditions on Eq. (1.2.3) (i.e. $\dot{\xi} = \tau_{ass}(\xi) = 0$ and $\dot{\theta}_v = 0$) for $\epsilon << |\xi|$ , a maximum value of amplification $\xi = \xi_{\max}$ and a constant value of driver's torque $\tau_v = \tau_{v0\,\max}$.
Under these hypothesis, it is possible to obtain

$$- a\xi_{\max} + c\left(\sqrt{|\xi_{\max}| + \epsilon}\right)\tau_{v0\,\max} = 0 \tag{1.2.4}$$

then, solving for $c$

$$c = \frac{a\sqrt{\xi_{\max}}}{\tau_{v0\,\max}} \tag{1.2.5}$$

This parameter changes the amplification factor and with $\xi_{\max}$ fixes the maximum amplification torque resulting from the booster stage. The constant values $\tau_{v0\,\max}$ corresponds to a constant value of driver's torque. For values of driver's torque $|\tau_v| \geq \tau_{v0\,\max}$, the output of the booster stage is saturate to the maximum value $\xi_{\max}$.
Coupling with the steering column is done through the measure of $\dot{\theta}_v$.

As concluding remark, it is possible to infer that among many possible specifications, an EPAS system is aimed at ensuring stability of the system, improving steering-wheel return-ability and attenuate the road disturbance. Moreover, it has to reduce driver's effort and to guarantee a good steering feel. These elements are valid for healthy and drivers with reduced mobility. In this last case, it seems appropriate to consider also limitations due to the disease and to modify standard steering assistance to alleviate these effects on the driving.

## 1.3 General control architecture & Road map of the thesis

The main contribution of this thesis is the proposition of a general methodology to adapt the standard EPAS systems designed for healthy drivers to drivers with reduced mobility. The proposed methodology has the advantage to overcome the extra costs due to the installation of dedicated devices and it is sufficiently generic to cover a large segment of patients.

A first important step towards the goal of this thesis consists in setting a control framework for the study of EPAS systems. This control framework is designed to be used for standard drivers and for drivers with reduced mobility. It includes models of the vehicle dynamics and of the steering column, with torques involved in a real driving situation (torsion due to flexibility of the force sensor, applied driver's forces and tire-road contact friction forces).
The control framework should also comprehend an observer to recover signals, that are

not sensed, and a control law that compensates the column flexibility. This is completed with a booster stage (power steering torque) specific to the driver's profile.

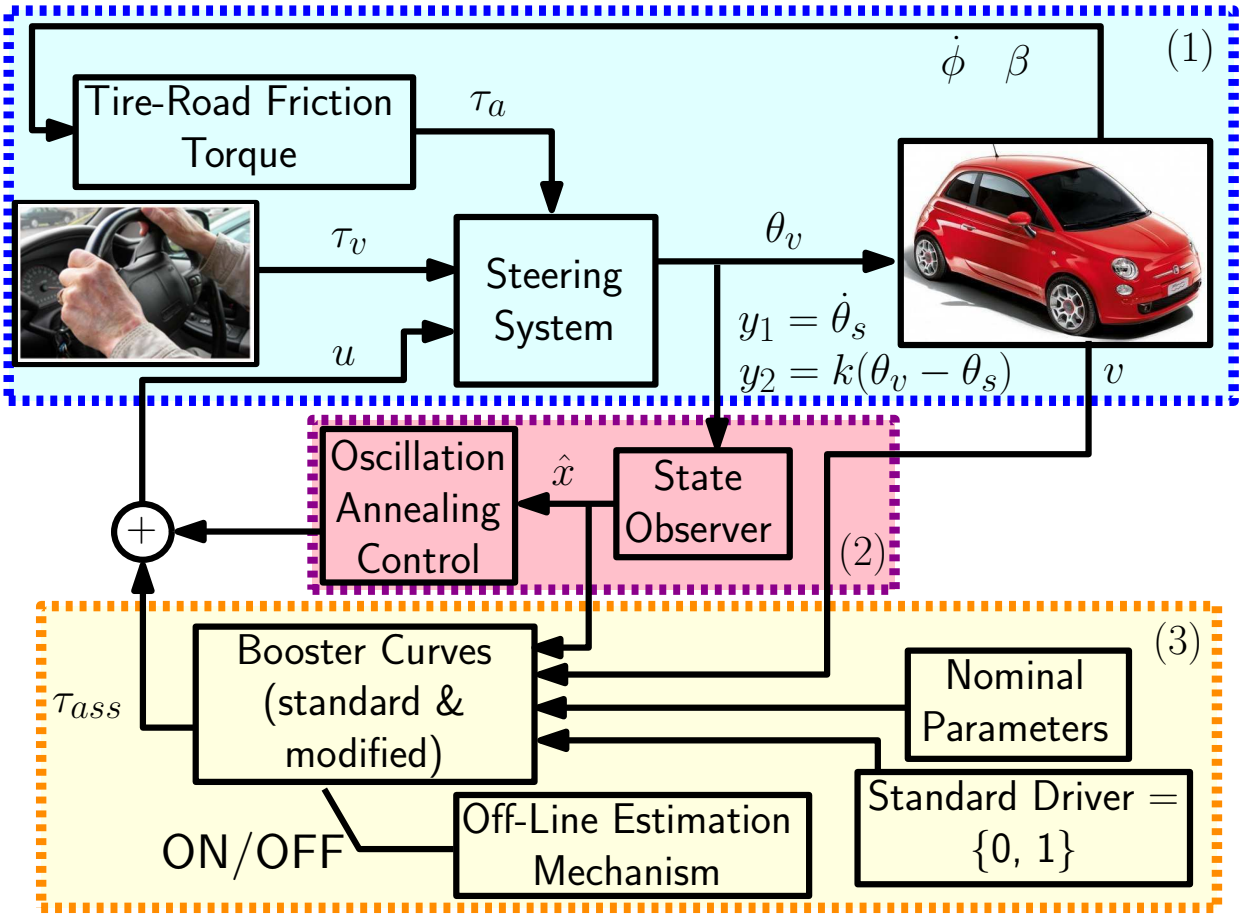


**Figure 1.9** – Model of the general architecture of the EPAS system. Variables : driver's exerted torque $\tau_v$, tire-road friction torque $\tau_a$, control input $u$, position of the steering wheel $\theta_v$, slip angle $\beta$, angular velocity of the wheel-rim $\dot{\phi}$, angular velocity of the column-shaft $y_1 = \dot{\theta}_s$, torsion of the steering column $y_2 = k(\theta_v - \theta_s)$, estimated state-space vector $\hat{x}$, assistance torque $\tau_{ass}$, cruise-speed of the vehicle $v$.

The proposed general architecture is shown in Fig. 1.9 and constitutes the road map for the following of this thesis. It is possible to identify 3 blocks :

– Block (1) concerns the study of the physical models of system, mainly, the dynamics of the steering column are considered. The steering column takes in input two exogenous inputs (the driver's exerted torque $\tau_v$ and the tire-road friction torque $\tau_a$) and a control input $u$ acting on the electrical motor. It drives the vehicle through the angular position of the steering wheel $\theta_v$.
  The influence of the tire-road friction torque is described through the use of dynamical models, that capture the phenomena of the self-alignment and of the sticking torques. These models require in input measures of the slip angle $\beta$ and the angular velocity of the wheel-rim $\dot{\phi}$. Note that to have a realistic tire-friction model, it is mandatory to test the power steering system. Main elements of this block are described in **Chapter** 2

– **Models and control strategies**.

– Based on the steering column model proposed in the Chapter 2, a linear optimal control that seeks to cancel the oscillations due to the torsion of the column is designed. This results in an output optimal feedback with an observer included, shown in the Block (2) in Fig. 1.9. In addition to cancel the oscillations, the control design seeks to preserve the impedance between the driver's exerted torque and the tire-road friction torque. In that way, the low frequency feelings of the driver will not be affected. In addition, the proposed state-observer estimates the state-variables of the system and the exogenous inputs $\hat{x}$, taking in input the measures of the angular velocity of the column-shaft $y_1 = \dot{\theta}_s$ and of the torsion of the steering column $y_2 = k(\theta_v - \theta_s)$. More details about this part are shown in **Chapter** 3 – **Oscillation annealing and torque observer design**.

– Block (3) concerns the steering assistance, provided by the standard booster curves, and all components that can be added to adapt standard booster curves for drivers with reduced mobility. To differentiate the assistance provided for a general driver's profile from that one used in case of driver with reduced mobility, a binary parameter is given in input to this block (standard driver = $\{0, 1\}$).

  If we consider a general driver's profile, the steering assistance is provided by dynamical booster curves.

  If we consider a driver with reduced mobility, the steering assistance is given from the modified booster curves that keep into account difficulties of the driver. An additional estimation block, that acts off-line with the vehicle at stand-still, is used in case of drivers with reduced mobility. At the end of this procedure, the estimated parameters are given in input to the booster curves.

  Both the steering assistances require as input the estimated driver's exerted torque $\hat{\tau}_v$ from the state observer, the cruise speed of the vehicle $v$ and the initial nominal parameters. The output of this stage is the assistance torque $\tau_{ass}$, that sums to the control input to delete oscillations of the steering column.

  Details about this block are developed in **Chapter** 4 – **Power steering booster stage**.

The general architecture is validated experimentally on a HIL setup and results of this validation are shown in **Chapter** 5 – **Experimental validation of the general methodology**.

## 1.4 Publications list

Main contributions of this thesis are the principal subject of the following publications :

### 1.4.1 International conference papers with proceedings

- Ciarla, V. ; Cahouet, V. ; Canudas de Wit, C. ; Quaine, F., "Genesis of booster curves in Electric Power Assistance Steering systems", 15th International IEEE Conference on Intelligent Transportation Systems (ITSC), pp.1345–1350, 16–19 Sept. 2012
- Illan, J.T. ; Ciarla, V. ; Canudas de Wit, C., "Oscillation annealing and driver/tire load torque estimation in Electric Power Steering systems", IEEE International Conference on Control Applications (CCA), pp.1100–1105, 28-30 Sept. 2011

### 1.4.2 ANR working reports

- Ciarla, V. ; Canudas de Wit, C. ; Dumon , J. ; Quaine, F. ; Cahouet, V., "Definition of a methodology to adapt a model of steering assistance and its experimental validation", http ://hal.archives-ouvertes.fr/hal-00797633
- Ciarla, V. ; Cahouet, V. ; Canudas de Wit, C. ; Quaine, F., "Notes on the analytic solution for the Dahl's friction model", http ://hal.archives-ouvertes.fr/hal-00744521
- Ciarla, V. ; Canudas de Wit, C. ; Quaine, F. ; Cahouet, V., "Preliminary study on Electronic Power Assistance Steering (EPAS) systems", http ://hal.archives-ouvertes.fr/hal-00757002
- Ciarla, V. ; Canudas de Wit, C. ; Quaine, F. ; Cahouet, V., "Exogenous input estimation in Electronic Power Steering (EPS) systems", http ://hal.archives-ouvertes.fr/hal-00757001
- Ciarla, V. ; Canudas de Wit, C. ; Quaine, F. ; Cahouet, V., "Oscillation annealing in Electronic Power Steering (EPS) systems", http ://hal.archives-ouvertes.fr/hal-00757000

# Chapitre 2

# Models for simulation

## 2.1 Introduction

To achieve to the main goal of this thesis, a general control architecture of the steering system is proposed. This chapter is devoted to the description of the dynamical systems that compose this architecture, mainly, the steering system and the dynamical model of the tire-road friction torque. The main use of proposed models is numerical simulation. For each system, a non-exhaustive overview of the corresponding state-of-art is done. Then, a mathematical description of each one is provided.

## 2.2 Preliminary background on the steering system

### 2.2.1 Steering layout

The steering wheel is positioned in front of the driver, who applies a torque to rotate it and to steer the wheels of the vehicle. The steering column converts the rotary motion of the steering wheel to the translational motion of the wheels of the vehicle. Classical steering layouts [67] are the front-wheel-drive layout, the rear-wheel-drive layout and the four-wheel-drive layout, as shown in Fig. 2.1.

Front-wheel-drive layout is typically employed on standard cars. Engine is located in front of the front axle and the motion on the steering system is also transferred to front wheels, as it is shown in Fig. 2.1(a). This layout is typically chosen for its compact packaging. Since engine and driven wheels are on the same side of the vehicle, it is not necessary to have a central tunnel through the passenger compartment to accommodate the propeller shaft to transmit the torque from the engine to the driven wheels.

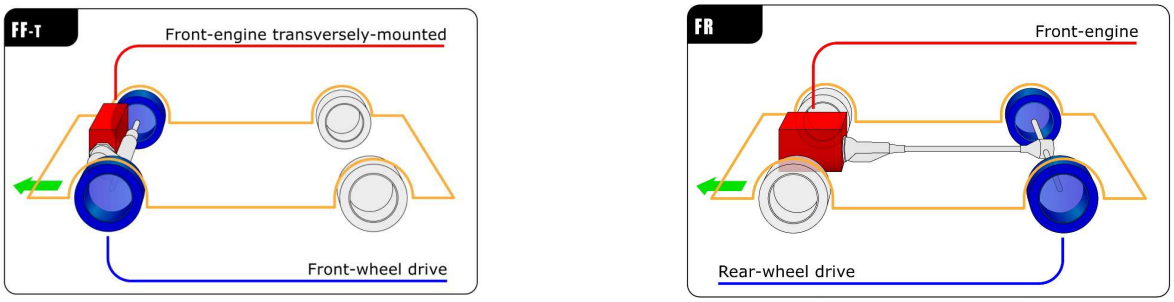


(a) Front-wheel-drive layout

(b) Rear-wheel-drive layout

**Figure 2.1** – Commonly used wheel-drive layouts, as shown in [67]

In rear-wheel-drive layout, the steering system drives front wheels and motion is transferred from the front engine to rear wheels, as it is shown in Fig. 2.1(b). It is commonly used on sport vehicles, for its simple design and good handling characteristics. During acceleration, weight is transferred to the rear part of the vehicle, increasing the load and the grip of rear wheels. As steered wheels are also the driven wheels, cars with front wheel drive layout are generally considered superior to vehicles with rear-wheel layout in conditions such as snow, mud or wet tarmac. Weight of the engine over the driven wheels also improves grip in such conditions. However, powerful cars rarely use front-wheel-drive layout, because weight transference under acceleration reduces weight on front wheels and their traction, putting a limit on the amount of torque that can be used. Electronic traction control can avoid wheel-spin, but reduces also the benefit of extra power (torque) of the motor.

Finally, four-wheel steering layout is used by some vehicles to improve steering response. It can increase stability of the vehicle at high speeds and decrease the turning radius at low speeds. This layout found its most widespread use on monster trucks, where manoeuvrability in small arenas is critical. It is also popular in large farm vehicles. Some modern European Intercity buses also use four-wheel steering to assist manoeuvrability in bus terminals and also to improve road stability.

### 2.2.2 Components of the steering system

Main components of the steering system are the steering column and the gear unit. Steering column is a shaft, that connects the steering wheel to the gear unit. On modern cars, steering column is designed to collapse, in order to protect the driver in case of collisions. Gear unit translates the rotational torque applied to the steering shaft to the left-to-right motion of the tie rod. As for the steering layout, it is possible to find different kinds of gear unit, as it is shown in Fig. 2.2.

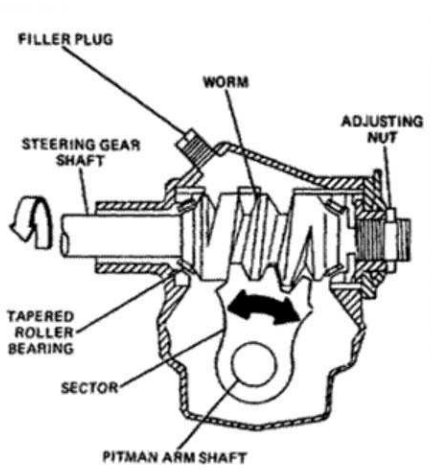


(a) Worm-sector gear unit

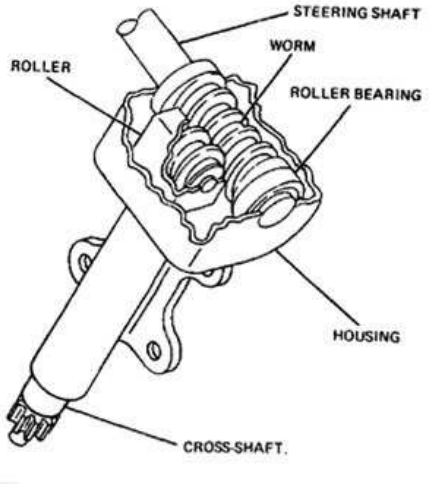


(b) Worm-roller gear unit

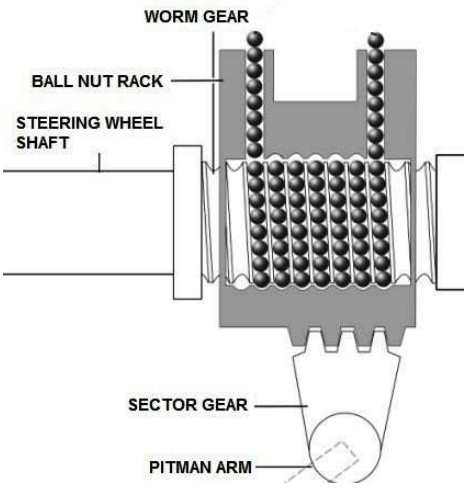


(c) Gear unit with recirculating ball nut

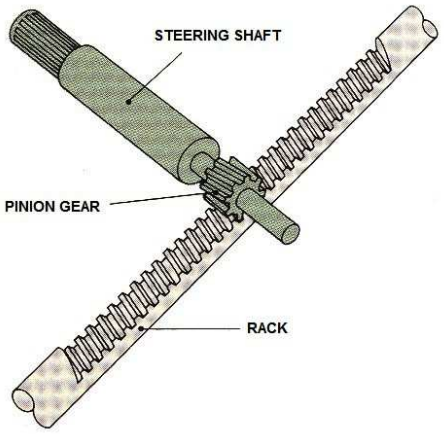


(d) Rack and pinion gear unit

**Figure 2.2** – Common examples of gear unit, as shown in [51]

They differentiate each other for the mechanics of the movement.

The classical gear unit is at worm-sector (see Fig. 2.2(a)), where the worm is connected to the steering shaft. When the steering shaft is rotated, it will turn the worm around its axis causing the sector to rotate. The pitman arm, which is attached to the sector and the steering linkage converts the angular motion of the sector shaft into the linear motion to steer the wheels.

Worm-roller gear unit is similar to the worm sector in the worm part, but it differentiates because the sector is replaced with a roller, as it is shown in Fig. 2.2(b). The worm rotates the roller, that displaces the steering linkage to drive the wheels in the necessary

direction.

In case of gear unit with recirculating ball nut (see Fig. 2.2(c)), the worm is rotated by the steering shaft. The block of the worm gear has a threaded hole and gear teeth cut into the outside of the block to move the sector. When the worm is rotated, instead of moving further into the block since the worm is fixed, it displaces the block. The displaced block turns the gear across the gear teeth. Finally, the sector moves the pitman arm and passes through the steering linkage. Threads are filled with ball bearing, that recirculate, when the block is moved.

Last kind of gear unit is known as rack and pinion and it is shown in Fig. 2.2(d) : the pinion, controlled by the steering wheel via the steering column, has teeth that engage with teeth of the rack. Helical teeth replaced the older perpendicular ones, since they reduce pressure on the tooth and give some irreversibly. Pinion is rotated by the steering shaft, that is controlled by the steering wheel. Lateral moment in the rack caused by teeth of the pinion produces the displacement of the tie rod, that is connected to wheels of the vehicle. In this way, displacement of the tie rod steers the vehicle wheels accordingly.

For purposes of this thesis, we focus on standard city vehicles. For these vehicles, the front-wheel-drive layout, shown in Fig. 2.1(a), is employed and the standard gear configuration is rack and pinion, shown in Fig. 2.2(d). For these reasons, these elements are assumed as reference in this manuscript.

## 2.3 Mathematical model for the steering system

The mathematical model of the steering system establishes the relation between driver, steering wheel/column, electrical motor and tire/road contact forces. A real steering system contains several non-linear components, such as friction forces in the column, the rack, the motor as well as sticking and backslash in the gearbox. However, it is possible to approximate these terms by linear ones and to treat the approximation errors as model uncertainties. Consequently, it is imperative that feedback controller that are designed on the basis of the reduced model must be robust enough, to provide stability and satisfactory performance also on the real system.

In literature ([63], [61], [65], [62], [64], [93], [24],[43], [85], [15], [42]), it is possible to find many mathematical models for the steering system. Most of them are obtained by applying Newton's second law and examining torques acting on the steering column and the pinion driven by the electric motor. With these models, authors often consider in detail forces acting on the rack and electrical equations of the motor. These forces can be approximated as an overall inertia acting on the system, simplifying the system, as in [19], [27] and [18].

The mathematical model of the steering column used in this thesis considers the model, treated in [19], [27] and [18]. This model is characterized by the presence of the torsion force of the steering column. This physical element is present on the real system, but it is often neglected. The adopted model is shown in Fig. 2.3 and can be described by the

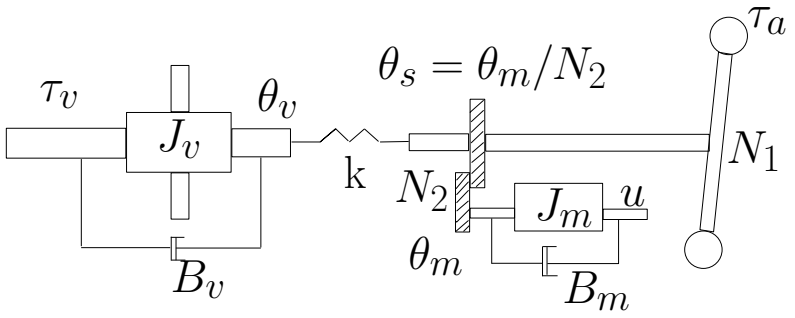


**Figure 2.3** – Mechanical model of the steering system.

following set of linear differential equations :

$$J_v\ddot{\theta}_v(t) = \tau_v - k(\theta_v(t) - \theta_s(t)) - B_v\dot{\theta}_v(t) \quad (2.3.1)$$

$$J_T\ddot{\theta}_s(t) = -k(\theta_s(t) - \theta_v(t)) - N_2^2 B_m\dot{\theta}_s(t) - \frac{\tau_a}{N_1} + N_2 u \quad (2.3.2)$$

with $J_T = \left(J_c + N_2^2 J_m + \frac{J_w}{N_1^2}\right)$ is the total inertia of the system. It is given from the sum of the inertia of the column $J_c$, of the motor $J_m$ and of the rack $J_w$. The electrical motor is connected to the steering column through the amplification gear ratio $N_2$, while the rack is connected through the reduction gear ratio $N_1$.

Variables $B_v$ and $B_m$ represent the viscosity of the steering wheel and of the electrical motor, respectively.

The torsion torque $F_t = k(\theta_v(t) - \theta_s(t))$ appears in opposite sign in the two equations and is at the main responsible of important oscillations of the steering column in open loop, as it will be shown in Chapter 3.

Angles $\theta_v(t)$, $\theta_s(t)$ and $\theta_m(t)$ correspond to the angular positions of the steering wheel, the steering column and the motor, respectively. The column-shaft angle can be obtained by dividing the motor angle $\theta_m(t)$ by the gear ratio $N_2$, as follows :

$$\theta_s(t) = \frac{\theta_m(t)}{N_2} \quad (2.3.3)$$

Exogenous inputs of the system are the driver's exerted torque $\tau_v$ and the tire-road friction torque $\tau_a$. Note that the friction torque is divided by the gear ratio $N_1$, that corresponds to the rotation of the steering wheel and the rotation of the wheels. This ratio depends from the vehicle : in motorcycles it is $N_1 = 1$, while in most passenger cars, the ratio is between 12 :1 and 20 :1. As an example, if a complete turn of the steering wheel (360 °) causes the wheels to turn 24 °, then the ratio is 15 :1.

The control input $u$ is actuated from the electrical motor, that improves also the driver's steering feel. Constants of the model are defined in Table A.1 in Appendix A. The state-space representation of this system and the analysis of its behaviour in open and closed loop is shown in Chapter 3.

## 2.4 Road friction phenomena

The operation of the steering system of a passenger car is characterized by frequent transitions from rest to turn. Steering velocity varies remarkably and includes the zero-speed condition. Therefore, friction of each component of the steering system often changes from a static to a dynamic condition.

Friction affects the sensitivity characteristics of a steering actuator, especially in conditions of relatively low input torque intended for small changes of the rack position. The friction reduction of mechanical components of the steering is one of the counter-measures for this problem. Active friction compensation offers another option because the assist motor can generate a cancelling torque.

Interesting surveys about friction models commonly employed in automotive can be found in [5] and [4]. In this thesis, an overview of the most relevant friction models is done. The final goal is indeed to have a turnkey model to describe the influence of this phenomenon on the steering system.

### 2.4.1 Introduction to models of friction

Most known class of models are the so-called "static" or "pseudo-static" models, that predict the friction force (magnitude and direction) as well as the aligning moment as a function of the slip for constant vehicle and tire angular velocity. The major representative of this class of models is known as "Pacejka's Magic Formula". This model is given from a formula with coefficients, that describe some of the typifying quantities of a tire, such as slip stiffness at zero slip and force and torque peak values. This formula is capable to describe the characteristics of side force, brake force and self-alignment torque with great accuracy ([6], [71], [72]).

Other steady-state models represent rather artificial curve-fitting procedures to experimental data and they do not interpret physics phenomena that give rise to the friction forces and moments. For a more in-depth discussion on the potential problems of the steady-state models see [23]. These models have disadvantages : they are limited to the steady-state conditions and suffer from singularities at low speeds. They also require the redefinition of the slip ratios, depending whether the motion mode is acceleration

or brake, and forward or backward. Velocity dependence is also added through specific methods. They are over-parametrized, difficult to calibrate and are not suitable for direct identification. In addition, static models are not linked to the physics of friction process. Their parameters lack any physical interpretation, making it difficult to integrate model dependencies on specific factors such as humidity of the road or tire-tread temperature. Also, these models need to be re-calibrated for different road and vehicle conditions, even if in [45] and [38] there are some identifiable approximations to the models, where the parameters can be estimated in real-time.

A different approach to describe the friction phenomenon is based on the assumption that this force is not static, but changes in time. To this aim, it should be described with differential equations and considered as a dynamical system. The so-called dynamic friction models use this approach ([30], [31], [32], [13], [14], [79], [22],[17]).

The pioneer of dynamic models was Dahl ([30], [31], [32]), who suggested a simple model for controlling systems with friction. He made some experiments on a ball bearing mechanism, that brought to conclusions that some microscopic irregularities located on the fractional surfaces contact area are the reason for the occurrence of dry friction (according to the classic solid mechanics). To represent this phenomenon, Dahl considered the curve representing the relation between the pressure force and the deformation, typical of solid mechanics, shown in Fig. 2.4.

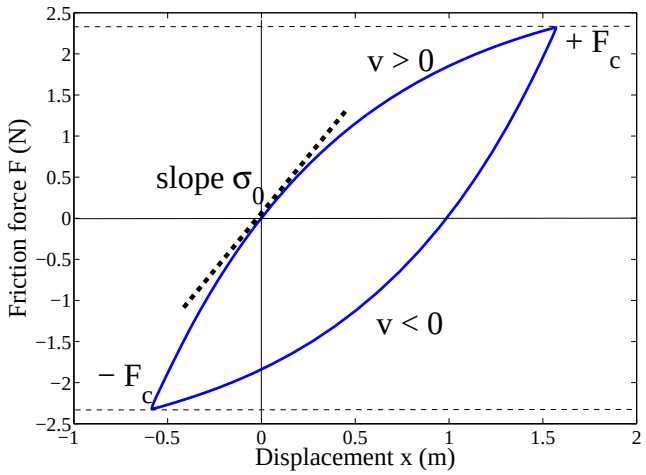


**Figure 2.4** – Pre-sliding displacement as described by Dahl's model. The simulation started with zero initial conditions.

Dahl's model does not neither include the static friction that needs to be overcome to enable relative motion of stationary objects in contact (stiction), nor a friction peak at a specific break-away distance. Nevertheless, this model is simple and it is easily possible to calculate the analytic solution of its differential equation (i.e. the evolution of the friction force w.r.t. the time). For this reason, it is preferred to more complicated models

for the optimization procedure, shown in Chapter 4.

To include stiction, Bliman and Sorine proposed a higher-order model in ([13], [14], [79], [37]), based on experiments run by Robinowicz [79]. In [13], dynamic models to handle the rate-independent hysteresis phenomena observed in practice were proposed. As an application to this work, a dynamic elastoplastic friction model was developed in [14]. This friction was then applied to the longitudinal motion of a tire in [12] and extended to the longitudinal and lateral motion in [82].
As it is shown in ([37], [5]), the Bliman-Sorine model can be problematic to use because of poor damping at zero crossing of the velocity. LuGre friction model is a valid alternative the Bliman-Sorine model, because it inherits the simplicity of the Dahl's model, but it exhibits a richer behaviour.

LuGre model is a dynamic friction model introduced in ([22], [17]). Friction is modelled as the average deflection force of some elastic springs. When a tangential force is applied to bristles, they deflect like springs. If the deflection is sufficiently large the bristles start to slip. The average bristle deflection for a steady-state motion is determined by the velocity. It is lower at low velocities, which implies that the steady-state deflection decreases with increasing velocity. This is useful to describe the phenomenon that surfaces are pushed apart by the lubricant and to model the Stribeck effect [1]. Moreover, the model includes rate-dependent friction phenomena such as varying break-away force and frictional lag. The LuGre model is described by following equations :

$$\frac{\mathrm{d}z}{\mathrm{d}t} = v_r - \sigma_0 \frac{|v_r|}{g(v_r)} z \tag{2.4.1}$$

$$F = \sigma_0 z + \sigma_1(v_r)\frac{\mathrm{d}z}{\mathrm{d}t} + \sigma_2 v_r \tag{2.4.2}$$

where $z$ is the average bristle deflection and $v_r$ is the relative velocity between the two surfaces. In Eq. (2.4.1), the first term gives a deflection that is proportional to the integral of the relative velocity, while the second term implies that the deflection $z$ approaches to the following steady-state value when $v_r$ is constant

$$z_{ss} = \frac{v_r}{|v_r|} g(v_r) = g(v_r)\mathrm{sign}(v_r) \quad . \tag{2.4.3}$$

The model behaves as a spring for small displacements. The function $g(v)$ is positive and gives a good approximation of the Stribeck effect. It can be expressed as

$$g(v) = \alpha_0 + \alpha_1 \exp^{-(v/v_0)^2} \quad . \tag{2.4.4}$$

1. The shear strength of a solid lubricant film at low velocities is generally higher than the shear forces of the corresponding fluid film built up at higher velocities. As a result, the friction coefficient in lubricated systems normally decreases when the velocity increases from zero. When the thickness of the film is large enough to completely separate the bodies in contact, the friction coefficient may increase with velocity as hydrodynamic effects becomes significant. The overall phenomenon is called the Stribeck effect [5].

It characterizes the steady-state of the model. The sum $\alpha_0+\alpha_1$ corresponds to the stiction force and $\alpha_0$ to the Coulomb friction force [5].
In Eq. (2.4.2), $F$ is the friction force, the parameter $\sigma_0$ is the stiffness of the bristles, while $\sigma_1$ is the damping and $\sigma_2$ is the viscous friction.

In [23], authors extend the LuGre model for the longitudinal road/tire interaction for wheeled ground vehicles. To this aim, authors assume that there is a contact patch between the tire and the ground and they develop a partial differential equation for the distribution of the friction force along the patch. The distributed model is very realistic, but it is not suitable for control purposes because it is necessary to choose a discrete number of states to describe dynamics of each tire. This has the disadvantage that a possibly large number of states is required to describe the friction generated at each tire. For this reason, the lumped model is derived to closely approximate the distributed model when it is used for control.

In [86], the longitudinal LuGre model is extended for longitudinal and lateral motion of the vehicle. Main friction phenomena described in [86] are the self-alignment torque and the sticking torque. Self-alignment torque appears when the speed of the vehicle grows up. It tends to rotate the wheels around their vertical axis and allows the wheels to return to the straight position. Sticking torque opposes to the movement of the tires, let them turning around the vertical axis. It is especially important at low speeds of the vehicle. Due the importance of these phenomena for the steering system, mathematical models used to describe them are discussed in detail in next paragraphs. Moreover, the original model of the sticking torque is improved to include the dependency from the speed of the vehicle and to obtain a more realistic behaviour.

### 2.4.2 Model for the self-alignment torque

Lumped LuGre friction model used in [86] to describe the Self-alignment torque derives from a distributed parameter model. The complete procedure to obtain the lumped model is described in ([23], [86]). In this thesis, only equations that are used for simulations are reported.

At this end, let define weighted mean internal friction states $\bar{z}_i(t)$ $(i = x, y)$ and $\hat{z}_y(t)$ for each tire and each direction of the movement and let write the corresponding differential equation for each state, as follows :

$$\dot{\bar{z}}_i(t) = v_{ri} - C_{0i}(v_r)\bar{z}_i(t) - \kappa_i^{ss}|\omega r|\bar{z}_i(t) \quad (i = x, y) \tag{2.4.5}$$

$$\dot{\hat{z}}_y(t) = \frac{G}{F_n L} v_{ry} - C_{0y}(v_r)\hat{z}_y(t) - \nu^{ss}|\omega r|\hat{z}_y(t) + \frac{|\omega r|}{L}\bar{z}_y(t) \tag{2.4.6}$$

They correspond to a physical deflection of the patch element along the $x$ and $y$ direction, respectively, located at the contact point $\zeta$ with respect to the patch frame at a given

time $t$.

In Eqs. (2.4.5) and (2.4.6), it is possible to recognize the rate-dependency of the aligning torque through the vector of the relative speeds $v_r = [\ v_{rx} \quad v_{ry}\ ]^T$. Each component of $v_r$ is defined as follows

$$v_{rx} = \omega r - v\cos(\beta) \tag{2.4.7}$$
$$v_{ry} = -v\sin(\beta) \tag{2.4.8}$$

with $\omega$ that corresponds to the angular velocity of the wheel of radius $r$, $v$ is the velocity of the vehicle and $\beta$ is the slip angle. Measure of the slip angle $\beta$ is easily obtained from the lateral bicycle model, shown in Appendix A.

Other common element to Eqs. (2.4.5) and (2.4.6) is the scalar function $C_{0i}(v_r)$ $(i = x, y)$, given by

$$C_{0i}(v_r) = \frac{\lambda(v_r)\sigma_{0i}}{\mu_{ki}^2} \quad (i = x, y) \quad , \tag{2.4.9}$$

In Eq. (2.4.9), $\sigma_{0i}$ is the normalized rubber stiffness and $\mu_{ki}$ is the kinetic friction coefficient through each direction $(i = x, y)$. The vector function $\lambda(v_r)$ is given from

$$\lambda(v_r) = \frac{||M_k^2 v_r||}{g(v_r)} \quad . \tag{2.4.10}$$

In Eq. (2.4.10), $\lambda(v_r)$ depends from the matrix $M_k$ of kinetic friction coefficients, where each parameter $\mu_{ki} > 0$ is an element on the main diagonal of matrix $M_k$.
Function $\lambda(v_r)$ depends also from function $g(v_r)$, that defines the steady-state behaviour of the model and the Stribeck effect. It is given by

$$g\left(v_r\right) = \frac{\|M_k^2 v_r\|}{\|M_k v_r\|} + \left(\frac{\|M_s^2 v_r\|}{\|M_s v_r\|} - \frac{\|M_k^2 v_r\|}{\|M_k v_r\|}\right) e^{-\left(\frac{\|v_r\|}{v_s}\right)^{\gamma}} \tag{2.4.11}$$

where $M_s$ is the matrix of static friction coefficients $\mu_{si} > 0$, $v_s$ is the Stribeck linear relative velocity, $\gamma$ is a steady-state constant, generally set to 1.

In Eqs. (2.4.5) and (2.4.6), it is possible to recognize steady-state constants $\kappa_i^{ss}$ with $(i = x, y)$ and $\nu^{ss}$. To obtain these values, authors in [86] make the assumption that the steady-state solution of the lumped model is the same as the steady-state solution of the distributed one. Details about the technique to obtain these values are shown in [86], [23] and [33]. We refer the reader to [86], [23] and [33] for all details of the derivation of such values, while we report here only the relevant final results.
First, let consider the constant $\kappa_i^{ss}$ with $(i = x, y)$ in Eq. (2.4.5). It is given from

$$\kappa_i^{ss} = \frac{1}{|\omega r|}\left(\frac{v_{ri}}{\bar{z}_i^{ss}} - C_{0i}(v_r)\right) \quad (i = x, y) \tag{2.4.12}$$

The only unknown element in Eq. (2.4.12) is $\bar{z}_i^{ss}$. It is obtained by integrating the corresponding value of steady-state $\bar{z}_i^{ss}$ of the distributed model along the patch length $L$

and under the hypothesis of a trapezoidal load distribution $f_n(\zeta)$ of the static friction force, shown in Fig. 2.5.

$$z_i^{ss}(\zeta) = C_{1i}\left(1 - \exp^{-\frac{\zeta}{C_{2i}}}\right) \quad (i = x, y) \tag{2.4.13}$$

where

$$C_{1i} = \frac{v_{ri}\mu_{ki}^2}{\lambda(v_r)\sigma_{0i}} \quad (i = x, y) \tag{2.4.14}$$

$$C_{2i} = \frac{|\omega r|}{C_{0i}(v_r)} \quad (i = x, y) \tag{2.4.15}$$

It is assumed that the friction torque develops along a trapezoidal load distribution $f_n(\zeta)$, because it satisfies the natural boundary conditions of zero normal load at the edges of the patch. It allows also to model the effect that the aligning torque changes in sign at higher lateral slip angles, as observed in practice. The load distribution $f_n$ is shown in Fig. 2.5 and is defined as follows

$$f_n(\zeta) = \begin{cases} \alpha_1\zeta, & \text{for } 0 \le \zeta \le \zeta_L \\ F_{max}, & \text{for } \zeta_L \le \zeta \le \zeta_R \\ \alpha_2\zeta + \beta_2, & \text{for } \zeta_R \le \zeta \le L \end{cases} \tag{2.4.16}$$

Values $\alpha_1$, $\alpha_2$ and $\beta_2$ define the geometrical shape of the load distribution. They correspond, respectively, to the initial and the final slope and the intercept. $F_{max}$ define the max value assumed by the normal distribution. The variable $\zeta$ define the position on the patch length $L$, while constants $\zeta_L$ and $\zeta_R$ define the left and the right limits of the distribution, as it is shown in Fig. 2.5.

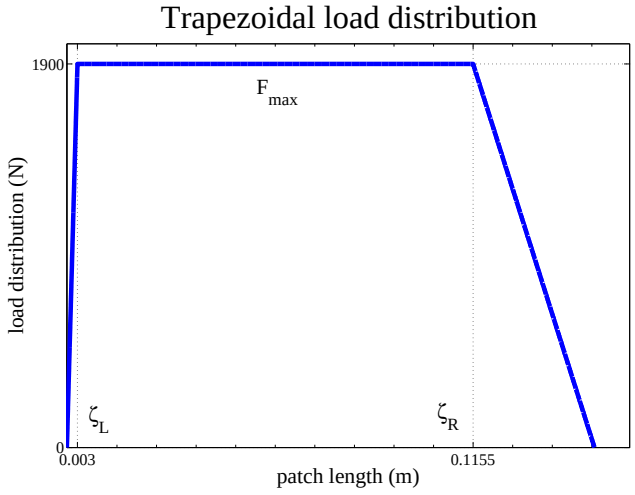


**Figure 2.5** – Profile of the trapezoidal load distribution of the friction force

Integrating Eqs. (2.4.13) with constants in Eqs. (2.4.14) and (2.4.15), under the hypothesis of the load distribution in Eq. (2.4.16), it is possible to obtain the complete expressions for $\bar{z}_i^{ss}$

$$\begin{aligned}
\bar{z}_i^{ss} &= \frac{1}{F_n}\int_0^L z_i^{ss}(\zeta) f_n(\zeta)\mathrm{d}\zeta \\
&= \frac{1}{F_n}\Big\{\frac{C_{1y}\,\alpha_1\,{\zeta_L}^2}{2} - C_{1y}\,\alpha_1\,\left[{C_{2y}}^2 - C_{2y}\,(C_{2y}+\zeta_L)\exp^{-\frac{\zeta_L}{C_{2y}}}\right] \\
&- C_{1y}\,f_{\max}\,\left[\zeta_L - \zeta_R + C_{2y}(\exp^{-\frac{\zeta_L}{C_{2y}}} - \exp^{-\frac{\zeta_R}{C_{2y}}})\right] \\
&+ C_{1y}\,\alpha_2\,\left[C_{2y}\,(C_{2y}+L)\exp^{-\frac{L}{C_{2y}}} - C_{2y}\,(C_{2y}+\zeta_R)\exp^{-\frac{\zeta_R}{C_{2y}}}\right] \\
&+ C_{1y}\,\beta_2\,(L-\zeta_R) + \frac{C_{1y}\,\alpha_2}{2}(L^2 - {\zeta_R}^2) + C_{1y}\,C_{2y}\,\beta_2\,\left[\exp^{-\frac{L}{C_{2y}}} - \exp^{-\frac{\zeta_R}{C_{2y}}}\right]\Big\}
\end{aligned}$$

Now, let consider the constant $\nu^{ss}$ in Eq. (2.4.6). Using the same methodology as for the constant $\kappa_i^{ss}$ with $(i = x, y)$, it is possible to obtain the following value

$$\nu^{ss} = \frac{1}{|\omega r|}\left[\frac{1}{\hat{z}_y^{ss}}\left(\frac{G v_{ry}}{F_n L} + \frac{|\omega r|\bar{z}_y^{ss}}{L}\right) - C_{0y}\right] \tag{2.4.17}$$

The steady-state value $\hat{z}_y^{ss}$ is given from

$$\hat{z}_y^{ss} = \frac{1}{2\sigma_{0y}}(\sigma_{0y}\bar{z}_y^{ss} + \sigma_{2y}v_{ry}) - \frac{M_z^{ss}}{F_n L\sigma_{0y}} - \frac{G\sigma_{2y}v_{ry}}{F_n L\sigma_{0y}} \tag{2.4.18}$$

where $\sigma_{0y}$ and $\sigma_{2y}$ are, respectively, the normalized rubber stiffness and the normalized viscous relative damping and the steady-state auto-aligning moment $M_z^{ss}$ of the distributed model. It is obtained by integration of steady-state friction force along the patch length $L$ and under the hypothesis of a trapezoidal distribution of Eq. (2.4.16). The

complete expression for $M_z^{ss}$ is given by

$$
\begin{aligned}
M_z^{ss} &= \int_0^L \left(\sigma_{0y} z_y^{ss}(\zeta) + \sigma_{2y} v_{ry}\right) f_n(\zeta) \left(\frac{L}{2} - \zeta\right) \mathrm{d}\zeta \\
&= C_{1y}\,\alpha_1\,\sigma_{0y} \left(2\,{C_{2y}}^3 - {C_{2y}}^3 \left(\frac{2\,\zeta_L}{C_{2y}} + \frac{{\zeta_L}^2}{{C_{2y}}^2} + 2\right)\exp^{-\frac{\zeta_L}{C_{2y}}}\right) - \frac{1}{3}\alpha_1 {\zeta_L}^3 (C_{1y}\sigma_{0y} + \sigma_{2y}\,v_{ry}) + \\
&- \frac{1}{2} C_{1y}\ C_{2y}, L\,\alpha_1\,\sigma_{0y} \left(C_{2y} - (C_{2y} + \zeta_L)\exp^{-\frac{\zeta_L}{C_{2y}}}\right) + \frac{L\,\alpha_1}{4}(C_{1y}\sigma_{0y}{\zeta_L}^2 + v_{ry}\sigma_{2y}{\zeta_L}^2) + \\
&+ C_{1y}\,f_{\max}\,\sigma_{0y} \left(C_{2y}\ (C_{2y} + \zeta_L)\exp^{-\frac{\zeta_L}{C_{2y}}} - C_{2y}\ (C_{2y} + \zeta_R)\exp^{-\frac{\zeta_R}{C_{2y}}}\right) + \\
&+ \frac{C_{1y}\,f_{\max}\,\sigma_{0y}}{2}({\zeta_L}^2 - {\zeta_R}^2) + \frac{f_{max}\,\sigma_{2y}\,v_{ry}}{2}({\zeta_L}^2 - {\zeta_R}^2) + \\
&- \frac{C_{1y}\,L\,f_{max}\,\sigma_{0y}}{2}(\zeta_L + \zeta_R) - \frac{L\,f_{\max}\,\sigma_{2y}\,v_{ry}}{2}(\zeta_L - \zeta_R) + \\
&- \frac{1}{2} C_{1y}\,C_{2y}\,L\,f_{\max}\,\sigma_{0y} \left(\exp^{-\frac{\zeta_L}{C_{2y}}} - \exp^{-\frac{\zeta_R}{C_{2y}}}\right) + \frac{C_{1y}\,\alpha_2\,\sigma_{0y}\,{\zeta_R}^3}{3} + \\
&- \frac{C_{1y}\,L^3\,\alpha_2\,\sigma_{0y}}{12} + \frac{C_{1y}\,\beta_2\,\sigma_{0y}\,{\zeta_R}^2}{2} - \frac{L^3\,\alpha_2\,\sigma_{2y}\,v_{ry}}{12} + \\
&- C_{1y}\,\alpha_2\,\sigma_{0y} \left({C_{2y}}^3 \left(\frac{2\,L}{C_{2y}} + \frac{L^2}{{C_{2y}}^2} + 2\right)\exp^{-\frac{L}{C_{2y}}} - {C_{2y}}^3 \left(\frac{2\,\zeta_R}{C_{2y}} + \frac{{\zeta_R}^2}{{C_{2y}}^2} + 2\right)\exp^{-\frac{\zeta_R}{C_{2y}}}\right) + \\
&+ \sigma_{2y} v_{ry} {\zeta_R}^2 \left(\frac{\alpha_2}{3}\zeta_R + \frac{\beta_2}{2}\right) - C_{1y}\,\beta_2\,\sigma_{0y} \left(C_{2y}\ (C_{2y} + L)\exp^{-\frac{L}{C_{2y}}} - C_{2y}\ (C_{2y} + \zeta_R)\exp^{-\frac{\zeta_R}{C_{2y}}}\right) + \\
&+ \frac{1}{2} C_{1y}\,L\,\alpha_2\,\sigma_{0y} \left(C_{2y}\ (C_{2y} + L)\exp^{-\frac{L}{C_{2y}}} - C_{2y}\ (C_{2y} + \zeta_R)\exp^{-\frac{\zeta_R}{C_{2y}}}\right) + \\
&- \frac{C_{1y}\,L\,\beta_2\,\sigma_{0y}\,\zeta_R}{2} - \frac{L\,\beta_2\,\sigma_{2y}\,v_{ry}\,\zeta_R}{2} - \frac{C_{1y}\,L\,\alpha_2\,\sigma_{0y}\,{\zeta_R}^2}{4} - \frac{L\,\alpha_2\,\sigma_{2y}\,v_{ry}\,{\zeta_R}^2}{4} + \\
&+ \frac{1}{2} C_{1y}\,C_{2y}\,L\,\beta_2\,\sigma_{0y} \left(\exp^{-\frac{L}{C_{2y}}} - \exp^{-\frac{\zeta_R}{C_{2y}}}\right)
\end{aligned}
$$

Finally, the value of $G$ in Eq. (2.4.18) is given by

$$
\begin{aligned}
G &= \int_0^L f_n(\zeta)\zeta \mathrm{d}\zeta \\
&= \frac{\alpha_1}{3}\zeta_L^3 + \frac{f_{max}}{2}\left(\zeta_R^3 - \zeta_L^3\right) + \frac{\alpha_2}{3}\left(L^3 - \zeta_R^3\right) + \frac{\beta_2}{2}(L^2 - \zeta_R^2) \quad ,
\end{aligned}
\tag{2.4.19}
$$

with $f_n(\zeta)$ and all the constant, as before.
The self-alignment torque can be written in terms of the mean states $\bar{z}_y(t)$ and $\hat{z}_y(t)$ as follows

$$
M_{\text{self-alig}} = -LF_n\Big[\sigma_{0y}\left(\frac{1}{2}\bar{z}_y(t) - \hat{z}_y(t)\right) + \sigma_{1y}\left(\frac{1}{2}\dot{\bar{z}}_y(t) - \dot{\hat{z}}_y(t)\right) + \sigma_{2y}\left(\frac{1}{2}v_{ry} - \frac{G}{F_n L}\right)\Big] \quad . \tag{2.4.20}
$$

A synthetic description of the physical meaning and values of parameters of this model are in Appendix A. These values are obtained by curve fitting in [86], comparing the steady-state characteristics of the model with steady-state data.

### 2.4.3 Model for the sticking torque

In [86], authors propose an average lumped model to describe the friction force generating from the rotation of wheels around the $z$ axis (i.e. the axis perpendicular to the $x-y$ plane, where the patch lies). This phenomenon is known as Sticking friction torque and can be described with the differential equation :

$$\dot{z}_z(t) = \dot{\phi}(t) - \frac{\sigma_{0z}|\dot{\phi}(t)|}{g_z(\dot{\phi}(t))} z_z(t) \tag{2.4.21}$$

where $\sigma_{0z}$ is the normalized rubber stiffness and $\dot{\phi}(t)$ is the angular velocity of the wheel rim, defined as follows

$$\dot{\phi}(t) = \dot{\theta}_s(t)/N_1 \tag{2.4.22}$$

The function $g_z\left(\dot{\phi}\right)$ guarantees steady-state conditions

$$g_z(\dot{\phi}) = \mu_{kz} + (\mu_{sz} - \mu_{kz}) \exp^{-\left(\frac{\dot{\phi}(t)}{\dot{\phi}_s}\right)^2} \tag{2.4.23}$$

Constants $\mu_{kz}$ and $\mu_{sz}$ are, respectively, the kinetic and static friction coefficients on the z-axis ; $\dot{\phi}_s$ is the Stribeck angular velocity.
The sticking torque can be evaluated as follows :

$$M_{sticking} = -LF_n \left[\sigma_{0z} z_z(t) + \sigma_{1z} \dot{z}_z(t) + \sigma_{2z} \dot{\phi}\right] \tag{2.4.24}$$

Hence, the total torque generated by the contact of the tires and the road is :

$$\tau_a = M_{self-alig} + M_{sticking} \tag{2.4.25}$$

### 2.4.4 Parameters setting and improvements to the model of the sticking friction torque

Coefficient $\sigma_{0z}$ affects directly the settling time of the sticking torque. It is important to remark that very fast dynamics make the sticking torque vary in steps. This includes very high frequency components that are likely to cause oscillations and instabilities. Thus, it is advisable to choose a value for $\sigma_{0z}$ low enough to avoid too fast dynamics. In this case the value chosen was $\sigma_{0z} = 20\ \mathrm{m}^{-1}$.

Coefficient $\sigma_{1z}$ is chosen conveniently to avoid overshoot in the dynamics of the sticking torque.

In this thesis, the model of the sticking torque is improved, by introducing the dependence of the model w.r.t. the velocity of the vehicle. It can be proved experimentally that, as the speed of the vehicle grows, the self-alignment torque dominates over the sticking torque, and inversely. Previous model for the sticking torque does not respect this observation in its actual form. It is then necessary to weight the sticking torque in Eq. (2.4.24) as a function the velocity of the vehicle. Thus, the modification that has been done along these observations is the following

$$M_{sticking} = -LF_n \left(\sigma_{0z} z_z + \sigma_{1z} \dot{z}_z + \sigma_{2z} \dot{\phi}\right) \exp^{-|v|/v_k} \tag{2.4.26}$$

where $v_k$ is a positive constant. It is also important to check if results follow the expected logic at the variation of the speed of the vehicle. To achieve to this goal, several simulations are carried out for velocities going from 0 to 30 $\mathrm{km\,h^{-1}}$ and over a time range of several seconds, in order to see the effects at steady-state. The choice of this speed range between 0 and 30 is due to the fact that an EPS system operates in this range. The results obtained from those simulations are shown by Figs. 2.6 and 2.7.

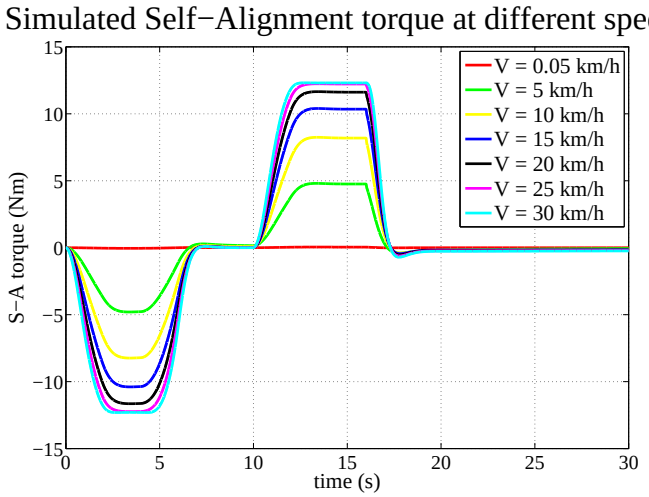


**Figure 2.6** – Simulations of the model of the Self-Alignment torque for different speeds over the range of interest.

Fig. 2.6 shows different curves obtained for the self-alignment torque at different driving speeds, while Fig. 2.7 shows different curves obtained for the sticking torque. Results are as expected : the sticking torque decreases exponentially as the velocity increases, so that the contribution of the self-alignment is more important as the speed increases.

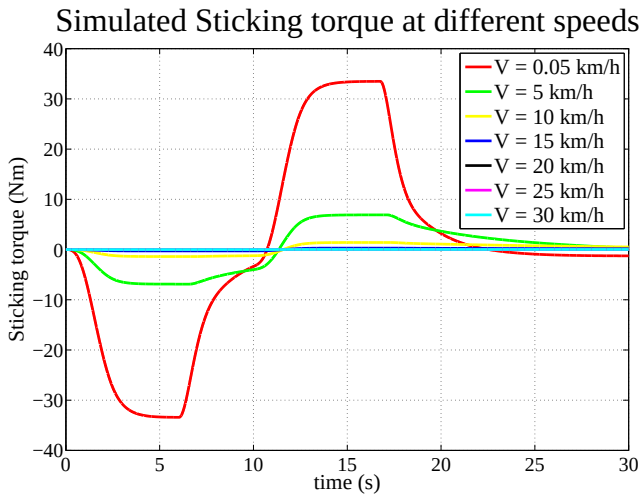


**Figure 2.7** – Simulations of the model of the Sticking torque for different speeds over the range of interest.

## 2.5 Concluding remarks

In this chapter, mathematical equations used to describe the steering system and the tire-road friction torque are introduced. Despite the complexity of the real steering system, it can easily described as a linear, second order system. However, it is necessary to have a realistic model to capture large part of friction phenomena appearing along the steering column until the tire-road contact patch. These phenomena can be described with two dynamic models, that provide the tire-road friction torques for different driving speeds.

# Chapitre 3

# Oscillation annealing and torque observer design

## 3.1 Introduction

This Chapter starts with the analysis of the steering model in open loop under the influence of exogenous inputs. This analysis shows that the this system reacts with undesired oscillations of the steering column. For this reason, a state-controller is proposed to eliminate these oscillations and ensuring the stability of the system. Simulation results in time and frequency domain are proposed to validate improvements brought from the introduction of the state controller on the system in closed loop.

For the main goal of the thesis, it is important to have as much information as possible concerning exogenous inputs acting on the system. In particular, the estimation of the driver's torque can be used as input to produce to correct steering assistance. To this aim, an exogenous input observer is also designed in this Chapter. Finally, simulation results validate performances of the estimation.

## 3.2 State-space representation of the steering system

To begin with, it is essential to recall the mechanical system of the steering column, that has been introduced in Chapter 2. Let us consider mechanical equations Eqs. (2.3.1) and (2.3.2) governing the EPS system.

This system can be described in state-space form, assuming as state-space variables the angular rate of the steering wheel $\dot{\theta}_v$, the angular rate of the column shaft $\dot{\theta}_s$ and the

difference between the steering angle $\theta_v$ and the column-shaft angle $\theta_s$, that is at the origin of the torsional force :

$$x^T = \Big(x_1, x_2, x_3\Big)^T = \Big(\dot{\theta}_v, \dot{\theta}_s, \theta_v - \theta_s\Big)^T \tag{3.2.1}$$

**Remark 3.2.1**

*For sake of simplicity, we will drop the notation "(t)" for time-dependency, e.g. we will use $\dot{\theta}_v$ for $\dot{\theta}_v(t)$.*

The model can be formulated into the state-space form

$$\dot{x} = Ax + Bu + Gw \tag{3.2.2}$$
$$y = Cx + Du \tag{3.2.3}$$

with exogenous inputs

$$w = \Big(\tau_v, \tau_a\Big)^T \tag{3.2.4}$$

and the state-space matrices

$$\begin{aligned} A &= \begin{pmatrix} -\frac{B_v}{J_v} & 0 & -\frac{k}{J_v} \\ 0 & -\frac{N_2^2 B_m}{J_T} & \frac{k}{J_T} \\ 1 & -1 & 0 \end{pmatrix} \quad B = \begin{pmatrix} 0 \\ \frac{N_2}{J_T} \\ 0 \end{pmatrix} \\ G &= \begin{pmatrix} \frac{1}{J_v} & 0 \\ 0 & \frac{1}{N_1 J_T} \\ 0 & 0 \end{pmatrix} = [G_1 \quad G_2] \end{aligned} \tag{3.2.5}$$

The output matrix $C$ is defined in the following Section, while the control to output matrix $D$ is set to 0, because exogenous inputs do not act on the outputs of the system.

### 3.2.1 Influence of driver's exerted torque on the steering system in open loop

Once the state-space representation of the system has been completely defined, it is interesting to observe how the model responds to a variation of the torque exerted by the driver $\tau_v$ on the steering wheel. To do this, it seems appropriate to compute the transfer function between the angular acceleration of the steering wheel $\ddot{\theta}_v$ and the driver's exerted torque $\tau_v$. In literature, this transfer function is often used as a measure of the driving comfort. Such a transfer function can be easily computed from the state-space matrices as follows :

$$G_{ol1} = \frac{\ddot{\theta}_v}{\tau_v} = C(sI - A)^{-1} G_1 \tag{3.2.6}$$

where the output matrix $C$ is given by :

$$C = \begin{pmatrix} -\frac{B_v}{J_v}, & 0, & -\frac{k}{J_v} \end{pmatrix} \tag{3.2.7}$$

Fig. 3.1 shows the frequency response and highlights that the open loop system has a significant peak for a frequency of about 10 Hz, that causes substantial oscillations on the steering wheel and that should be avoided so as to improve driving comfort and safety.

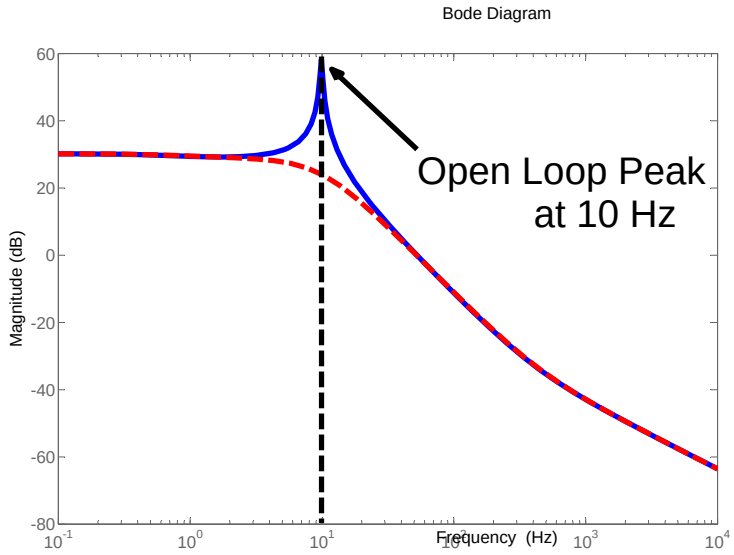


**Figure 3.1** – Frequency response of the transfer functions in open loop (blue) $G_{ol1}$ and in closed loop (dotted red) $G_{cl1}$. They describe the behaviour of the steering system w.r.t. the influence of the driver's torque $\tau_v$.

### 3.2.2 Full-state optimal feedback control

To compensate oscillations of the steering column in open loop, an optimal LQ feedback control is designed. The procedure to obtain this controller is described in the following theorem.

**Theorem 3.2.1 (*Linear Quadratic (LQ) controller*)**

*Given the state-space system*

$$\dot{x}(t) = Ax(t) + Bu(t) \quad \textit{with initial conditions} \quad x(t_0) = x_0 \tag{3.2.8}$$

*the minimization problem*

$$\min_{u^*} J = \min_{u^*} \int_{t_0}^{\infty} u^T(t)Ru(t) + x^T(t)Qx(t)\,\mathrm{d}t \tag{3.2.9}$$

*and matrices $Q > 0$ and $R > 0$, both symmetric and positive semi-definite, the optimal control $u^* = -Kx$ (with $K$ the state-feedback gain) at a given time $t$ is described by*

$$u^*(t) = -R^{-1}B^T P x(t) \tag{3.2.10}$$

*where $P$ satisfies the algebraic Riccati equation :*

$$PA + A^T P - PBR^{-1}G^T P + Q = 0 \quad . \tag{3.2.11}$$

For the synthesis of this controller, the first step is to select the adequate cost function $J$. This function depends from the control problem, that we are dealing with. It may include the penalisation of the only state variables or of the only control variable.
For purposes of this thesis, the cost function to be minimised is in the form :

$$\min_{u^*} J = \min_{u^*} \int_{t_0}^{\infty} q_1(x_1 - x_2)^2 + q_2 x_3^2 + Ru \, \mathrm{d}t \tag{3.2.12}$$

An easy way to obtain the matrix $Q$ is through the output matrix $C_q$, defined as

$$C_q = \begin{pmatrix} q_1 & -q_1 & 0 \\ 0 & 0 & q_2 \end{pmatrix} \tag{3.2.13}$$

Penalised state-matrix $Q$ is calculated as

$$Q = C_q^T C_q = \begin{pmatrix} q_1 & -q_1 & 0 \\ -q_1 & q_1 & 0 \\ 0 & 0 & q_2 \end{pmatrix} \tag{3.2.14}$$

This results in a cost function with three parameters to be tuned. During the process of selection of these parameters, it is compulsory to guarantee that the feedback control does not amplify the steady-state gain of the system. In others words, the impedance between the driver's torque and the tire-road friction torque has not to be modified by the introduction of the state-controller. To this aim, the value $R$ for the penalization of the control input is set to 100 and selected values are $q_1 = 100$ and $q_2 = 0.1$.
The closed-loop transfer function is given by the following equation :

$$G_{cl1} = \frac{\ddot{\theta}_v}{\tau_v} = C(sI - (A - BK))^{-1}G_1 \quad , \tag{3.2.15}$$

with $A - BK$ the closed-loop state space matrix.
The benefits of this design can be observed on the dotted curve in Fig. 3.1. The resonance peak that might cause undesirable oscillations has been eliminated thanks to the proposed optimal linear control. Also note that the low-frequency gain has remained unchanged.

**Remark 3.2.2**

*State-feedback control has an interesting and useful side-effect : it allows us to neglect the stiffness of the steering column and, consequently, the influence of the torsion force. In this way, it is possible to write the model of the EPS in Eqs. (2.3.1) and (2.3.2) in a reduced form, as it will be shown in Chapter 4.*

### 3.2.3 Optimal "output" feedback controller

All the calculations carried out until now assumed that the whole set of state-space variables was measurable. Nevertheless, on commercial products only the motor angle $\theta_s$ with its derivative $\dot{\theta}_s$ and the torsion force $F_t$ are measured. This is due to the fact that installation of additional sensors implies an important extra cost that should be, if possible, avoided.

The previous control problem can be reformulated by assuming only that the motor speed (approximated from motor position sensor) is available. This means that the only available output is

$$y_1 = C_1 x = \begin{pmatrix} 0, & 1, & 0 \end{pmatrix} x = \dot{\theta}_s \tag{3.2.16}$$

In order to recover non-measurable states of the system, a state-observer is synthesized. Assuming as before (this assumption will be relaxed later) that exogenous inputs $w$ are measured as well, then the proposed observer has the following form

$$\dot{\hat{x}} = (A - LC_1)\hat{x} + Bu + Gw + Ly \quad , \tag{3.2.17}$$

where $L$ is the observer gain to be designed. By the separation principle, the control $K$ is kept as before, and $L$ can be designed either via pole placement method, or via the loop-recovering strategy ([47], [48]). In any case, it is necessary that dynamics of the observation error

$$\dot{\hat{x}} - \dot{x} = \dot{e} = (A - LC_1)e \tag{3.2.18}$$

are fast enough to provide a fast convergence of the observer towards the real states.

### 3.2.4 Simulation results in time domain

In order to see the performance of the proposed controller and observer, simulations are carried out using as input to the system the driver's exerted torque profile, shown in Fig. 3.2. Note that this profile is designed in order to simulate the effect that the driver turns the steering wheel for 16 s, then he releases it.

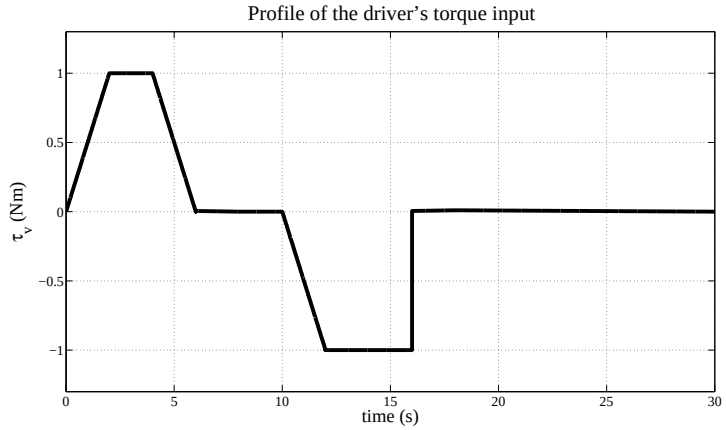


**Figure 3.2** – Profile of the driver's exerted torque used as input to the EPS system.

The first simulation concerns the system in open loop. As shown in Fig. 3.3, when the driver releases the steering wheel at the time instant $16s$, the steering system suffers significant oscillations that would cause an undesirable driving feeling and might even be dangerous at high speeds.

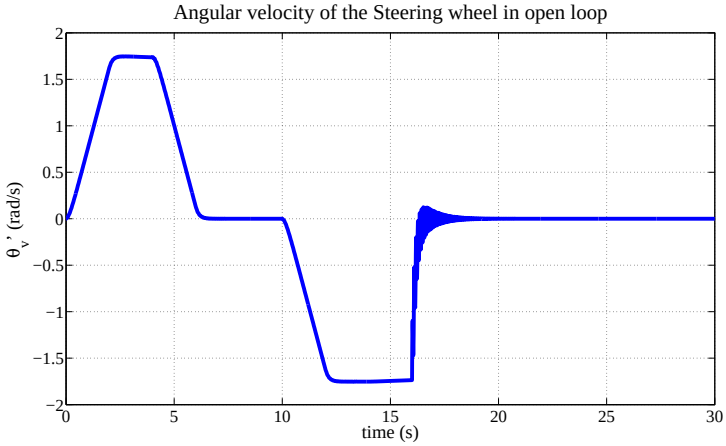


**Figure 3.3** – Profile of the angular speed of the steering wheel in open loop.

A zoom on these oscillations is shown in Fig. 3.4, where it is possible to see how the steering wheel oscillates until all the mechanical energy is dissipated.

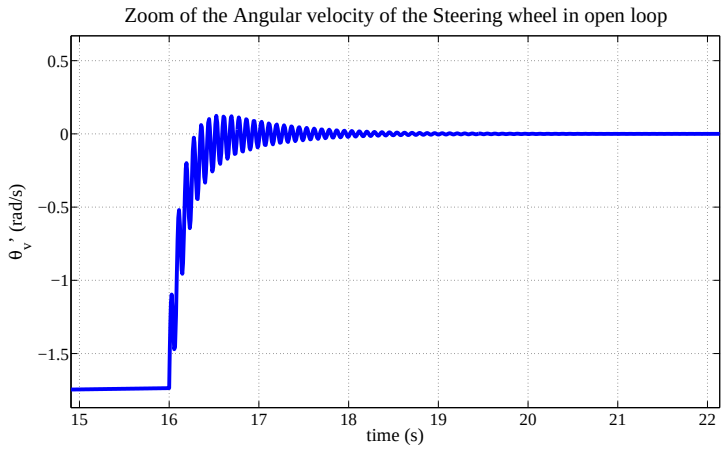


**Figure 3.4** – (Zoom on oscillations of the angular speed of the steering wheel, caused by the effect to release the steering wheel.

The optimal linear controller computed before has the aim to eliminate oscillations found in open loop thanks to the assistance motor. As shown at the Fig. 3.5, oscillations derived from the release of the steering wheel have been satisfactorily compensated by the optimal controller.

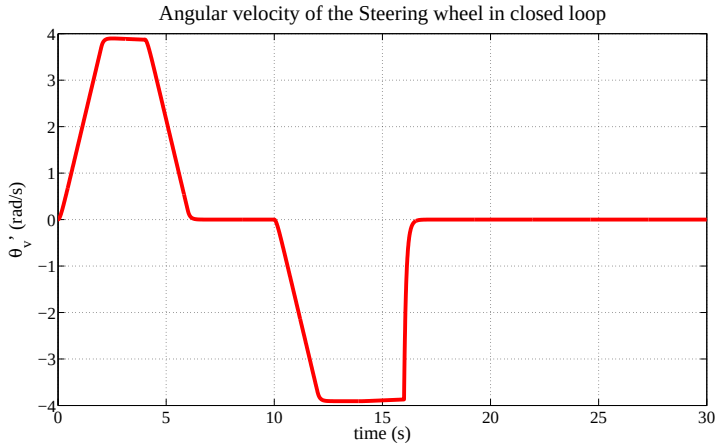


**Figure 3.5** – Profile of the angular speed of the steering wheel in closed loop.

The behaviour of the observer is shown by Fig. 3.6. From this figure it is possible to see that the performance of the observer is completely satisfactory.

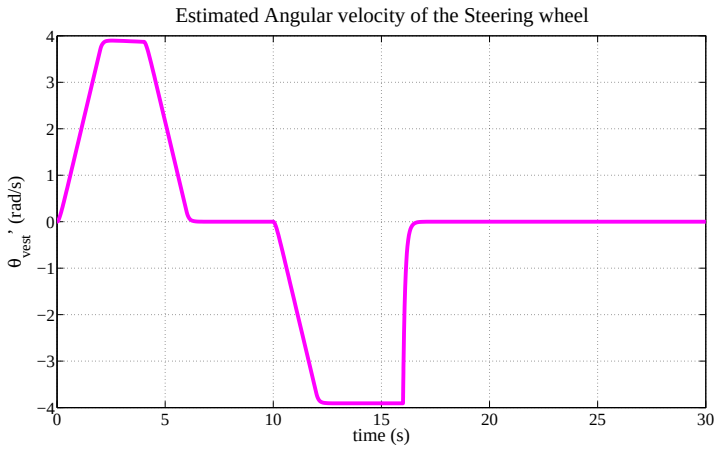


**Figure 3.6** – Estimation of the angular speed of the steering wheel.

## 3.3 Exogenous torques estimation

The observer described in the previous paragraph was designed on the basis of the assumption that the exogenous inputs were measured. This assumption cannot be verified on real system and needs to be relaxed.

The purpose of this paragraph is to develop an observer that includes also the estimation of the exogenous torques appearing on the system in addition to the estimation of the state variables of the system. Both $\tau_v$ and $\tau_a$ are not sensed *a priori* and it could be interesting to know their evolution. The more information is known about the system, the better it is for the analysis. Furthermore, if these estimations are successful, they can be used for the development and implementation of driver's assistance laws.

### 3.3.1 Extended state-space representation

To develop this observer, let us make the assumption that both exogenous torques are slowly time-varying

$$\dot{\tau}_a \approx 0, \quad \dot{\tau}_v \approx 0 \tag{3.3.1}$$

and they are assumed as further state-space variables of the original system in Eq. (3.2.5). Under this assumption, it is possible to extend the original system and to build a new state-observer for the extended system. Another interesting fact, which is a side effect, is that the observer not only provides the original control-states estimates but also provide an estimate of the driver's delivered torque, and the contact tire/road friction forces.

The extended state-space vector $z$ for the torque observer design is now defined as,

$$\tilde{z} = \left(\dot{\theta}_v, \dot{\theta}_s, \theta_v - \theta_s, \tau_v, \tau_a\right)^T \tag{3.3.2}$$

in which both exogenous torques are added as state variables.
The complete state-space representation is given by

$$\dot{\tilde{z}} = \tilde{A}_e \tilde{z} + \tilde{B}_e u \tag{3.3.3}$$

where the state-matrices are given by

$$\tilde{A}_e = \begin{pmatrix} A & G \\ \mathbb{O}_{2\times 3} & \mathbb{O}_{2\times 2} \end{pmatrix}, \quad \tilde{B}_e = \begin{pmatrix} B \\ 0 \\ 0 \end{pmatrix}, \tag{3.3.4}$$
$$C_e = \begin{pmatrix} C & 0 & 0 \end{pmatrix},$$

where $\mathbb{O}_{n\times m}$ denotes a $nxm$ all-zero matrix.

Besides the slow-varying hypothesis, the condition to respect to be able to estimate the exogenous input is that the extended system is observable. To respect this condition, the observability matrix must have full rank and equal to the number of states of the system ([47], [48]).

If only the motor velocity is used as an available output, as defined in Eq. (3.2.16), then the observability matrix for this new extended system has rank 4 in spite of dealing with a system of dimension 5. Under this condition, it is not possible to design an observer for the extended system.

### 3.3.2 Using the torsion force as an additional output

Although it has been so far considered that the only measurable variable was the angular velocity of the assistance motor, it is possible to measure a second signal as well : the torsion force,

$$y_2 = k(\theta_v - \theta_s) = kx_3. \tag{3.3.5}$$

In this case, the output matrix $C_e$ of the extended system becomes

$$\tilde{C}_e = \begin{pmatrix} 0 & 1 & 0 & 0 & 0 \\ 0 & 0 & k & 0 & 0 \end{pmatrix}. \tag{3.3.6}$$

Computing the new resulting observability matrix, it is easy to check that it has now full rank. The system is then observable and both exogenous torques can be correctly estimated.

The method used to design the observer's gain is analogue to the one used in Section 3.2.3, i.e., the poles of the dynamics of the observer (matrix $\tilde{A}_e - L_e\tilde{C}_e$) should be fast enough compared to those resulting from the linear controller.

Performance of the observer has been tested in simulations, using the realistic tire-road friction torque, shown in Paragraph 2.4.

Results obtained for the estimation of $\tau_v$ and $\tau_a$ are shown in Fig. 3.7(a) and Fig. 3.7(b). They show how the observer reconstructs perfectly exogenous input torques. The maximum value reached by the observation error can be reduced at the price of increasing the observer gain. At some point, measurement noise will limit the maximum possible value of the observer gain.

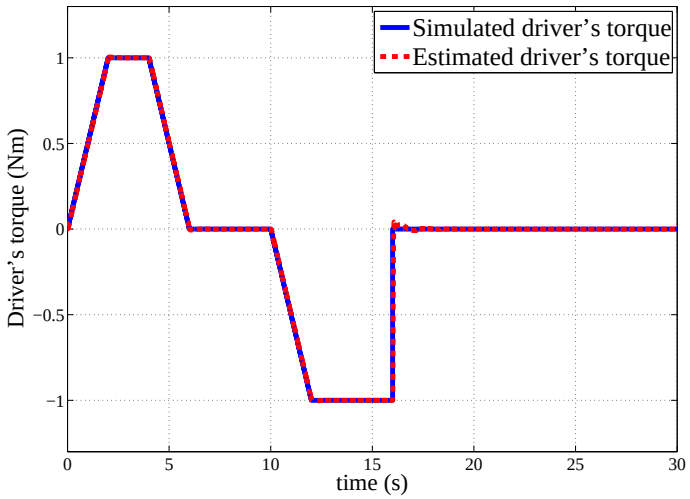


(a)

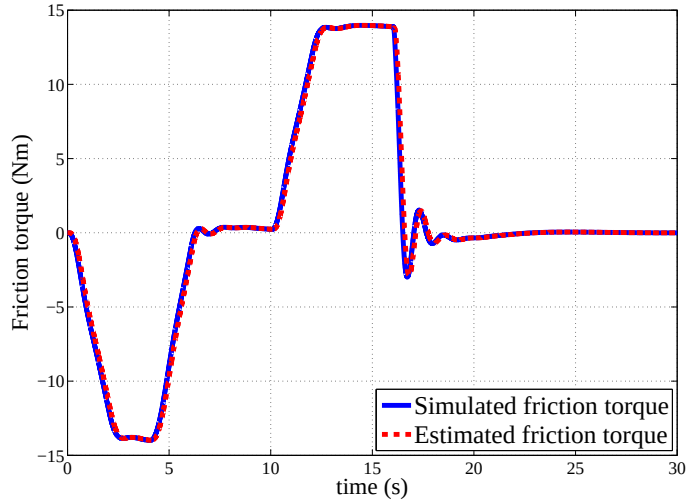


(b)

**Figure 3.7** – (a) Real driver's torque (solid) vs. estimated driver's torque (dotted). (b) Real load torque (solid) vs. estimated load torque (dotted).

## 3.4 Concluding remarks

This chapter presented an exhaustive analysis of the steering system in open and in closed loop. In open loop, the influence of exogenous inputs results in undesirable oscillations of the steering column. These oscillations can be attenuated in closed loop, under the influence of an optimal state controller. The state controller deletes oscillations of the steering column, but does not modify the steady-state impedance of the system.
Simulations in frequency domain and time domain have been carried on to validate the state controller. In both domains, performances of the controller are satisfying.

A state observer has been designed to recover inner states of the system. In the first part, the observer has been designed under the assumption of a perfect knowledge of the exogenous inputs acting on the system. In the second part, this assumption has been relaxed, and a new observer has been designed, including the estimation of exogenous inputs. This observer has been evaluated via simulation in closed-loop, showing good results and good estimation characteristics.

# Chapitre 4

# Power steering booster stage

## 4.1 Introduction

Power steering assistance is typically provided by EPAS systems, through the use of amplification maps. In literature, they are generally known as booster curves and they are modelled as mathematical functions of the driver's torque and the speed of the vehicle, as described in Paragraph 1.2.2.

The first aim of this Chapter is to find a justification to the use of these curves. Investigations about the state-of-art of EPAS systems do not provide evidence that they are optimal for the driver in any sense. This part of the chapter generates an optimal relation between the driver's exerted torque and the steering assistance, based on a minimizing criterion corresponding to relevant human parameters, and compares it with classical maps.

In the second part of the Chapter, the modification of these curves is developed to adapt them to drivers with reduced mobility. To this goal, first, a general methodology is proposed. Second, it is used for illustrating the procedure on a case study of interest. Finally, simulation results of the new steering assistance in the context of the general control architecture conclude this Chapter.

## 4.2 Genesis of booster curves in EPAS systems

Investigations about standard booster curves, which are commonly use to produce the steering assistance, do not provide a strong justification to the use of these curves, other than they reproduce the behaviour of the older power steering systems, based on hydraulic valves.

In literature, there is no reflection that may link the driver's steering feel, his neurological functions, his bio-mechanical behaviour and the suited steering assistance. As the future generation of EPAS systems should be designed to keep into account exigences of different kinds of population, it is suited to better understand what is the relationship between the driver's steering feel and the steering assistance. The following of this Chapter represents a first attempt in this sense.

In others words, the proposed procedure aims for providing some rationality to standard booster curves and validating their optimality for the drivers. To this aim, it is interesting to refer to the literature concerning criteria at the basis of the human coordination, that try to explain the human movement by minimizing a cost function. These criteria can be divided in two main classes :

– Dynamic optimization criteria aim to minimize quantities like human energy or power ([57], [58]), the torque and the torque change [70] exerted during a movement. These kinds of criteria are widely used to describe exercises with a consistent muscular activity and consequently muscular effort (e.g., riding or walking).
– Kinematic criteria aim to minimize quantities describing laws of the motion. Most common cost function is based on the minimization of the jerk (rate of change of acceleration). This function is widely used in literature to describe human pointing, because authors assume that the major goal of motor coordination is the production of a movement, that is as smoothest as possible ([40], [35], [9], [16]).

A typical driving task is a precise movement, but it does not require a great driver's effort. For this reason, the hypothesis at the basis of our reflection is that driver's coordination provide a movement on the steering wheel that minimize the criterion based on the jerk. The movement that we take into account starts with the steering wheel in an initial position, then the steering wheel is first turned to reach a final position and finally it is brought to the initial position. This trajectory has been chosen because it corresponds to a standard motion during a parking manoeuvre, but also because it allows to develop the complete profile of booster curves for positive and negative values of the driver's exerted torque.

Solving this optimization, it is possible to find the shape of the booster curve, that allows to minimise the jerk criterion and to keep a good perception of the driving task.

### 4.2.1 Analysis of torques acting on the EPS system

#### 4.2.1.1 Steering column torques

Let us consider the original EPS system in Eqs. (2.3.1) and (2.3.2). Let us make the hypothesis that the stiffness $k$ of the steering column is infinity or that its effect can be compensated as proposed in Chapter 3. In this case, it is possible to neglect the torsion

of the column $\theta_v - \theta_s = 0$ and to consider the equivalent steering wheel angle $\theta_v = \theta_s = \theta$. Summing Eq. (2.3.1) with Eq. (2.3.2), it is possible to obtain :

$$J\ddot{\theta} + B\dot{\theta} + \frac{\tau_a}{N_1} = \tau_v + U \tag{4.2.1}$$

where $J = J_v + J_T$ and $B = B_v + N_2^2 B_m$ are, respectively, the total inertia and the total viscosity of the system at the steering wheel level. The input $U = N_2 u$ corresponds to the assistance provided by the electrical motor, acting on the steering column.

From Eq. (4.2.1) arises that at stand-still, (or very low vehicle speeds, that is the common situation where the assistance acts), the most important torque opposing to the driver's torque is the contact friction torque. To this aim, the self-alignment torque shown in Section 2.4.2 is close to zero for the speed range of interest. For this reason, it is not considered in this problem. It is possible to proof that for cruise speeds of the vehicle close to zero, the sticking torque, that is shown in Section 2.4.3, behaves as the Dahl's tire-road friction torque. For this reason, in this part of the thesis the Dahl's friction model is used. This model has as advantage a closed-form solution for its differential equation, that can be easily introduced into the optimization procedure proposed to obtain dynamic booster curves.

#### 4.2.1.2 Contact friction torque at stand-still

The dynamic Dahl's model ([32], [30], [31]) is given by the following differential equation

$$\frac{\mathrm{d}F}{\mathrm{d}\theta_1} = \sigma_0 \left[1 - \frac{F}{F_c} \operatorname{sgn}\left(\dot{\theta}_1\right)\right] \tag{4.2.2}$$

where $\sigma_0$ is the rubber longitudinal stiffness coefficient, $F_c$ is the Coulomb friction force and $\theta_1 = \theta / N_1$ is the angular position of the steering wheel projected at the tire level and $\dot{\theta}_1$ is its derivative.

Main feature of this model is that the friction force $|F|$ will never be larger than the steady-state Coulomb friction force $F_c$, if its initial value is $|F(0)| < F_c$.

To obtain the equivalent time-domain model, the following change of coordinates is required

$$\frac{\mathrm{d}F}{\mathrm{d}t} = \frac{\mathrm{d}F}{\mathrm{d}\theta_1}\frac{\mathrm{d}\theta_1}{\mathrm{d}t} = \frac{\mathrm{d}F}{\mathrm{d}\theta_1}\dot{\theta}_1 = \sigma_0 \left[1 - \frac{F}{F_c} \operatorname{sgn}(\dot{\theta}_1)\right] \dot{\theta}_1 \tag{4.2.3}$$

The load torque $\tau_a$ in Eq. (4.2.1) can be expressed as a function of $F$, as follows

$$\tau_a = F_n L F \tag{4.2.4}$$

where $F_n$ and $L$ are, respectively, the normal force and the patch length.
For a constant speed $\dot{\theta}_1 = \bar{\dot{\theta}}_1$, it is possible to obtain the following steady-state friction

force $\bar{F}$

$$\bar{F} = \sigma_0 \bar{z} = F_c \, \mathrm{sgn}(\dot{\bar{\theta}}_1) \tag{4.2.5}$$

This model is a first-order dynamic system and its steady-state behaviour gives the Coulomb friction force, as shown in Eq. (4.2.5).

For this model, it is possible to compute the solution of its differential equation in closed form for a sign-changing speed signal. Let us consider the steering movement shown in Fig. 4.1. Let us consider a time interval $t \in [0, t_1]$, where the speed signal is positive and

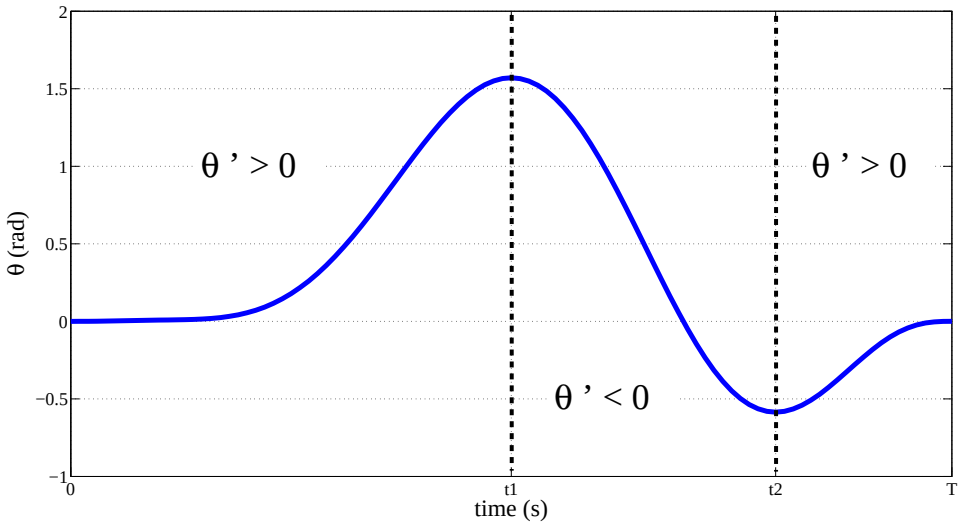


**Figure 4.1** – Profile of the movement on the steering wheel, that is used to calculate the analytical solution of the Dahl's friction model.

the system starts with the initial conditions, i.e. $F(\theta_0) = 0$ and $\theta(0) = \theta_0$, the solution is :

$$F_1(t) = F_c \left[ 1 - \exp^{-\frac{\sigma_0}{F_c}\left(\frac{\theta(t)-\theta_0}{N_1}\right)} \right] \tag{4.2.6}$$

If the speed signal becomes negative during a time interval $t \in [t_1, t_2]$, then the solution is :

$$F_2(t) = F_c \left[ -1 + 2\exp^{\frac{\sigma_0}{F_c}\left(\frac{\theta(t)-\theta(t_1)}{N_1}\right)} - \exp^{\frac{\sigma_0}{F_c}\left(\frac{\theta(t)-2\theta(t_1)}{N_1}\right)} \right] \tag{4.2.7}$$

Note that this solution is evaluated starting from initial conditions, that guarantee the continuity of the solution at the time instant $t_1$, when the sign change of the speed happens. Finally, if the speed changes again in sign, during the time interval $t \in [t_2, T]$, the solution is :

$$F_3(t) = F_c \left[ 1 - 2\exp^{-\frac{\sigma_0}{F_c}\left(\frac{\theta(t)-\theta(t_2)}{N_1}\right)} + 2\exp^{-\frac{\sigma_0}{F_c}\left(\frac{\theta(t)+\theta(t_1)-2\theta(t_2)}{N_1}\right)} - \exp^{-\frac{\sigma_0}{F_c}\left(\frac{\theta(t)+2\theta(t_1)-2\theta(t_2)}{N_1}\right)} \right] \tag{4.2.8}$$

Details about the computation of previous analytical solutions are shown in Appendix A.3. For purposes of this thesis, the computation of the analytic solution is limited to three consecutive sign changes of the speed, but the proposed method can be applied even for more general cases. To compute the analytic solution, the time instant when the sign change takes place must be known. The friction force is only a function of the displacement and the sign of the relative velocity. This implies that it will depend only from the sign of the velocity, but not from its magnitude.

### 4.2.2 Perception of the load torque and assistance torque definition

At stand still, the main force opposing to the driver's effort is the contact friction. In this situation, it is possible to assume that the assistance $U$ acts to compensate, first of all, a part of the contribution of the load torque $\tau_a$ in Eq. (4.2.1). Indeed at steady-state conditions :

$$\frac{\tau_a}{N_1} = \tau_v + U \tag{4.2.9}$$

In order to design the assistance amplification, the hypothesis that the driver's perception of the load torque obeys to the Stevens' power law ([69], [29], [7]) is done. According to the power law, sensation magnitudes grow as power functions of stimulus intensities that produce them. This law was first proposed by S.S. Stevens for light and sound. Subsequently, Stevens suggested it as a general law describing quantitatively relationships between human sensations as well as other subjective impressions and the physical stimuli, that evoke them [95]. According to the proposed law, the relationships approximate power functions of the form (see also Fig. 4.2)

$$\psi = \delta\phi^n \tag{4.2.10}$$

where $\psi$ stands for the sensation magnitude, $\phi$ is the magnitude of the physical stimulus, $\delta$ is the intensity magnitude of the stimulus and $n$ describes the rate of growth of the sensation of the stimulus and depends on the sensory modality of the driver (e.g. perception of force or perception of position). Let us apply this law to the case of the perception of the friction torque

$$\tau_v = \delta \left( \frac{\tau_a}{N_1} \right)^n \tag{4.2.11}$$

The value of $\delta$ is tuned to obtain a realistic value of the amplification torque, while to choose the value of $n$, it is mandatory to refer to the literature, concerning the control of the movement and to some experimental results.

During the steering movement, some authors ([41], [75]), show that drivers prefer exerting their control, basing on the transfer function between the friction contact load and the

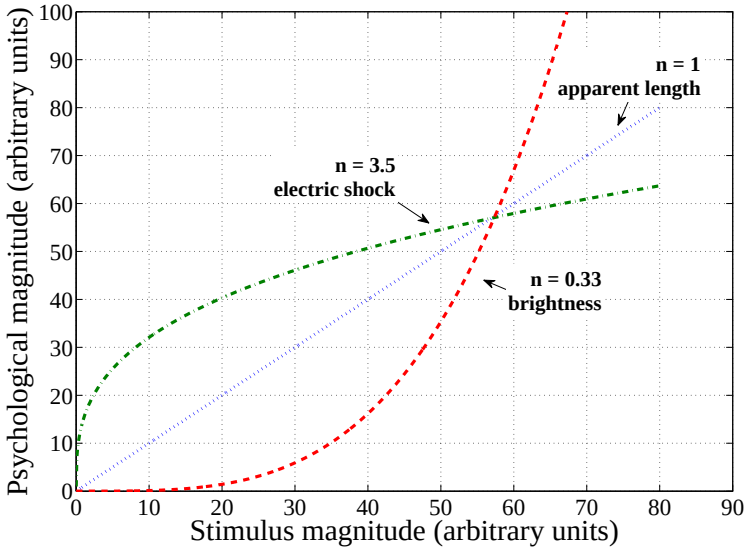


**Figure 4.2** – The apparent magnitudes of electric shock, length and brightness follow different curves of growth, because their power law exponents are 3.5, 1.0 and 0.33, respectively. Note how the curve is concave upward or downward, depending on whether the exponent is greater or less than 1.0. The units of the scales have been chosen arbitrarily in order to show the relative form of the curves on a single graph.

steering angle (*position-oriented control*), rather than the transfer function between the friction torque and the steering torque (*torque-oriented control*). This can be explained by the fact that the neuro-muscular system is better suited to control the steering angle than the exerted torque, thanks to the gamma ($\gamma$) motor neurons, that adapt the length of the spindles according to the hand wheel angle [75].

In [69], authors determine experimentally the value of $n$ for both cases of torque-oriented and position-oriented control. For each case, they produce 3 experiments.
In particular, for what concerns the position-oriented control, during the first experiment they require to 12 subjects to make a numerical estimation of the perceived magnitude of sensation. During the second one, they require to the same subjects to adjust the stimulus to produce a sensory magnitude equivalent to given numbers. Finally, they employ both magnitude estimation and magnitude production to develop a scale of perception of steady-state steering wheel angle.
The value of the rate $n$ is determined by least square identification of the real data with Stevens' power law. They obtain an average value of $n = 0.93$, that is $n < 1$, meaning that the sensation of the angle grows at a slower rate than the angle.
Considering what has been highlighted to this point, in this case a position-oriented control is considered and simulations are provided for values of $n \leq 1$.

To obtain a relation between the assistance torque and the driver's torque in steady-state,

Eq. (4.2.9) is substituted in Eq. (4.2.11), as follows

$$\delta \left(\tau_v + U_{ss}\right)^n = \tau_v \quad . \tag{4.2.12}$$

It leads to the expression in steady-state

$$U_{ss} = \sqrt[n]{\frac{\tau_v}{\delta}} - \tau_v \tag{4.2.13}$$

When the dynamic terms of inertia and viscosity are included, we make the hypothesis that they add to the steady-state perception

$$J\ddot{\theta} + B\dot{\theta} + \delta \left(\frac{\tau_a}{N_1}\right)^n = \tau_v \quad . \tag{4.2.14}$$

Consequently, let us consider Eq. (4.2.1) and we can express the assistance torque $U$, as the following difference :

$$U = \frac{\tau_a}{N_1} - \delta \left(\frac{\tau_a}{N_1}\right)^n \quad . \tag{4.2.15}$$

Note that this expression is valid in all conditions. The assistance $U$ is directly linked to the value of the tire-road friction torque $\tau_a$ and to the acceleration and the velocity of the steering wheel ($\ddot{\theta}$ and $\dot{\theta}$). It is then necessary to calculate these values, in order to retrieve the corresponding assistance. To this goal, an optimization problem is introduced in Section 4.2.3.

### 4.2.3 Optimal problem formulation

Concerning the driving task, some authors formulated a position-oriented control ([41], [75]), that is in accordance with the kinematic optimization criteria. For this reason to obtain the profile of the booster curves for the dynamic case, an optimization problem basing on the minimization of the jerk function is here formulated.

The considered movement reproduces a standard parking manoeuvre and consists into bringing the steering wheel from 0 rad to $\pi/2$ rad and returning it to its initial position. The problem is to find the optimal trajectory $\hat{\theta}$, that minimizes the cost index $I$

$$I = \int_0^T \left(\frac{\mathrm{d}^3\theta}{\mathrm{d}t^3}\right)^2 \mathrm{d}t \tag{4.2.16}$$

under the constraint to have a driver's torque $\tau_v(0) = \tau_v(T) = 0$. These lasts are imposed on $\tau_v$ through Eq. (4.2.14), where the time-dependency is given from the state-variables ($\ddot{\theta}$ and $\dot{\theta}$).

To generalize the problem, the normalized form of the time is adopted

$$t^* = \frac{t}{T} \tag{4.2.17}$$

where $T$ is the final simulation time, considered to execute the movement. Differentiating this time, it is possible to get :

$$\mathrm{d}t^* = \frac{\mathrm{d}t}{T} \tag{4.2.18}$$

In the new set of coordinates, the equation of the model becomes :

$$\frac{J}{T^2}\frac{\mathrm{d}^2\theta^*}{\mathrm{d}t^{*2}} + \frac{B}{T}\frac{\mathrm{d}\theta^*}{\mathrm{d}t^*} + \delta\left(\frac{\tau_a}{N_1}\right)^n = \tau_v^* \quad . \tag{4.2.19}$$

The only time-invariant term in Eq. (4.2.19) is the friction torque, while the total inertia and the total viscosity decrease as slower the driver executes the movement.

In the normalized form of the time, the optimization problem becomes

$$\min_{\hat{\theta}^*} \int_0^1 \left(\frac{\mathrm{d}^3\theta^*}{\mathrm{d}t^{*3}}\right)^2 \mathrm{d}t^* \tag{4.2.20}$$

with the boundary conditions on the trajectory

$$\begin{aligned} &\theta^*(0) = 0 \quad \theta^*(1) = 0 \quad \theta^*(0.5) = \pi/2 \\ &\dot{\theta}^*(0) = 0 \quad \dot{\theta}^*(1) = 0 \quad \dot{\theta}^*(0.5) = 0 \\ &\ddot{\theta}^*(0) = 0 \quad \ddot{\theta}^*(1) = 0 \end{aligned} \tag{4.2.21}$$

and on the driver's torque

$$\tau_v^*(0) = 0 \quad \tau_v^*(1) = 0 \quad , \tag{4.2.22}$$

defined by Eq. (4.2.19). The condition $\tau_v^*(0) = 0$ is guaranteed by the constraint to impose that the movement begins with speed and acceleration null and by the initial condition imposed on the friction torque $F(0) = 0$. In the same way, to guarantee the condition $\tau_v^*(1) = 0$, it is mandatory to impose that the load torque $\tau_a$ must be null at the final time $\tau_a(1) = 0$, that implies $F(1) = 0$.

As the optimization procedure will use the analytic solution of the Dahl's friction torque, the constraint $F(1) = 0$ can be imposed on the function in Eq. (4.2.8), obtained for $t \in [t_2, 1]$, as follows :

$$F_3(1) = F_c\Big[1 - 2\exp^{-\frac{\sigma_0}{F_c}\left(\frac{\theta^*(1)-\theta^*(t_2^*)}{N_1}\right)} + 2\exp^{-\frac{\sigma_0}{F_c}\left(\frac{\theta^*(1)+\theta^*(t_1^*)-2\theta^*(t_2^*)}{N_1}\right)} - \exp^{-\frac{\sigma_0}{F_c}\left(\frac{\theta^*(1)+2\theta^*(t_1^*)-2\theta^*(t_2^*)}{N_1}\right)}\Big] = 0 \tag{4.2.23}$$

Using the boundary conditions imposed on the optimization problem, the values of $\theta^*(1)$ and $\theta^*(t_1^*)$, respectively, zero and $\pi/2$ rad, can be substituted in Eq. (4.2.23), and the only unknown variable becomes the angle $\theta^*(t_2^*)$ :

$$F_3(1) = F_c\Big[1 - 2\exp^{\frac{\sigma_0}{F_c}\frac{\theta^*(t_2^*)}{N_1}} + 2\exp^{-\frac{\sigma_0}{F_c}\left(\frac{\frac{\pi}{2}-2\theta^*(t_2^*)}{N_1}\right)} - \exp^{-\frac{\sigma_0}{F_c}\left(\frac{\pi-2\theta^*(t_2^*)}{N_1}\right)}\Big] = 0 \tag{4.2.24}$$

Setting

$$x = \exp^{\frac{\sigma_0}{F_c}\frac{\theta^*(t_2^*)}{N_1}} \quad , \tag{4.2.25}$$

Eq. (4.2.24) can be written as the following second order algebraical equation :

$$1 - 2x + \left(2\exp^{-\frac{\sigma_0}{F_c}\frac{\pi}{2}\frac{1}{N_1}} - \exp^{-\frac{\sigma_0}{F_c}\frac{\pi}{N_1}}\right)x^2 = 0 \tag{4.2.26}$$

This equation is in the standard form

$$ax^2 + bx + c = 0 \tag{4.2.27}$$

with $a = 1$, $b = -2$ and $c = \left(2\exp^{-\frac{\sigma_0}{F_c}\frac{\pi}{2}\frac{1}{N_1}} - \exp^{-\frac{\sigma_0}{F_c}\frac{\pi}{N_1}}\right)$, respectively.
If $b \neq 0$ and $c \neq 0$, solutions of this equation are given from

$$x_{1,2} = \frac{-b \pm \sqrt{b^2 - 4ac}}{2a} \quad . \tag{4.2.28}$$

We choose the positive solution $x_1 > 0$. By inverting Eq. (4.2.25), it is possible to obtain the optimal angular position as follows

$$\theta^*(t_2^*) = \frac{F_c N_1}{\sigma_0}\log x_1 \tag{4.2.29}$$

Using this value, it possible to impose a further boundary condition on the trajectory, that guarantees $F(1) = 0$

$$\theta^*(t_2^*) = \theta_2 \tag{4.2.30}$$

#### 4.2.3.1 Static optimization problem

The problem to solve is a dynamic, non-linear, constrained optimization problem. A method to solve this problem consists into transforming it into a static, non-linear, constrained optimization problem and to calculate the optimal solution for this problem [8].
Let make the hypothesis that among the set of the feasible solutions, the optimal one has the following polynomial form :

$$\theta^*(t^*) = a_0 + a_1 t^* + a_2 t^{*2} + a_3 t^{*3} + \ldots a_{p-1} t^{*p-1} + a_p t^{*p} \tag{4.2.31}$$

where $p$ is the order of the polynomial and $a_p$ is each single coefficient of the polynomial. Derivatives of Eq. (4.2.31) provide the analytical expressions for $\dot{\theta}^*(t^*)$ and $\ddot{\theta}^*(t^*)$ and the jerk

$$\dot{\theta}^*(t^*) = a_1 + 2a_2 t^* + 3a_3 t^{*2} + \ldots (p-1)a_{p-1} t^{*p-2} + p a_p t^{*p-1} \tag{4.2.32}$$

$$\ddot{\theta}^*(t^*) = 2a_2 + 6a_3 t^* + \ldots (p-1)(p-2)a_{p-1} t^{*p-3} + p(p-1)a_p t^{*p-2} \tag{4.2.33}$$

$$\frac{\mathrm{d}^3\theta(t^*)}{\mathrm{d}t^{*3}} = 6a_3 + \ldots (p-1)(p-2)(p-3)a_{p-1}t^{*p-4} + p(p-1)(p-2)a_p t^{*p-3} \quad (4.2.34)$$

New optimization problem is obtained by substituting Eq. (4.2.34) in the Eq. (4.2.20) of the cost function

$$\min_{\hat{\theta}^*} \sum_{t^*=0}^{1} \left[6a_3 + \ldots (p-1)(p-2)(p-3)a_{p-1}t^{*p-4} + p(p-1)(p-2)a_p t^{*p-3}\right]^2 \Delta t^* \quad (4.2.35)$$

with $\Delta t^*$ the sample time of the algorithm. Let us also substitute Eqs. (4.2.31), (4.2.32) and (4.2.33) in Eqs. of the boundary conditions (4.2.21), (4.2.30) on the trajectory, as follows :

$$\begin{aligned}
&\theta^*(t^*=0) = a_0 = 0\\
&\dot{\theta}^*(t^*=0) = a_1 = 0\\
&\ddot{\theta}^*(t^*=0) = 2a_2 = 0\\
&\theta^*(t^*=1) = a_0 + a_1 + a_2 + a_3 + \ldots a_{p-1} + a_p = 0\\
&\dot{\theta}^*(t^*=1) = a_1 + 2a_2 + 3a_3 + \ldots (p-1)a_{p-1} + pa_p = 0\\
&\ddot{\theta}^*(t^*=1) = 2a_2 + 6a_3 + \ldots (p-1)(p-2)a_{p-1} + p(p-1)a_p = 0\\
&\theta^*(t^*=0.5) = a_0 + a_1 0.5 + a_2 0.5^2 + a_3 0.5^3 + \ldots a_{p-1}0.5^{p-1} + a_p 0.5^p = \pi/2\\
&\dot{\theta}^*(t^*=0.5) = a_1 + 2a_2 0.5 + 3a_3 0.5^2 + \ldots (p-1)a_{p-1}0.5^{p-2} + pa_p 0.5^{p-1} = 0
\end{aligned} \quad (4.2.36)$$

Let us also impose the boundary condition $\tau_v^*(1) = 0$ with

$$\begin{aligned}
\tau_v^*(1) = &\frac{J}{T^2}\left[2a_2 + 6a_3 + \ldots (p-1)(p-2)a_{p-1} + p(p-1)a_p\right]\\
&+ \frac{B}{T}\left[a_1 + 2a_2 + 3a_3 + \ldots (p-1)a_{p-1} + pa_p\right] + \delta\left(\frac{\tau_a}{N_1}\right)^p
\end{aligned} \quad (4.2.37)$$

where the tire-road friction torque $\tau_a$ is obtained from the analytic solutions of the Dahl's model for the intervals of interest (Eqs. (4.2.6), (4.2.7) and (4.2.8). In these equations, polynomial trajectories of the steering wheel are also substituted.

Last boundary condition to impose is on the position $\theta^*(t_2^*) = \theta_2$. Note that this condition is verified inside an additional dichotomy loop to find the optimal time instant $t_2^*$, when the steering wheel path may assume this value minimizing the cost function. According to the constraints of the problem, it is only possible to predict that this instant will be during the second part of the movement for $t_1^* < t_2^* < 1$, but it is not to possible to say more about. The implementation in pseudo-code of this loop is shown in Appendix A.

The optimization algorithm looks for the combinations of the polynomial $a_k$ with $k = 0 \ldots p$, that minimize the cost function. Remark that 9 boundary conditions are imposed ; as consequence, the degree of the polynomial must be greater $p > 9$ in order to allow

to the optimization procedure to choose among different solutions. However, a too high order for the polynomial could cause instabilities in the solution. For this reason, the chosen order is $p = 12$.

### 4.2.4 Simulation results

The solution of this minimization problem is obtained applying a convex programming algorithm, implemented with the software Matlab 2011®.

The optimal trajectories are shown in Fig. 4.3. The cost function determines the shape of the trajectory. Details are established by the boundary conditions. Given this information and the duration of the movement, the trajectory of the steering wheel is specified in its entirety. No other information is required. As expected from an optimization that minimizes the jerk, optimal trajectories are smooths and regulars. Note that the angular trajectory passes through the angle $\theta_2 = -0.58$ rad at the time $t_2 = 0.8$ s. This passage allows to obtain both the load and the driver's torques to be null at the final time. Three examples of amplification torque are proposed. They are obtained by tuning the

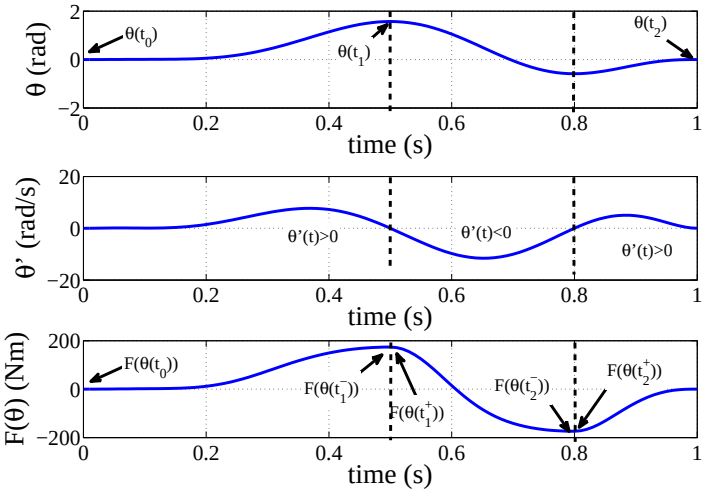


**Figure 4.3** – Evolution of the angular and speed profile used to evaluate the analytic solution of the contact friction model.

intensity magnitude $\delta$ and the rate of growth of the sensation of the stimulus $n$. For each case, two simulations are provided. They correspond, respectively, to steady-state case in Eq. (4.2.13) and to the general formulation in Eq. (4.2.15). Three values of the coefficient $n$ ($n = \{1, 0.9, 0.5\}$) are tested, while $\delta$ is tuned to provide realistic values of the booster values with $T = 15$ s.
In Fig. 4.4, coefficients are $n = 1$ and $\delta = 0.3$ ; in Fig. 4.5(a), $n = 0.9$ and $\delta = 0.3$, while in Fig. 4.5(b), $n = 0.5$ and $\delta = 1$.
The predicted profiles of the booster curves are strongly dependent from the value of $n$.

For the case in Fig. 4.4, the profile is linear in the stationary case ; the hysteresis phenomena due to the influence of the inertia and the viscosity is evident when the transient state is considered.

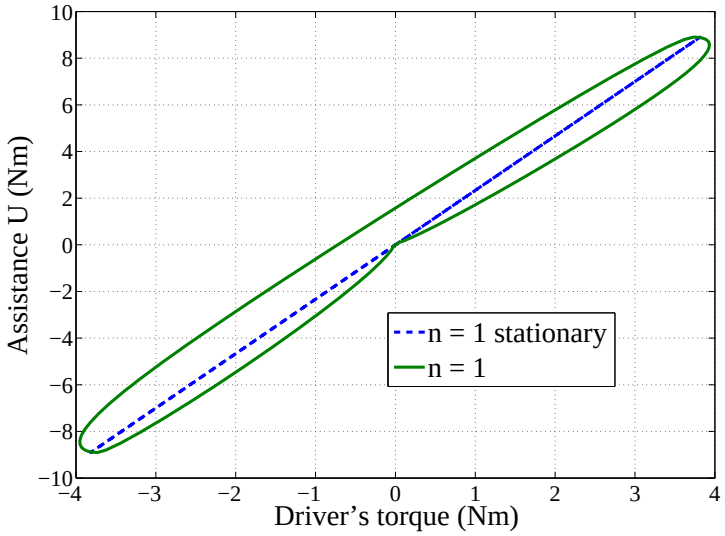


**Figure 4.4** – Amplification torque obtained to compensate the friction torque with rate of the sensation stimulus n = 1 in steady-state case (dotted) and dynamical one (full line).

For the cases $n < 1$, shown in Figs. 4.5(a) and 4.5(b), at steady-state the curve has an exponential behaviour. This characteristic is more accentuated as the coefficient $n$ diminishes (for $n = 0.5$). The amplification is almost negligible for driver's torques in the interval $-1 \leq \tau_v \leq +1$ N m, while it grows for more important values. The hysteresis effect is present when the optimization in transient state is carried out, due to the influence of the inertial and viscosity torques. Nevertheless, it is possible to conclude that the commonly used amplification curves can be linked to the optimal profile obtained based on the hypothesis of a position-oriented control of the movement.
This result justifies the choice of classical booster curves to produce the steering assistance. They not only mimic the behaviour of the hydraulic assistance, but they can be also linked to an optimal behaviour of the drivers.

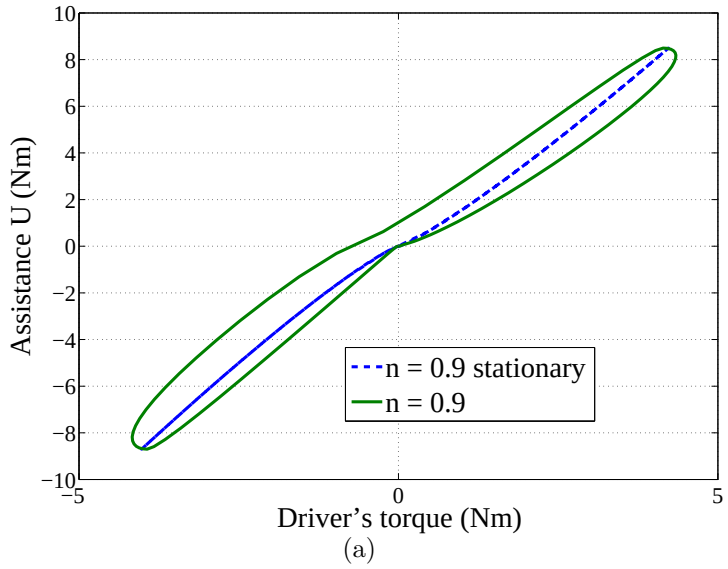


(a)

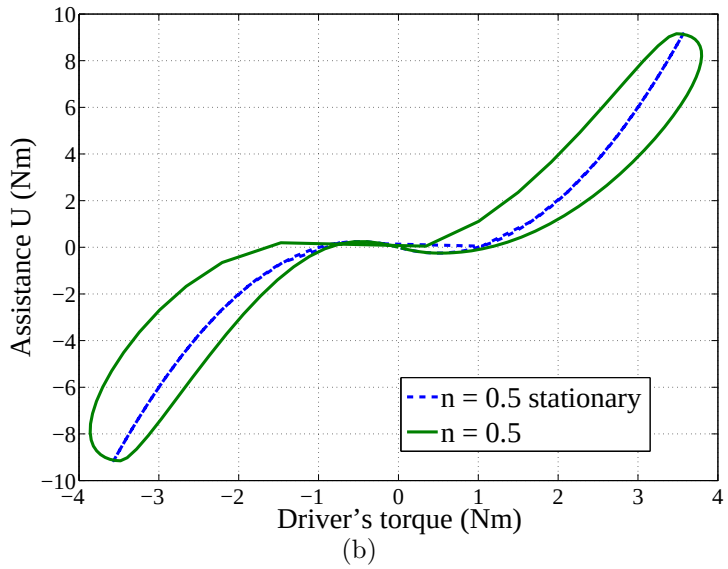


(b)

**Figure 4.5** – (a) Amplification torque obtained with rate of the sensation stimulus n = 0.9. (b) Amplification torque obtained with rate of the sensation stimulus n = 0.5.

## 4.3 Methodology to adapt EPAS to disabled drivers

The steering assistance is dedicated to drivers with reduced mobility, who may show very different symptoms according to the kind of pathology (e.g. neuro-muscular disease, absence of a limb, handicap due to a neuro-degenerative disease). In spite of the variety of different symptoms, it is possible to cluster them in common categories, such as :

– global loss of the capacity to produce a force. A close association between decline in muscle mass with reduced muscle strength with ageing has been identified, a disproportionate greater loss of muscle strength compared to muscle mass was recently

reported in a longitudinal study (about 3% versus 1% per year, respectively) ([89], [36]).
– The premature appearing of the fatigue, resulting from the disruption of the muscle due to static contraction ([34], [10]).
– Loss of precision of the movement, due to the loss of the muscular control as consequence of Parkinson's disease.
– Asymmetry : this feature is typical of drivers with only one upper limb because of the lost or the paralysis of the other one and of drivers with unilateral disease.

The goal is then to develop a methodology that may propose ad adapted steering assistance, that keep into account all these symptoms through the adding of eventual modifications to the control architecture (e.g. through the introduction of external tuning blocks) or to the shape of the standard booster curves. Road map for the proposed methodology is the following :

1. analysis of a specific symptom and of its consequences in the context of a driving task.

2. Identification of the features, that it is possible to modify on standard booster stages, in order to alleviate effects of the symptom and make the steering assistance more adapt to the specific pathology.

3. Elaboration of test scenarios and determination of evaluation criteria to validate improvements brought from the new booster stage.

4. Mathematical simulation and experimental validation of test scenarios in the context of the general architecture of the EPAS system.

Main advantages of this methodology are the generality, i.e. the possibility to apply it to every kind of symptoms and the compatibility with standard EPAS systems. Possible changes to the architecture do no affect the hardware of the system ; this aspect makes the methodology exploitable on every kind of vehicle and represents a huge advantage for the use in an industrial context.

The real study case that has been chosen in this thesis concerns drivers affected by muscular diseases, that causes a certain degree of asymmetry into the upper limb w.r.t. the steering wheel. In a more general context, asymmetry may affect also drivers who can drive with both hands, but they cannot exert the same torque on both sides, because an upper limb is stronger than the other one. These drivers may be affected by unilateral diseases (e.g. paralysis to one of two upper limbs) and they drive with the use of a ball, a fork or a tripod.

### 4.3.1 Application of the methodology for asymmetric drivers

#### 4.3.1.1 Gravitational asymmetry

After this general analysis, the second step of the methodology consists into the mathematical modelling of the asymmetry. From a bio-mechanical point of view, a healthy driver represents a closed chain with the steering wheel. Forces exerted by each upper limb can be symmetrical to turn the steering wheel.

In case of driver with only one upper limb, the driver performs an open chain with the steering wheel. He has no choice, because he always uses the same arm so the driver will get tired more quickly. Moreover, he faces to a reduced stability and control of the vehicle and a bigger effort to apply with the healthy arm.

Let us consider a driver with only one upper limb on the steering wheel. It is possible to consider that the torque exerted with this limb acts as a gravity torque, due to the weight of the limb, and that is not compensated by the presence of the other limb. This weight depends from the position $\theta_v$ and others constant terms, that project the weight force on the plane of the steering wheel.

To model this torque, let us consider the reference axis system on the plane of the steering wheel $(O, \overrightarrow{x_v}, \overrightarrow{y_v}, \overrightarrow{z_v})$ as shown in Fig. 4.6(a), with the out-going $\overrightarrow{z_v}$ axis. On this plane, the gravity torque is given from the following vector product

$$\overrightarrow{\tau_g} = \overrightarrow{OR} \wedge \overrightarrow{F}_g \tag{4.3.1}$$

where $\overrightarrow{OR}$ is moment arm and $\overrightarrow{F}_g$ is the reaction force due to the weight of the upper limb. On the plane $(O, \overrightarrow{x}_v, \overrightarrow{y}_v, \overrightarrow{z}_v)$, $\overrightarrow{OR}$ is given from the sum of following components

$$\begin{aligned} \overrightarrow{OR} &= OR_x \overrightarrow{x}_v + OR_y \overrightarrow{y}_v & (4.3.2) \\ &= r_{sw} \cos\theta_v \overrightarrow{x}_v + r_{sw} \sin\theta_v \overrightarrow{y}_v & (4.3.3) \end{aligned}$$

with $r_{sw}$ the radius of the steering wheel.
On commercial vehicles, the steering wheel is inclined with respect to the vertical axis of the suspension, measured in the longitudinal direction, and the inclination angle is known as caster angle $\Phi$. This implies that the gravity force must be projected on the reference axis $(O, \overrightarrow{x}_v, \overrightarrow{y}_v, \overrightarrow{z}_v)$, as shown in Fig. 4.6(b).
Resulting force $\overrightarrow{F}_g$ has components only across the $\overrightarrow{y}_v$ and the $\overrightarrow{z}_v$ axis

$$\overrightarrow{F}_g = -F_g \sin\Phi \overrightarrow{y}_v - F_g \cos\Phi \overrightarrow{z}_y \quad . \tag{4.3.4}$$

Force $\overrightarrow{F}_g$ is a function of the mass $m$ and of the posture of the upper limb. Value of the mass $m$ is proper to each driver and it is necessary to estimate it. To this aim, two methods are proposed : the first one is an off-line method, based on a bio-mechanical

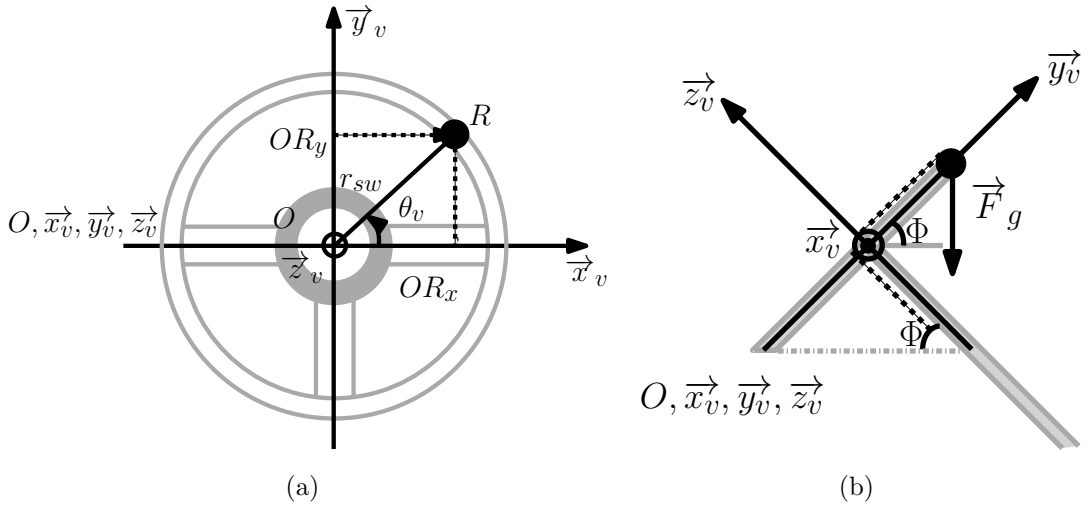


**Figure 4.6** – References used to describe the weight disturb on the driver's model. (a) Projections of the radius on the steering wheel plane. (b) Projections of the weight force on the steering wheel plane.

model of the driver's upper limb and on values shown on anthropometric tables [90]. The second one is on-line and will be introduced in Chapter 5.

To introduce the biomechanical model of the upper limb, let us make the following assumptions :
– the upper limb is rigid and extended ;
– the hand leans at the center of the steering wheel. This correspond to an average position.

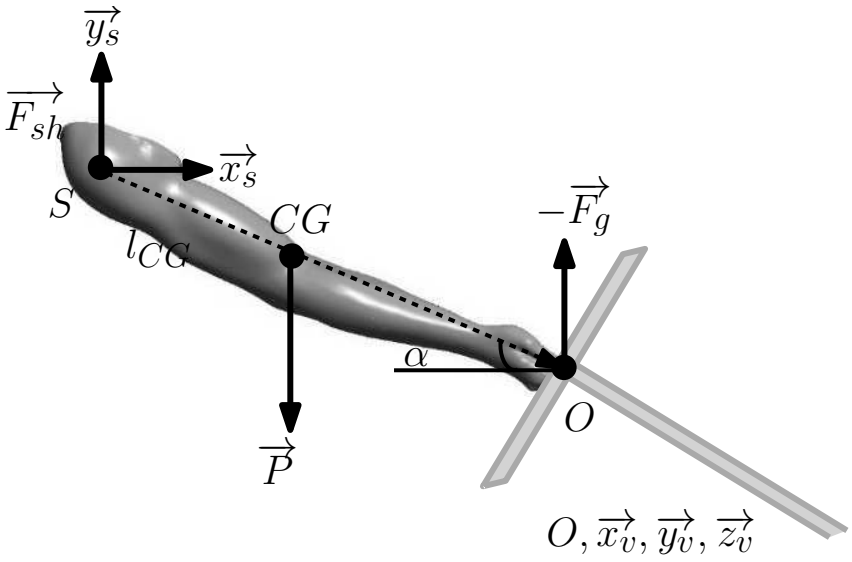


**Figure 4.7** – Balance of forces around the rigid arm

Isolating the upper limb, as shown in Fig. 4.7, static principle of equilibrium of forces

leads to

$$\sum \overrightarrow{F}_{ext} = 0 \Longrightarrow \overrightarrow{F}_{sh} + \overrightarrow{P} - \overrightarrow{F}_{g} = \overrightarrow{0} \tag{4.3.5}$$

and for moments leads to

$$\sum \overrightarrow{M}_s(\overrightarrow{F}_{ext}) = \overrightarrow{0} \Longrightarrow \overrightarrow{M}_s(\overrightarrow{P}) + \overrightarrow{M}_s(-\overrightarrow{F}) = \overrightarrow{0} \tag{4.3.6}$$

where

$$\overrightarrow{M}_s(\overrightarrow{P}) = -mg \times l_{CG} \cos\alpha \, \overrightarrow{z}_s \tag{4.3.7}$$

$$\overrightarrow{M}_s(-\overrightarrow{F}) = F_g \times l \cos\alpha \, \overrightarrow{z}_s \tag{4.3.8}$$

$$\tag{4.3.9}$$

These equations lead to

$$F_g = \frac{g\, m\, l_{CG}}{l} = g \times \hat{m} \tag{4.3.10}$$

where $\hat{m}$ is a mass parameter that allows to quantify the reaction force of the upper limb on the steering wheel and is defined as function of the length $l_{CG}$ of the upper limb at the Center of Gravity (CoG) and the total length of the upper limb $l$

$$\hat{m} = \frac{m\, l_{CG}}{l} \quad . \tag{4.3.11}$$

Anthropometric tables in [90] define the length $l_{CG}$ as a percentage w.r.t. $l$

$$l_{CG} = 47\,\%l \quad .$$

The same tables provide a relationship between the mass $m$ at the CoG w.r.t. the total mass of the person $M_{tot}$

$$m = 5\,\%M_{tot} \quad .$$

This implies that the reaction force is given by

$$F_g = g\, 0.05\, M_{tot} \times 0.47 \tag{4.3.12}$$

so the mass parameter corresponds to

$$\hat{m} = 0.05\, M_{tot} \times 0.47 \tag{4.3.13}$$

For a person of $M_{tot} = 76$ kg, the weight of the upper limb is $\hat{m} = 1.786$ kg.
This method is simple, but it requires informations, that can be obtained only through anthropometric tables. To overcome this limitation, an experimental estimation is proposed in Chapter 5 and results are compared each other.

Resulting gravity torque $\tau_g$ is given from the vector product between the moment arm $\overrightarrow{OR}$ and the force $\overrightarrow{F}_g$ :

$$\overrightarrow{\tau_g} \;=\; \overrightarrow{OR} \wedge \overrightarrow{F}_g =$$

$$
\begin{aligned}
&= [r_{sw}\cos\theta_v \overrightarrow{x}_v + r_{sw}\sin\theta_v \overrightarrow{y}_v] \wedge [-F_g \sin\Phi \overrightarrow{y}_v - F_g \cos\Phi \overrightarrow{z}_y] \\
&= (-r_{sw}F_g \sin\Phi\cos\theta_v)\overrightarrow{z}_v - (r_{sw}F_g \cos\Phi\cos\theta_v)\overrightarrow{y}_v + \\
&- (r_{sw}F_g \cos\Phi\sin\theta_v)\overrightarrow{x}_v \qquad (4.3.14)
\end{aligned}
$$

Component $\tau_{gx}$ contributes to pull the steering wheel across the $\overrightarrow{x_v}$ axis, while component $\tau_{gy}$ acts across the $\overrightarrow{y_v}$. The only component that contribute to turn the steering wheel is around the $\overrightarrow{z_v}$ axis

$$\tau_{gz} = (-r_{sw}F_g \sin\Phi\cos\theta_v)\overrightarrow{z_v} \quad . \qquad (4.3.15)$$

#### 4.3.1.2 Muscular asymmetry

Until now, we considered the case of a driver with only one upper limb. However, we observed that, even in case of an healthy driver, the maximum torque, that can be exerted on the steering wheel is not the same in all quadrants on the steering wheel. This means that there is also a muscular asymmetry into the torque production on the steering wheel.

To this aim, we have performed some experimental tests, although with a restricted number of subjects. Such tests give very encouraging results, but this study could be enriched and could have a validation with a larger test campaign.
In our tests we have considered measures of driver's exerted torque obtained with 3 subjects using the experimental setup that will be shown in detail in Chapter 5.
For each driver, 3 experiments are trained out with the steering wheel locked in 8 reference positions, as it is shown in Fig. 4.8.

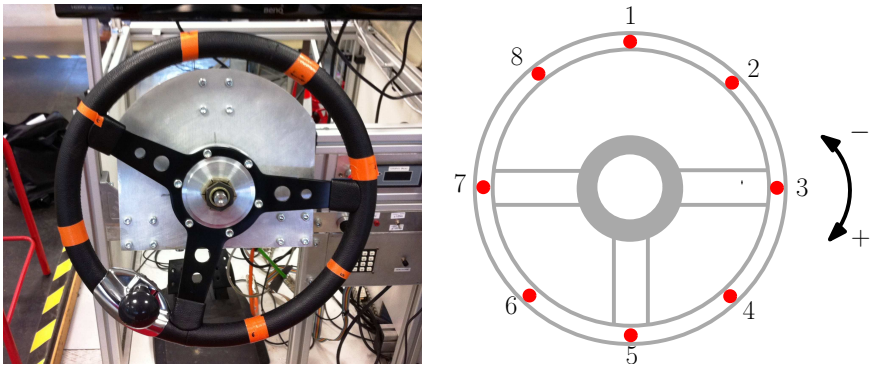


(a) (b)

**Figure 4.8** – (a) Real steering wheel used for the experiment. (b) Scheme of the steering wheel with the 8 positions used to make the experiment.

During all the tests, the steering wheel is locked and we ask the driver to exert a maximum effort to rotate the steering wheel.

During the first experiment, the driver is forced to push with both upper limbs with his/her hands at ±45 ° w.r.t. the referenced position on the steering wheel. This test is repeated twice : the first time the driver exerts a torque in clockwise, the second time the driver exerts a torque in anti clockwise. In total, 16 measures for each driver are collected. These measures are normalized w.r.t. the maximum value.
Results of this test are shown in Fig. 4.9, where it is possible to remark that profiles of each driver are similar and reproducible. This proves that the profile of forces is repeatable among different subjects, even if they have not a statistical value.

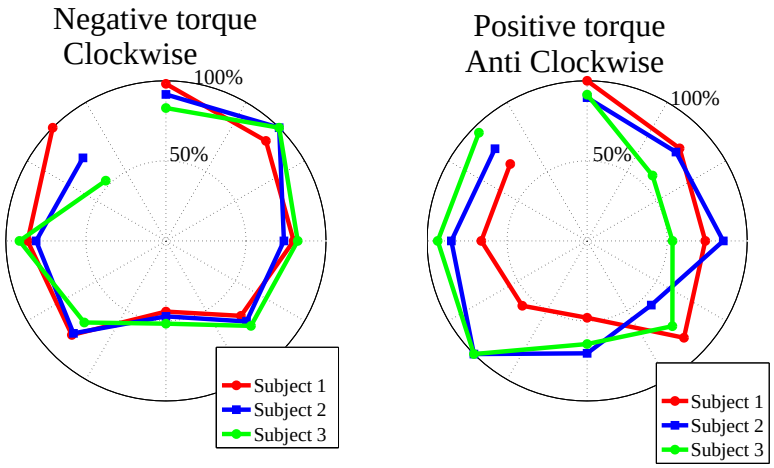


**Figure 4.9** – Measures of maximum torque done with 2 hands with the steering wheel locked. On the left, the operator applies the torque in clockwise. On the right, the torque is applied in anti-clockwise. Each measure is normalised w.r.t. the maximum, in order to provide a percentage of the exerted torque.

In the second experiment, a ball is mounted in correspondence of each reference position, shown in Fig. 4.8, and the driver is forced to push with the left hand. The first set of measure is done with the torque exerted in clockwise (positive driver's torque +), while during the second set of measure the torque is exerted in anti clockwise (negative driver's torque −). Each measure is normalised w.r.t. the maximum of each subject. Results of these tests are shown in Fig. 4.10.

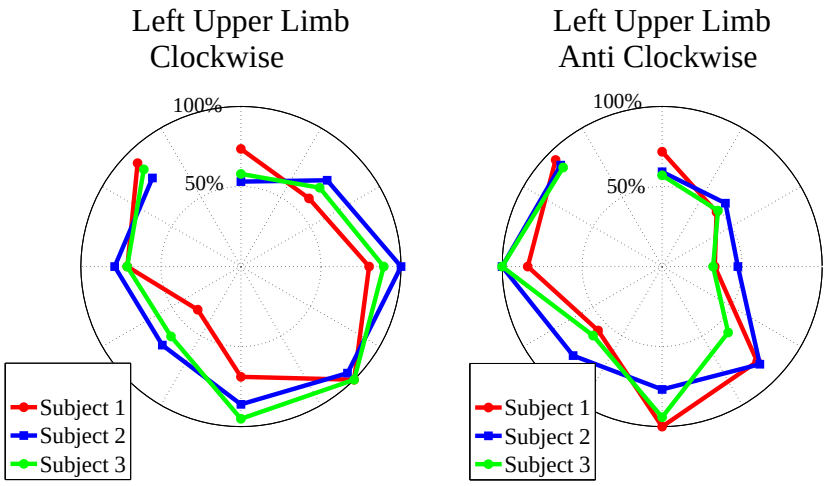


**Figure 4.10** – Measures of maximum torque done with 1 hand with the steering wheel locked. The left harm is on the steering wheel and applies a torque in clockwise (left) and anti-clockwise (right). Torques are divided w.r.t. the maximum torque.

In the third experiment, a ball is mounted in correspondence of each position and the driver is forced to push with the right hand, first in clockwise and then in anti clockwise. Results of this test are shown in Fig. 4.11.

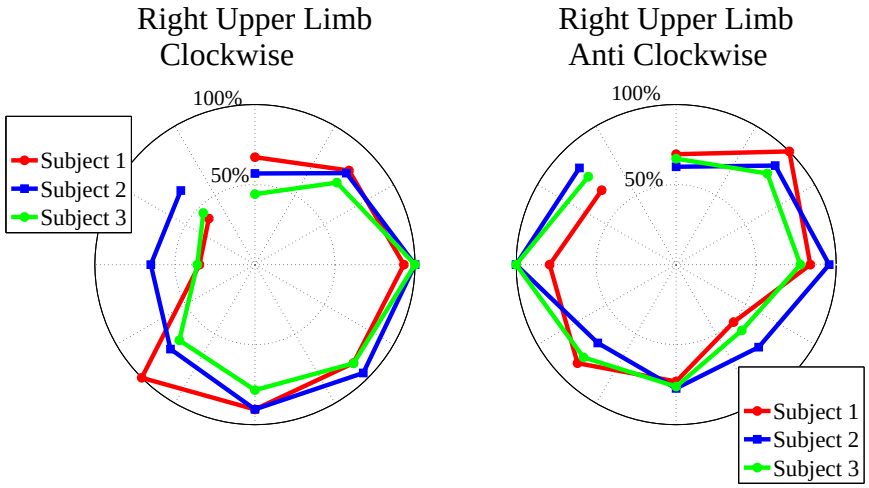


**Figure 4.11** – Measures of maximum torque done with 1 hand with the steering wheel locked. The left harm is on the steering wheel and applies a torque in clockwise (left) and anti-clockwise (right). Torques are divided w.r.t. the maximum torque.

More in detail in Fig. 4.10, the left upper limb in anti clockwise shows that subjects are stronger on the left side front to the steering wheel than on the right side. In Fig. 4.11, the right upper limb in clockwise shows that subjects are stronger on the right side front to the steering wheel than on the left side. Moreover, the profile of the left upper

limb in clockwise is symmetric to the anti clockwise profile of the right upper limb. Maximum values correspond to the situation when the operator pushes (or pulls) at his/her maximum effort. The hollow part in front of the peak corresponds to the situation when the operator has to do a lateral effort.

Now let us consider the averages on the real measured torque (not normalized). Let us calculate the average value in absolute value of torques exerted with the both the upper limbs from all the subjects. The obtained value is 5.01 N m.
The average value of the exerted torques with the left upper limb is 2.34 N m, while the average value with the right upper limb is 2.21 N m.
These results imply that exerted torque with one arm is approximately the half of the exerted torque with both upper limbs, meaning the existence of the muscular asymmetry.

It is also possible to calculate an asymmetry ratio $A_r$ for all the subjects, defined as

$$A_r = \frac{\max(\tau_v) - \min(\tau_v)}{\max(\tau_v)} \quad [\%] \tag{4.3.16}$$

In the case of driving with both the upper limbs, average ratio for all the subjects is 53.58% in both rotational sense. In case of driving with only the left upper limb, average ratio is 63.32%, while for the right hand is 58.5%, meaning that subjects have more difficulty to exert the same maximum torque all over the plane of the steering wheel with only one hand.

The asymmetric behaviour into the torque exertion is a good starting point to apply the proposed methodology. At this aim, next paragraph will be dedicated to the introduction of the adaptation of the EPAS system.

### 4.3.2 Adaptation of the EPAS system

Following step of the methodology consists in the identification of critical situations where the disease may appear and affect the driving behaviour. This step represents the starting point to modify the standard booster curves.

Let us consider the case of a driving at low speeds. As stated before, an asymmetric driver uses always the same upper limb to turn the steering wheel. The muscular control torque $\tau_m(t)$ is an active load, that acts according to the direction of the movement. The gravity torque $\tau_{gz}(t)$ is passive and acts always in the same direction. According to the direction of the movement, $\tau_{gz}(t)$ may accelerate or brake the control torque. When it acts as a brake, it increases driver's fatigue and strain, while it can be helpful to improve driver's torque when it acts in the opposite way. Let us describe following situations :

1. At low speeds, the corresponding steering assistance law has to keep into account this dual behaviour. For this reason, it can be modified to compensate this bias torque when it brakes the movement, but it does not act when it can help it.

2. At high speeds, two aspects can be revealed :
   - the first one is the fatigue due to the effect to maintain the same straight position with only one upper limb for a long time. For instance, let us consider the case of a long time driving on an highway, an asymmetric driver has to keep the arm suspended for a long period without the opposite arm to counterbalance. This situation brings to the arrival of muscular weakness, rigidity, fatigue, muscular pain and driving may become uncomfortable.
   - The second aspect concerns the problem of control during during an emergency manoeuvre. Let us consider a classical manoeuvre of obstacle avoidance. Gravity torque may interfere with the muscular control and may bring to instabilities into the accomplishing of the task.

   In both situations at high speeds, the steering assistance assumes the role of compensating torque, but it has two different objectives : to improve driver's comfort and to improve driving control.

The compensation among asymmetric drivers can be done through the introduction of an additional torque, that modifies the standard booster curves according to the cruise speed of the vehicle and driver's needs in that moment.
To join these requirements with the diffused technology the following extension to the dynamic assistance model of Eqs. (1.2.2) and (1.2.3) is proposed :

$$\dot{\xi} = \begin{cases} -a\xi - b\sqrt{|\xi|}\dot{\theta}_v + c(\sqrt{|\xi| + \varepsilon})\tau_m, & \text{if } |\xi| \leq \xi_{max} \\ 0, & \text{else} \end{cases} \tag{4.3.17}$$

with the assistance torque $\tau_{ass}$

$$\tau_{ass} = (h_1(v) \times \xi) - \tau_{gz} \times \left[(1 - h_1(v)) + \frac{h_1(v)}{2}\left(1 - \text{sign}(\tau_m \times \tau_{gz})\right)\right] \tag{4.3.18}$$

The linear function $h_1(v)$ determines the transitions between the assistance provided at high speeds and the assistance at lows speeds of the vehicle $v$. This function is defined as follows :

$$h_1(v) = \begin{cases} 1, & \text{for } v = 0\,\text{km/h}; \\ 0, & \text{for } v = 30\,\text{km/h}. \end{cases} \tag{4.3.19}$$

The output of the previous differential equation saturates, as soon as $\xi$ reaches the maximum $\xi_{max}$, admitted from the electrical motor.

The steering assistance requires measures of the control torque $\tau_m$, of the bias $\tau_{gz}$ and of the angular velocity of the steering wheel $\dot{\theta}_v$. These measures can be obtained starting from the observer, developed in Chapter 3.
The gravity torque is completely known thanks to the estimation of the mass parameter $\hat{m}$ of the upper limb and the knowledge of the estimated position of the steering wheel

$\hat{\theta}_v$. Moreover, the observer provides an estimates of the total driver's torque $\hat{\tau}_v$. These measures can be substituted in Eq. (4.3.27) and allow us to identify the contribution of the estimated control input $\hat{\tau}_m$, as follows

$$\hat{\tau}_m = \hat{\tau}_v(t) - \hat{\tau}_m gR \cos\Phi \cos\hat{\theta}_v(t) \quad , \tag{4.3.20}$$

that can be given in input to the assistance stage. Note that on the real setup, this element represents the muscular contribution of the driver's torque on the steering wheel.

Let us consider how the proposed steering assistance modifies the shape of the standard booster curves. For simplicity of the representation, we show the map of the assistance provided by the model at steady-state ($\dot{\xi} = \dot{\theta}_v = 0$) for the most representative cruise speeds of the vehicle ($v = 0$ and $30\ \mathrm{km\,h^{-1}}$). These graphs are shown in Figs. 4.12 and 4.13, for a range of values of the driver's torque between $\pm 5$ N m all over the steering plane. The gravity torque is positive for all $\theta_v > 0$, while it is negative when $\theta_v < 0$.

Let us consider the cruise speed of the vehicle $v = 0\ \mathrm{km\,h^{-1}}$ : the compensation acts and modifies the contribution of the classical assistance when the control torque $\tau_m > 0$ and we are in the negative plane of the disturbance. Otherwise, it is not active (see Fig. 4.12). The assistance exploits the contribution of the gravity torque, when it is in the same direction of the movement, otherwise compensates it.

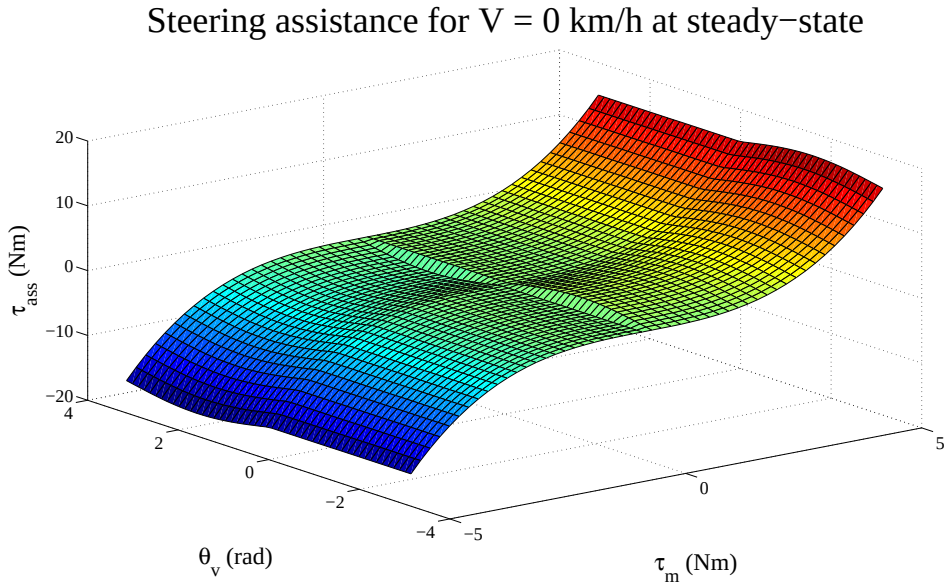


**Figure 4.12** – Map of the proposed steering assistance at steady-state for a cruise speed of the vehicle $v = 0\ \mathrm{km\,h^{-1}}$. The assistance acts only on the part of the plane when the gravity torque opposes to the movement.

When the cruise speed is at $v = 30\ \mathrm{km\,h^{-1}}$, the compensation is always active, modifying everywhere the classical assistance (see Fig. 4.13). In this case, its role is to counterbalance the asymmetry to improve driver's strain and driving precision at the time.

In transient, these maps keep the same profile, but in addition it is possible to see the hysteresis area that it has been introduced with the dynamic standard booster stages.

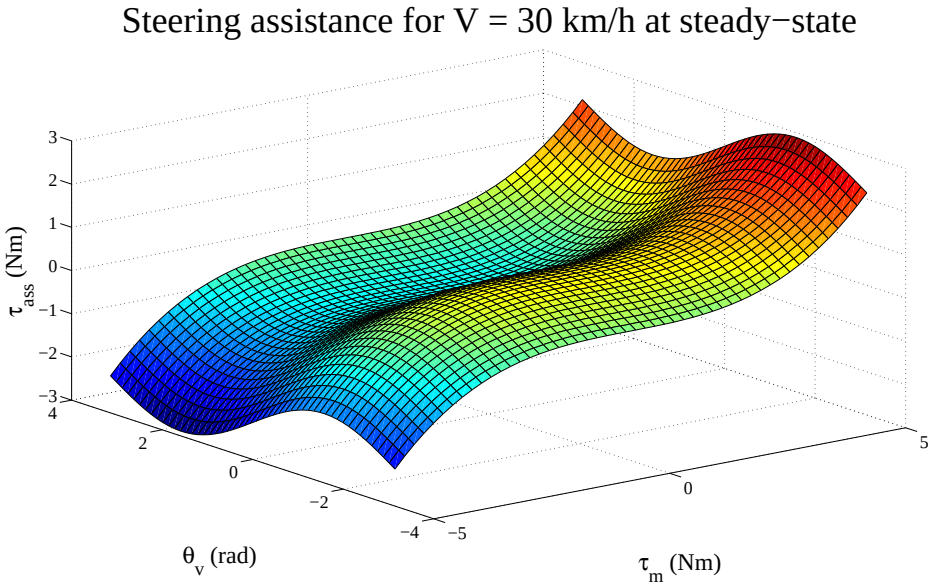


**Figure 4.13** – Map of the proposed steering assistance at steady-state for a cruise speed of the vehicle $v = 30\ \mathrm{km\,h^{-1}}$. The assistance always acts to compensate the gravity torque.

### 4.3.3 Elaboration of test scenarios and determination of evaluation criteria

The next step consists of verifying if the proposed steering assistance achieves its design goals. This can be ensured by the introduction of the assistance in the general control architecture of the EPAS system and by the simulation of this combined system for some test scenarios of interest. In the current case of study, three test scenarios are considered :

1. a parking manoeuvre at slow motion ;
2. a cruise control situation at low speeds, where the driver keeps the same position over a long period ;
3. an obstacle avoidance at low speeds.

The analysis of effects of the EPAS system is strictly dependent from driver's steering feel, which cannot be easily evaluated. For this reason, we developed different criteria with quantitative mechanical features.

First index used to validate the assistance into the improvement of the driver's strain quantifies the driver's energy $E_d(t)$ during the driving task. It is considered into absolute value, because driver's muscles are not reversible. The definition of this index is the

following :

$$E_d(t) = \int_0^T |\tau_m(t) \times \dot{\theta}_v(t)| \mathrm{d}t \tag{4.3.21}$$

where $\tau_m(t)$ can be obtained from the torque observer described in Chapter 3 and through Eq. (4.3.20).

This criterion allows to quantify energy expenditure during a driving task. However, benefits of EPAS system can be evaluated also in terms of muscular activity level. Many agonist and antagonist muscles are activated during a driving task, at the shoulder, elbow and wrist joints.
Quantifying each muscular activity needs sophisticated biomechanical models or additive Electromyography (EMG) measurements. A reduced representation of global muscular activity is the driver's torque exerted on the steering wheel. This leads to the criterion, representing the global muscular activity exerted during a driving task. This criterion is the driver's strength $S_d(t)$, defined as follows :

$$S_d(t) = \int_0^T |\tau_m(t)|^2 \mathrm{d}t \quad , \tag{4.3.22}$$

Another aspect of the benefits brought from the EPAS system is the driving precision $D_p(t)$, that can be defined as the error between the reference trajectory and the current value of the steering wheel angle

$$D_p(t) = \int_0^T (\theta_{ref}(t) - \theta_v(t))^2 dt \tag{4.3.23}$$

and the objective of the assistance is to minimize this error.

For each study case, the corresponding evaluation criteria is shown in Table 4.1.

| Scenario | Vehicle speed | Ball position | Metrics |
|---|---|---|---|
| Parking manoeuvre | 0 km/h | 0° / 90° | Driver's energy $E_d$ |
| Cruise control | 30 km/h | 0° / 60° | Driver's strength $S_d$ |
| Obstacle avoidance | 30 km/h | 0° / 60° | Driving precision $D_p$ |

**Table 4.1** – Summarizing table with simulation/test scenarios and corresponding improvement critera

To simulate the proposed adaptation methodology, it is necessary to have a mathematical model of the driver that acts on the system, under the influence of the gravity torque.
To this aim, in control system domain, two approaches are the most employed to model driver's behaviour. The first one is based on the assumption that the driver behaves as a compensation tracking control, that takes into account the error between the actual driving state information and the expected one ([39], [3], [77]). The second one assume

the driver as a preview tracking model, that use future road information ([52], [74], [26], [68], [55]).

In this thesis, the proposed controller derives from ([39], [3], [77]), where authors use driver's models to estimate the stability of the closed-loop system with perturbation. They models the driver as a Proportional Integral Derivative (PID) controller. In this thesis, to keep into account driver's physical limitations, this control is enriched with a time delay and an output saturation. Time delays are added to model neuromuscular delays to actuate the control input [55]. Saturations are added to simulate the effect that the driver's exerted torque is limited by the strength of his muscles and the arising of the muscular fatigue [46].

To describe the proposed control strategy, let us introduce the tracking error $e(t)$, as the difference between the reference trajectory $\theta_{ref}(t)$ and the steering wheel position $\theta_v(t)$ :

$$e(t) = \theta_{ref}(t) - \theta_v(t) \tag{4.3.24}$$

Output of the controller is multiplied by the physical action time delay $\delta$

$$\tau_c(t) = K_p \left( e(t-\delta) + \frac{1}{T_i} \int_0^t e(t-\delta)\mathrm{d}t + T_d \frac{\mathrm{d}e(t-T_r)}{\mathrm{d}t} \right) \tag{4.3.25}$$

where the constant $K_p$ is the coefficient of the proportional action ; $T_d$ and $T_i$ are, respectively, the time constants of the derivative and integral actions (reset time), measured in seconds.
The first term is proportional to the tracking error ; the second one is proportional to the integral of the error and it is useful to impose the cancellation of the error at steady-state face to constant references or disturbances. Finally, third term is proportional to the derivative of the error and has the goal to anticipate the evolution of the error in future time. For instance, if the derivative of the error is positive, the control action is augmented thanks to the derivative action to obtain a bigger value for the trajectory of the system and, consequently, the decrease of the tracking error.

Previous controller is saturated between a maximum and a minimum value, so the complete expression for the driver's exerted torque is

$$\tau_m(t) = \max(\min(\tau_c(t), \tau_{\max}), \tau_{\min}) \tag{4.3.26}$$

where $\tau_{max}$ and $\tau_{min}$ correspond to the upper and lower saturation limits, that the muscular capacity may reach.

Values assumed from constants $K_p$, $T_d$ and $T_i$ derive from the literature [44], while adopted values for $\tau_{max}$ and $\tau_{min}$ are chosen to obtain realistic values of driver's torque. All numerical values are shown in Appendix A.2.

The complete expression of the driver's exerted torque under the influence of the gravity torque is

$$\tau_v(t) \quad = \quad \tau_m(t) + \tau_{gz}(t) = \tag{4.3.27}$$

$$= \max(\min(\tau_c(t), \tau_{\max}), \tau_{\min}) + r_{sw} F_g \sin\Phi \cos\theta_v \quad .$$

Each scenario is simulated in 3 different driving conditions, in order to verify the effects of the proposed assistance. The first test corresponds to the ideal case of a standard driver. The tracking controller takes in input the error between the reference trajectory and the current path and exerts the corresponding delayed torque on the steering wheel, without the influence of the steering assistance :

$$\tau_v(t) = \tau_m(t) \quad .$$

The second simulation corresponds to the case of a driver with reduced mobility, which is not assisted :

$$\tau_v(t) = \tau_m(t) + \tau_{gz}(t) \quad ,$$

The gravity torque acts on the controller, but there is the assistance to compensate it.

Finally, last simulation corresponds to the case of a driver with reduced mobility, which is assisted by the proposed steering assistance

$$\tau_v(t) = \tau_m(t) + \tau_{gz}(t) + \tau_{ass} \quad .$$

All these simulations are done with the EPS system in closed loop, i.e. the controller for the oscillations of the steering column is activated and the torque observer is also active. The tyre-road feedback is provided from the simulated models of sticking and self-alignment torque, developed in Chapter 2.

For each scenario the most significant case is shown with the initial position of the steering wheel at $\theta_0 = 0$ ° or $\theta_0 = 60$ °. It is always possible to retrieve the other simulation by translation of the curves.

#### 4.3.3.1 Simulation of a parking manoeuvre

To simulate a parking manoeuvre at low speeds, a ramp signal is given as reference trajectory in input to the tracking controller. The speed of the vehicle is set at 0 $\mathrm{km\,h^{-1}}$. Under these conditions, the main responsible of the road feeling feedback is the sticking torque, that reaches values up to 30 N m.

Let us consider the case with the position of the ball on steering wheel is at $\theta_0 = 0$ °. The corresponding movement let the driver move his upper limb from $\theta_v = 0$ ° to $\theta_v = 90$ °.

In Fig. 4.14 the reference trajectory is compared with the resulting trajectory at the output of each driver's model. It is evident the influence of the disturbance on the second model, when he tries to gain the straight position (at 25 s), while this disturbance is compensated by the steering assistance acting on the third model.

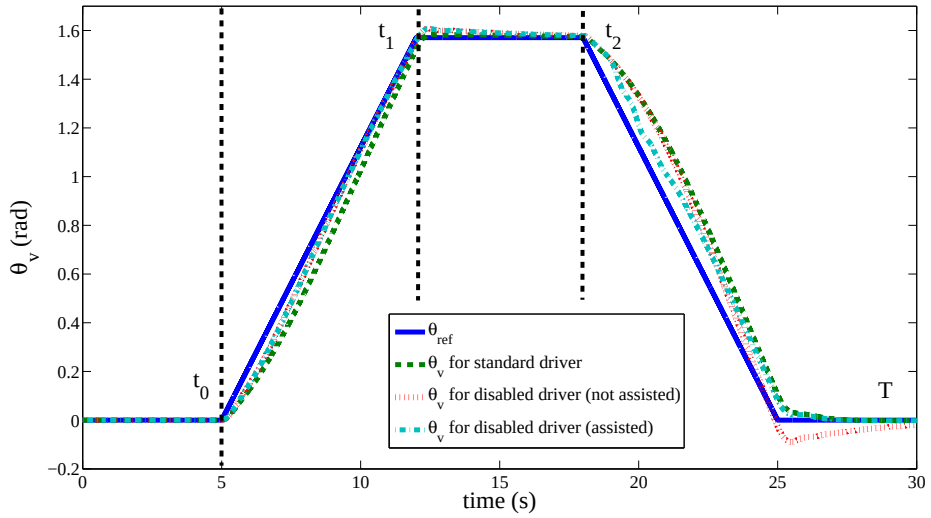


**Figure 4.14** – Profile of the trajectory of the steering wheel used to simulate parking manoeuvre. Between time instants $t_0$ and $t_1$ the movement is in the same direction of the bias, while between $t_2$ and $T$ the movement is in opposite direction.

In this scenario, it is possible to observe how the assistance helps to reduce the driver's strain (see Fig. 4.15) : for $t \in (t_0 : t_1)$, the assistance is not active, because the weight helps the driver's movement, so the curve of driver's strain overlaps the curve corresponding to the second model, without assistance. For $t \in (t_2 : T)$, the compensation is active and the curve of strain overlaps that one corresponding to the first model, with a global improvement of the driving comfort.

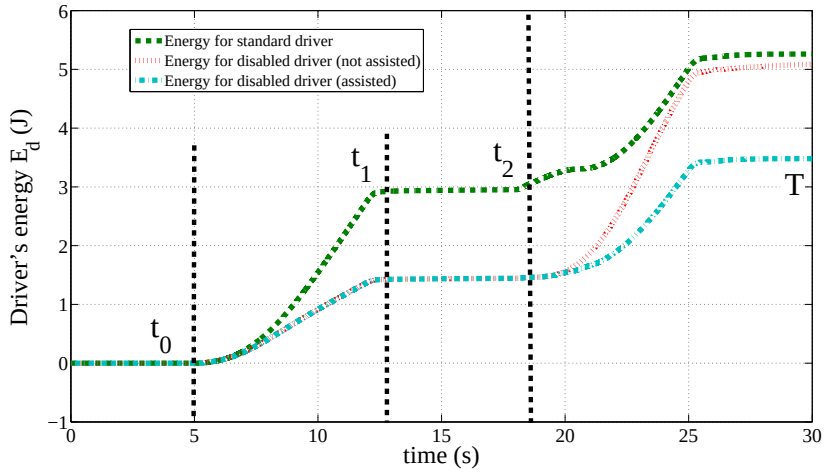


**Figure 4.15** – Profile of the driver's energy during the simulation. Steering assistance acts directly for $t \in (t_2 : T)$, allowing the driver to save energy.

As additional index of the performances of the steering assistance during a parking manoeuvre, it is possible to look at the driver's power consumption over the steering wheel plane. This is shown in Fig. 4.16, where the power consumption is shown during

2 parts of the movement : from 0 ° to 90 ° the movement is in the same direction as the bias, so the assistance does not compensate. When the movement is in the opposite sense, the assistance helps to diminish the driver's power consumption.

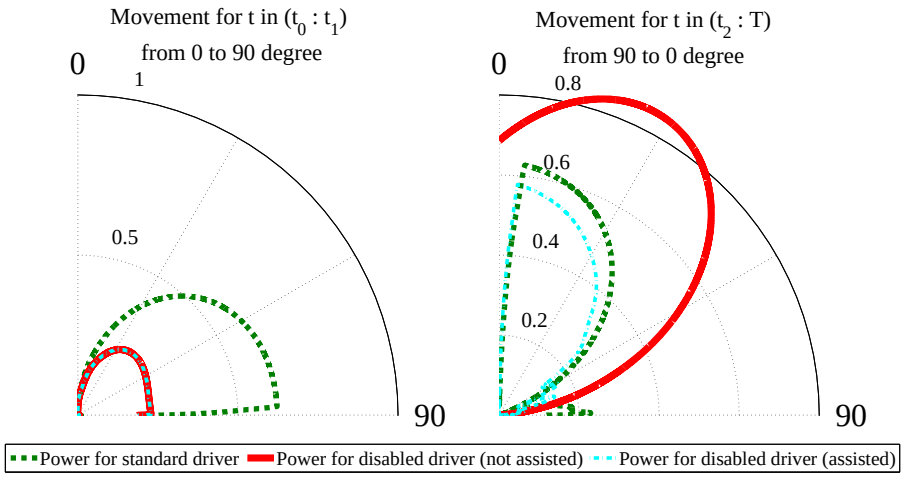


**Figure 4.16** – Driver's power during the simulation of a parking manoeuvre. The steering assistance does not act during the first phase of the movement when the bias acts in the same direction of the movement, while it acts during the second part allowing the driver to spend less power.

#### 4.3.3.2 Simulation of a cruise control

The effect to maintain the same straight position for a long time influences driver's strain and fatigue. In this case, the proposed steering assistance acts to compensate the asymmetry, due to the disease. In this way, it helps to maintain the path following at high speeds and to improve the driving comfort.
This is a trivial results, that can be shown in the last part of the movement in Fig. 4.17 at the time instant for $t > 25$ s. The assistance helps to maintain the trajectory on the fixed reference.

#### 4.3.3.3 Simulation of an obstacle avoidance

To simulate the scenario of an obstacle avoidance, a step-wise reference trajectory is given in input to the tracking control. The vehicle is simulated with a cruise speed of 30 $\mathrm{km\,h^{-1}}$. At these speeds of the vehicle, the main responsible of the road feedback is the self-alignment torque.

Let us consider the case with the position of the ball on steering wheel is at $\theta_0 = 0$ °. The corresponding movement let the driver move his upper limb from $\theta_v = 0$ ° to $\theta_v = 90$ °.

The driver's steering assistance is always active to compensate the disturbance and to improve the driving precision.

Simulation results are shown in Fig. 4.17 with the 3 different driver's models. The influence of the disturb on the tracking control is clear, when it tries to change the path direction every 5 second. The assistance brings the trajectory of the steering wheel on the same path as if the driver could drive without the disease.

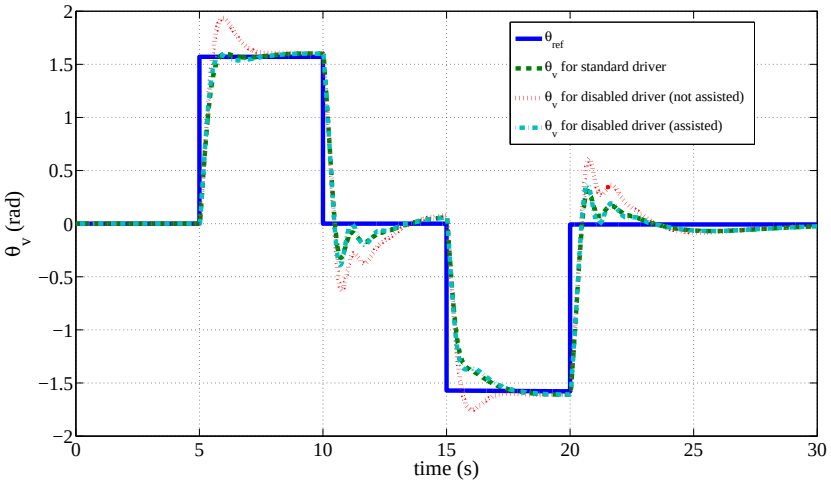


**Figure 4.17** – Profile of the trajectory of the steering wheel used to simulate obstacle avoidance.

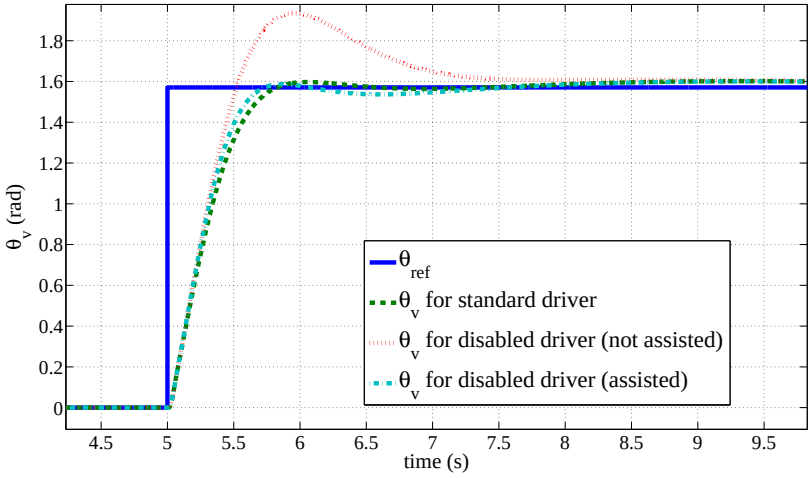


**Figure 4.18** – Zoom on the part of the simulation at 5 second, when the steering assistance acts to improve control during the manoeuvre of the obstacle avoidance.

Bar graph reporting the driving precisions for all cases is shown in Fig. 4.19. It is possible to remark the improvements due to the introduction of the steering assistance on the

driver 3. In this case, the value assumed by the error between the current path and the reference trajectory is the lower than the case without the steering assistance.

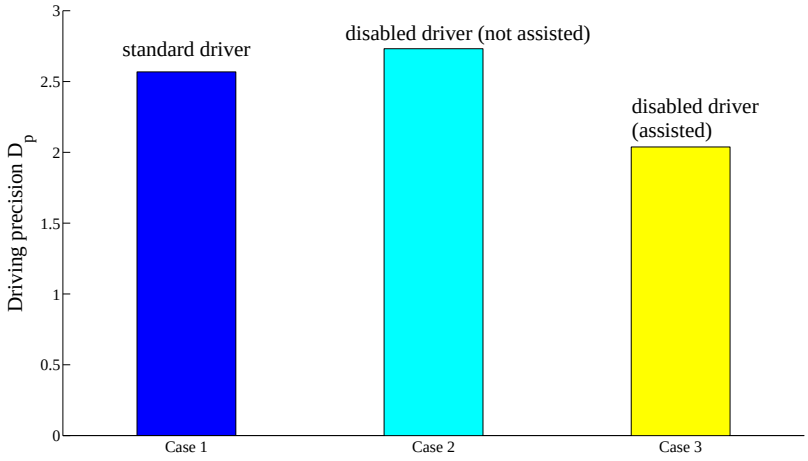


**Figure 4.19** – Bar graph with the driving precisions, calculated in all cases of interest. Improvements due to the steering assistance are shown in case 3, where the error between the trajectory of the steering wheel and the reference is minimized.

## 4.4 Concluding remarks

Purposes of this chapter were manifold. First, a study to provide some rationality the existing criteria used in EPAS systems is done. The analysis was carried out in steady-state and transient conditions to provide a mathematical relation between the provided assistance and the driver's exerted torque. In steady-state, a relation in closed form between the assistance torque and the driver's torque was founded. For the transient case, an optimization procedure is applied to reproduce the shape of the booster curves. The study showed that the profile of the booster curve can be linked to minimization criteria based on the steering wheel jerk, coupled with the Stevens' power law. Moreover, the analysis showed that the profile of the predicted booster curves is strictly influenced by the rate of growth of the sensation of the stimulus, coming from the contact friction torque, but the commonly used booster curves are closed to those obtained, making the hypothesis of the position-oriented control of the movement.

The second purpose of this chapter was to provide a general methodology that allows us to adapt the standard booster stages to the exigences of disabled drivers. This methodology takes origin from the biomechanical analysis of the muscular disease. The study continues with the mathematical formulation of the disease and the analysis of its impact on the model of the driver.

Starting from this, we can obtain useful informations about how it is possible to modify the steering assistance in order to keep into account this disease. Simulation results of different scenarios are used to validate the proposed steering assistance. Finally, numerical validation of these scenarios ends the proposed methodology.

## 4.5 Summary of the methodology of EPAS for Drivers with Reduced Mobility (EPAS-DRM)

– **Steering system**

$$\begin{aligned} J_v\ddot{\theta}_v(t) &= \tau_v - k(\theta_v(t) - \theta_s(t)) - B_v\dot{\theta}_v(t) \\ J_T\ddot{\theta}_s(t) &= -k(\theta_s(t) - \theta_v(t)) - N_2^2 B_m\dot{\theta}_s(t) - \frac{\tau_a}{N_1} + N_2 u \end{aligned}$$

with $J_T = \left(J_c + N_2^2 J_m + \frac{J_w}{N_1^2}\right)$

– **Tire-Road friction torque**

$$\tau_a = M_{\text{self-alig}} + M_{sticking}$$

– **Self-Alignment torque**

$$\begin{aligned} \dot{\bar{z}}_i(t) &= v_{ri} - C_{0i}(v_r)\bar{z}_i(t) - \kappa_i^{ss}|\omega r|\bar{z}_i(t) \quad (i = x, y) \\ \dot{\hat{z}}_y(t) &= \frac{G}{F_n L}v_{ry} - C_{0y}(v_r)\hat{z}_y(t) - \nu^{ss}|\omega r|\hat{z}_y(t) + \frac{|\omega r|}{L}\bar{z}_y(t) \end{aligned}$$

$$M_{\text{self-alig}} = -LF_n\left[\sigma_{0y}\left(\frac{1}{2}\bar{z}_y(t) - \hat{z}_y(t)\right) + \sigma_{1y}\left(\frac{1}{2}\dot{\bar{z}}_y(t) - \dot{\hat{z}}_y(t)\right) + \sigma_{2y}\left(\frac{1}{2}v_{ry} - \frac{G}{F_n L}\right)\right] \quad .$$

– **Sticking torque**

$$\dot{z}_z(t) = \dot{\phi}(t) - \frac{\sigma_{0z}|\dot{\phi}(t)|}{g_z(\dot{\phi}(t))}z_z(t)$$

$$M_{sticking} = -LF_n\left[\sigma_{0z}z_z(t) + \sigma_{1z}\dot{z}_z(t) + \sigma_{2z}\dot{\phi}\right]$$

– **LQ Control**

$$\min_{u^*} J = \min_{u^*}\int_{t_0}^{\infty} u^T(t)Ru(t) + x^T(t)Qx(t)\,\mathrm{d}t$$

$$u^*(t) = -R^{-1}B^T Px(t)$$

where $P$ satisfies the algebraic Riccati equation :

$$PA + A^T P - PBR^{-1}G^T P + Q = 0 \quad .$$

– **State-Observer**

$$\dot{\tau}_a \approx 0, \quad \dot{\tau}_v \approx 0$$

$$\tilde{z} = \left(\dot{\theta}_v, \dot{\theta}_s, \theta_v - \theta_s, \tau_v, \tau_a\right)^T$$

$$\dot{\tilde{z}} = \tilde{A}_e \tilde{z} + \tilde{B}_e u$$

$$y_2 = k(\theta_v - \theta_s) = k x_3.$$

$$\tilde{A}_e = \begin{pmatrix} A & G \\ \mathbb{O}_{2\times 3} & \mathbb{O}_{2\times 2} \end{pmatrix}, \quad \tilde{B}_e = \begin{pmatrix} B \\ 0 \\ 0 \end{pmatrix} \quad \tilde{C}_e = \begin{pmatrix} 0 & 1 & 0 & 0 & 0 \\ 0 & 0 & k & 0 & 0 \end{pmatrix}.$$

– **Power steering assistance**

$$\dot{\xi} = \begin{cases} -a\xi - b\sqrt{|\xi|}\dot{\theta}_v + c(\sqrt{|\xi| + \varepsilon})\tau_m, & \text{if } |\xi| \leq \xi_{max} \\ 0, & \text{else} \end{cases}$$

$$\tau_{ass} = (h_1(v) \times \xi) - \tau_{gz} \times \left[(1 - h_1(v)) + \frac{h_1(v)}{2}\left(1 - \text{sign}(\tau_m \times \tau_{gz})\right)\right]$$

$$h_1(v) = \begin{cases} 1, & \text{for } v = 0\,\text{km/h}; \\ 0, & \text{for } v = 30\,\text{km/h}. \end{cases}$$

# Chapitre 5

# Experimental validation NeCS-Car benchmark

## 5.1 Introduction

This chapter describes the experimental validation of the complete control architecture for the EPAS system and the testing of the general methodology on the NeCS-Car benchmark.

## 5.2 NeCS-Car benchmark

The NeCS-Car is a dedicated platform for tele-operation funded by the NeCS team at the Control System department of GIPSA-lab. It is based on a typical HIL architecture, where real hardware is joined together with simulated elements.

Tree configurations are used for this platform. In the first, a remote operator drives a steering wheel with and electrical motor (control station), that is connected to a PC-unit, that has the goal to give in input the feedback torque for the operator. In this case, the feedback torque is made up of simulated signals coming from algorithms implemented on the PC-unit.

If compared with the general control architecture, shown in Fig. 1.9, these signals include the simulated torsion of the steering shaft $F_t = k(\theta_v - \theta_s)$, the control input for the oscillation annealing $u$, the steering assistance torque $\tau_{ass}$ and the simulated model for the tire-road friction torque $\tau_a$. This last corresponds to the mathematical models of the self-alignment and the sticking tire-road friction torque, described in Chapter 2. This configuration is shown in Fig. 5.1.

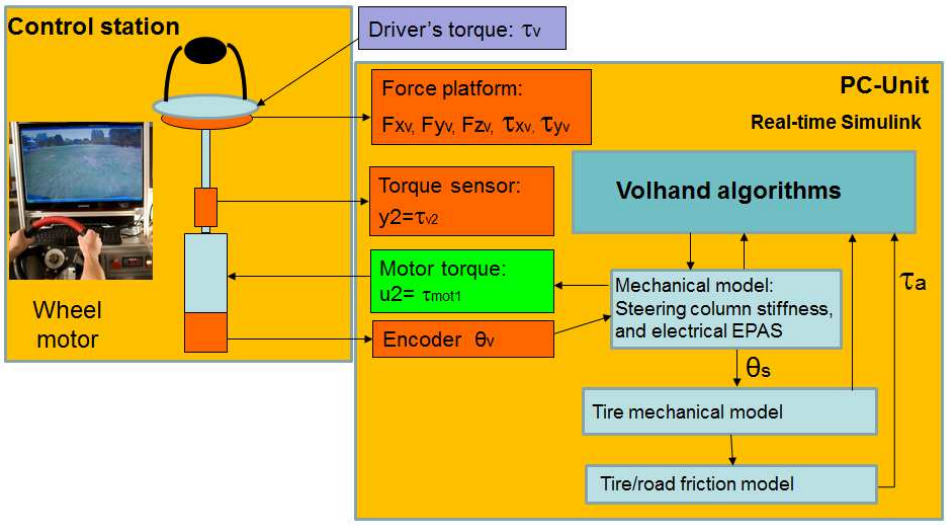


**Figure 5.1** – Configuration 1 of the experimental setup, when the tire-road friction torque is simulated in the PC-unit.

In the second configuration, the operator drives the vehicle via the control station, experiencing the torque feedback. In this case, PC-unit performs the connection between the control station and NeCS-Car. It receives in input the measured tire-road friction torque from the vehicle, then it sums this torque with all simulated signals and gives in output the overall feedback torque for the operator. In this case, the simulation block of the tire-road friction model is not used because NeCS-Car sensor measures the real friction force produced by the front-wheel movement. This configuration is shown in Fig. 5.2.

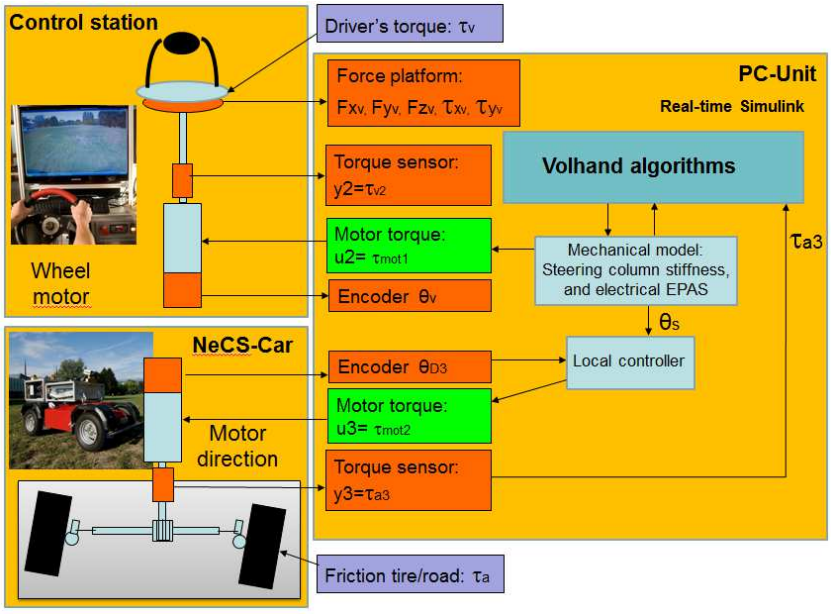


**Figure 5.2** – Configuration 2 of the experimental setup, when the vehicle is connected to the control station and the PC-unit and fed-back the tire-road friction torque.

The third mode is the tele-operation where NeCS-Car is connected to a second PC-Unit witch communicates with the first one by WLAN.

First configuration was used during preliminary tests to adapt the theoretical model to the experimental setup. All experimental results shown in this thesis have been obtained by using the second configuration.

### 5.2.1 Control station

As stated in previous paragraph, the control station allows to the operator to drive a steering wheel with its motor-shaft column. There are a torque sensor at the basis of the steering column and a force platform behind the wheel. These sensors allow to recover torques and forces exerted on the steering wheel by the operator on the reference space $(O, \overrightarrow{x_v}, \overrightarrow{y_v}, \overrightarrow{z_v})$. Torque sensor that provides this signal is Kistler 4503A and operates on the strain gage principle. An integral, digital measurement conditioning system produces analogue or digital output signals. We refer the reader to [53] for technical specifications. The torque signal at the origin of the rotational movement of the steering wheel is the driver's exerted torque over the $\overrightarrow{z_v}$ axis. This signal is shown as $y_2 = \tau_{v2}$ in Fig. 5.2.

Finally, the brush-less motor Kollmorgen transfers the desired torque to the wheel (signal $u_2 = \tau_{mot1}$ in Fig. 5.2). This asynchronous servomotor is coupled with a speed variator and is configured for a torque feedback control. We refer the reader to [54] for technical specifications about this motor. Its built-in encoder is connected to the PC-unit to get a measurement of the position of the steering wheel $\theta_v$.

### 5.2.2 PC-unit

The operating system on the PC-unit is Windows XP®. However, for real time communication of the controller, Ardence Real Time eXecution (RTX)® interface is used. Controller is designed in Matlab/Simulink 2007® and is converted to RTX®, that is a rapid prototyping product by Quanser®.

Analog inputs, encoder inputs and analog outputs are measured but by a Quanser® multi-Q PCI card.

### 5.2.3 NeCS-Car unit

NeCS-Car is a vehicle with a weight of 200 kg and in scale 1 :4 w.r.t. a standard commercial vehicle. The steering brushless motor mounted on the vehicle has similar features to the motor of the control station. The rack and pinion gear assembly converts its

rotational motion into the linear motion that turns the front wheels.

The torque feedback is measured by a sensor mounted between the steering motor and the pinion gear. It corresponds to the signal $y_3 = \tau_{a3}$ in Fig. 5.2.

Propelling on the NeCS-Car is performed by a DC motor connected to the rear wheels. The mechanical assembly of the NeCS-Car is shown in Fig. 5.3.

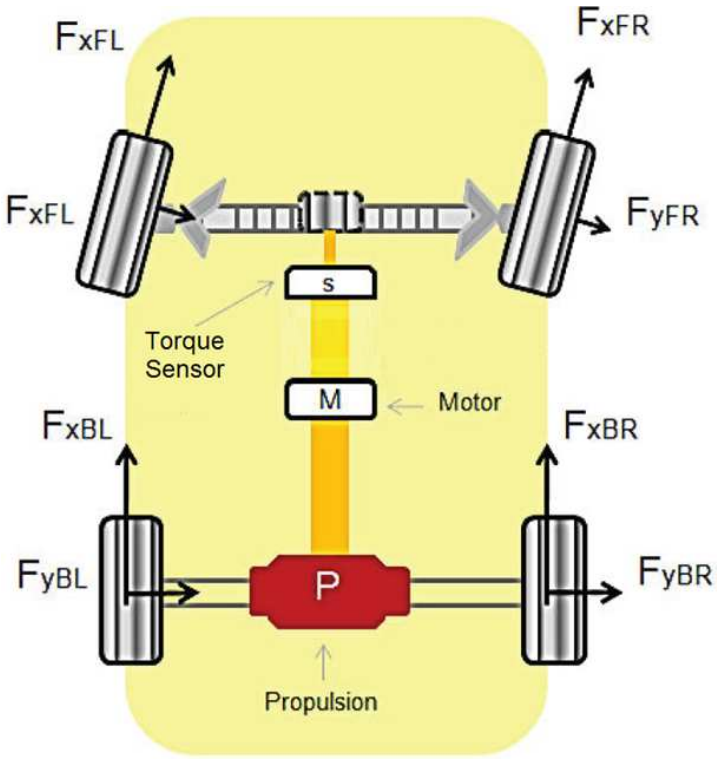


**Figure 5.3** – Architecture of the NeCS-Car

## 5.3 Implementation of the state-space model on the HIL setup

This section deals with preliminary tests to adapt the theoretical architecture to the HIL setup.

Mathematical model of the EPS system (see Eqs. (2.3.1) and (2.3.2)) includes the influence of the inertia and viscosity of the steering wheel and the column shaft. On the HIL setup, these elements are part of the hardware in the control station. To avoid the simulation also of the hardware elements on the system, it is necessary to re-write equations of the mathematical model, by making a separation between real and simulated values. At this aim, let us make the following assumption :

**Hypothesis 5.3.1**

*let $J$ and $B$ to be defined as the difference of the values adopted in simulation (respectively, $J_v$ and $B_v$) and values of the setup system (respectively, $J_0$ and $B_0$)*

$$J_v = J + J_0 \tag{5.3.1}$$
$$B_v = B + B_0 \quad . \tag{5.3.2}$$

Let us substitute $J_v$ and $B_v$, as resulting from Eqs. (5.3.1) and (5.3.2), in Eq. (2.3.1), as follows :

$$(J + J_0)\ddot{\theta}_v + (B + B_0)\dot{\theta}_v = \tau_v - k(\theta_v - \theta_s) \tag{5.3.3}$$

and let us apply the Laplace transform to obtain the value of $\theta_v$, as function of the driver's torque $\tau_v$ and the motor torque $C_m$, coming from the PC-unit

$$(J + J_0)s^2\theta_v + (B + B_0)s\theta_v = \tau_v - k(\theta_v - \theta_s) \tag{5.3.4}$$

Now, let us divide the real inertia and viscosity from residual ones

$$(J_0 s^2 + B_0 s)\theta_v = \tau_v - k(\theta_v - \theta_s) - (Js^2 + Bs)\theta_v \tag{5.3.5}$$

It follows that

$$C_m = -k(\theta_v - \theta_s) - (Js^2 + Bs)\theta_v \tag{5.3.6}$$

is the simulated torque given to the motor and

$$\theta_v = \frac{1}{(J_0 s^2 + B_0 s)}\,(\tau_v + C_m) \tag{5.3.7}$$

is the real steering wheel angle, obtained from the steering wheel and the column.

To obtain the relation between the steering wheel position $\theta_v$ and the column-shaft angle $\theta_s$, let us apply the Laplace transform on Eq. (2.3.2), as follows

$$J_T s^2\theta_s + N_2^2 B_m s\theta_s = k(\theta_v - \theta_s) + \frac{\tau_a}{N_1} + N_2 u \tag{5.3.8}$$

By collecting all the terms in $\theta_s$, it is possible to obtain

$$\theta_s = \frac{1}{J_T s^2 + N_2^2 B_m s + k}\left(k\theta_v + \frac{\tau_a}{N_1} + N_2 u\right) \tag{5.3.9}$$

Eqs. (5.3.7) and (5.3.9) allow to adapt the state-space representation of the EPS model to the HIL experimental setup. For the same input, these equations produce the same output of the state-space model in Eqs. (2.3.1) and (2.3.2).

### 5.3.1 Identification of residual viscosity and inertia on the HIL setup

Residual parameters of the inertia and viscosity of the control station $B_0$ and $J_0$ needs to be identified to be able to test the general architecture on the experimental setup.
The key factor of obtaining a good result of identification is selecting the right input signals in order to excite the system over all the frequency range of interest. At this aim, two identification methods are used. They differ each other for the input signal that is used for the identification.
In the first method, a step signal is used as input of the system. Parameters of the system can be easily obtained, starting from the analysis of the transfer function of the system, which behaves as a second order system.
The second method uses one of the signals, which is traditionally used for non-parametric model identification : i.e. the Pseudo-Random Binary Sequence (PRBS) signal. The PRBS signal is a deterministic signal with the property that its auto-correlation function corresponds to the auto-correlation function of the white noise signal ([91], [80], [81]).

#### 5.3.1.1 Step response of the system

The steering model can be described in open loop as a first-order transfer function in Laplace domain

$$G_{OL}(s) = \frac{\dot{\theta}_v}{\tau_v} = \frac{1}{J_0 s + B_0} \tag{5.3.10}$$

The corresponding closed loop system with a proportional gain $k_1$ is

$$G_{CL}(s) = \frac{\theta_v}{\tau_v} = \frac{k_1}{J_0 s^2 + B_0 s + k_1} \tag{5.3.11}$$

The experimental procedure to obtain values for $J_0$ and $B_0$ with the step input sequence is the following :

– the step input sequence of $\tau_{mot1}$, output of the pc-unit, is applied on the electrical motor of the control station in closed loop.
– As consequence of this input, the steering wheel starts to oscillate as a closed-loop system. This signal $\theta_v$ is saved to use it into the identification algorithm. This output is shown in Fig. 5.4. From the analysis of this output, it is possible to identify $J_0$ and $B_0$.

At this aim, let us consider the standard form for a transfer function of a second order system

$$G(s) = \frac{1}{\frac{1}{\omega_n^2} s^2 + \frac{2\xi_0}{\omega_n} s + 1} \tag{5.3.12}$$

where $\omega_n$ is the natural frequency of the system and $\xi_0$ is the damping coefficient.

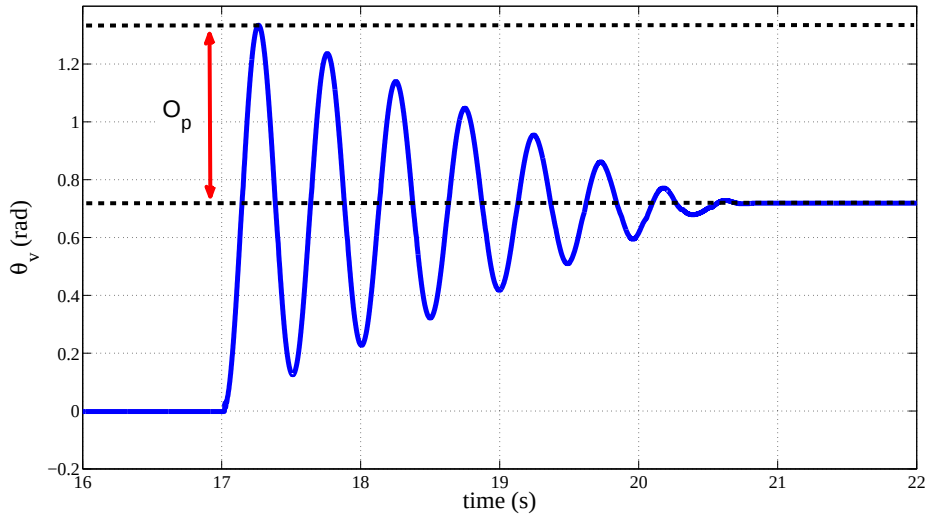


**Figure 5.4** – Output of the system to the step input.

By inspection of the output of the system in Fig. 5.4, it is possible to obtain the overshoot value of the system $O_p = 0.854$. The equation relating $O_p$ with $\xi_0$ is the following

$$O_p = \exp^{-\frac{\pi\xi_0}{\sqrt{1-\xi_0^2}}} \quad , \tag{5.3.13}$$

so the corresponding value for $\xi_0 = 0.05$.

The equation relating $\omega_n$ and $\xi_0$ is

$$\omega_n = \omega_0\sqrt{1-\xi_0^2} \tag{5.3.14}$$

By comparing Eq. (5.3.11) with Eq. (5.3.12), it is possible to obtain the corresponding values for $J_0$ and $B_0$

$$\frac{J_0}{k_1} = \frac{1}{\omega_n^2} \Rightarrow J_0 = \frac{k_1}{\omega_n^2} \tag{5.3.15}$$

$$\frac{B_0}{k_1} = \frac{2\xi_0}{\omega_n} \Rightarrow B_0 = \frac{2\xi_0 k_1\sqrt{1-\xi_0^2}}{\omega_n} \tag{5.3.16}$$

By substituting numerical values ($k_1 = 5$ and $\omega_n = 12.56$ rad s$^{-1}$, it is possible to obtain resulting values for the inertia and the viscosity are $J_0 = 0.0303$ kgm$^2$ and $B_0 = 0.039$ N m rad$^{-1}$ s, respectively.

#### 5.3.1.2 Identification via PRBS input sequence

The experimental procedure to obtain values for $J_0$ and $B_0$ with the PRBS input sequence is the following :

– the PRBS input sequence of $\tau_{mot1}$, output of the pc-unit, is applied on the electrical motor of the control station in open loop. This sequence is shown in Fig. 5.5.
– As consequence of this input, the steering wheel starts to oscillate with a variable angular speed. This signal $\dot{\theta}_v$ is saved to use it into the identification algorithm. This output is shown in Fig. 5.6.

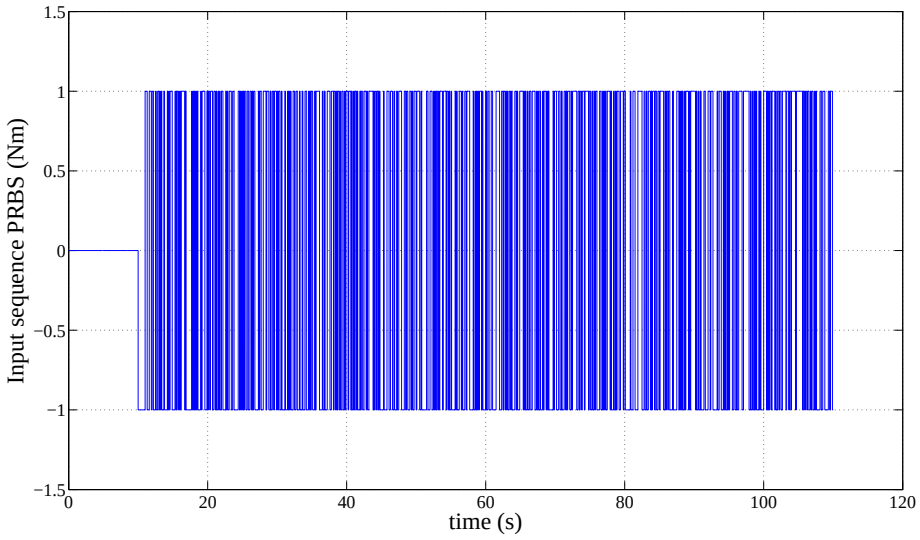


**Figure 5.5** – Sequence PRBS that is given in input for the parametric identification.

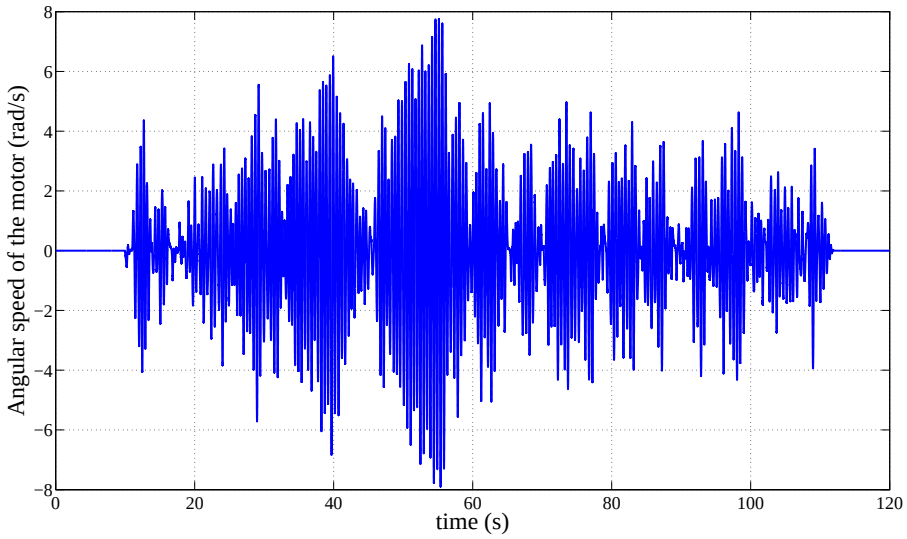


**Figure 5.6** – Output of the system to the proposed input. This signal is then used for the least squares identification.

We make the assumption that the model behaves as a first order transfer function in closed loop with a proportional gain $k_1$

$$G_0(s) = \frac{\dot{\theta}_v}{\tau_{mot1}} = \frac{k_2}{1 + T_p s} = \frac{1}{B_0 + J_0 s} \tag{5.3.17}$$

Under this assumption, the parameters to identify correspond to :

$$J_0 = \frac{T_p}{k_2} \qquad B_0 = \tfrac{1}{k_2} \tag{5.3.18}$$

The solution of this problem is obtained by applying a non-linear least squares algorithm ([56], [11]), implemented with the software Matlab 2011®. The resulting values for the inertia and the viscosity are $J_0 = 0.0325$ kgm$^2$ and $B_0 = 0.072$ N m rad$^{-1}$ s, respectively.

As concluding remark, it is possible to say that both identification methods produce very similar values. It is possible to conclude that identified values are appropriate. For the following, values obtained with the PRBS method are used.

## 5.4 Validation of the oscillation annealing control

Due the complexity of the general architecture, the experimental validation is shown following an incremental principle. First, the oscillation annealing control and the torque observer are validated without the steering assistance. Then, the steering assistance model is added to the controller and the observer and experimental tests are done on the complete architecture.

### 5.4.1 Steering column in open loop

Simulation results about the EPS system show that the system becomes unstable, when there is a variation of the driver's exerted torque. The instability is physically due to the torsion of the steering column. From a mathematical point of view, it can be checked with the two imaginary poles of the state matrix of the system in Eq. (3.2.5) ($p_{1,2} = -1.0023 \pm 56.0151i$), while the last pole is stable ($p_3 = -4.9386$).

To test the effect of this instability on the HIL setup, an operator is sit down on the control station. He puts hands at 10 :10 in clock-code. For safety reasons, NeCS-Car is not connected to the control station, but the tire-road friction torque is simulated for a speed of the vehicle of 0 km h$^{-1}$ (see configuration 1 in Fig. 5.1). This implies that the self-alignment torque is negligible and the main responsible of the driving feedback is the sticking torque. The driver applies the input trajectory shown in Fig. 5.7 : he turns the steering wheel in anti clock-wise of 90 °, then leaves it for 4 s and repeats the manoeuvre in clock-wise.

Fig. 5.8 shows the response of the real system in terms of angular speed of the steering wheel : when the driver leaves the system, the steering system starts to oscillate (see the profile of $\dot{\theta}_v$ between 4 and 6 s). It stops when all the energy of the system is dissipated. This experimental results is compatible with the simulations, shown in Chapter 3. These oscillations are uncomfortable for the driver, but they affect also the measure of the torque sensor and, consequently, the torque feedback of the electrical motor. For these reasons, it is necessary to compensate them with a proper controller.

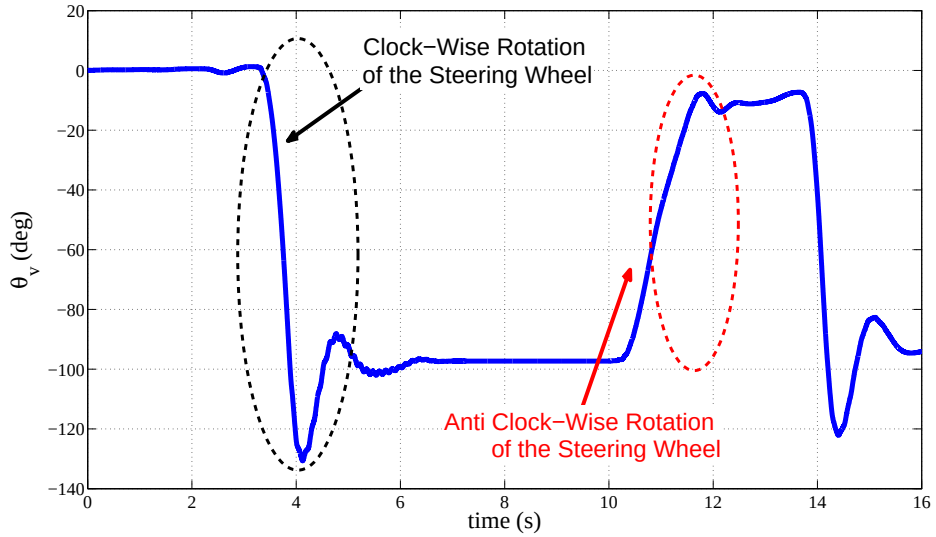


**Figure 5.7** – Trajectory applied from the operator on the steering wheel in open loop.

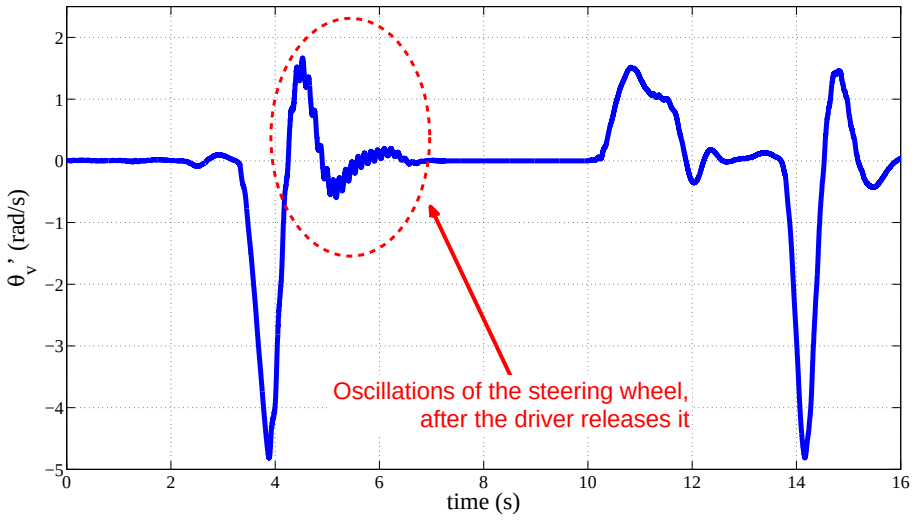


**Figure 5.8** – Angular rate of the steering wheel in open loop. Note the oscillations of the systems between 5 and 8 s.

### 5.4.2 Steering column in closed loop

The oscillations shown in previous section can be annealed by introducing the optimal LQ controller, shown in Chapter 3, under the constraint to not modify the impedance between the driver's and the load torque at low frequency.

To test the advantages of the oscillation annealing control, an operator is sit down on the control station. He puts hands at 10 :10 in clock-code and repeats the same manoeuvre shown in the open-loop case. He turns the steering wheel from the initial position to 90 ° in clock-wise, then releases the steering wheel for 6 s and finally he makes another turn in anti clock-wise.

As in the open loop case, NeCS-Car is not connected to the control station, but the tire-road friction torque is simulated for a speed of the vehicle of 0 $\mathrm{km\,h^{-1}}$ (see configuration 1 in Fig. 5.1).

The exerted driver's trajectory is shown in Fig. 5.9 and is similar to the open loop case. In Fig. 5.10 the angular speed of the steering wheel is shown. Oscillations of the steering column are completely annealed with the introduction of the inner control loop. This result validates the simulations, shown in Chapter 3. As further validation, it is

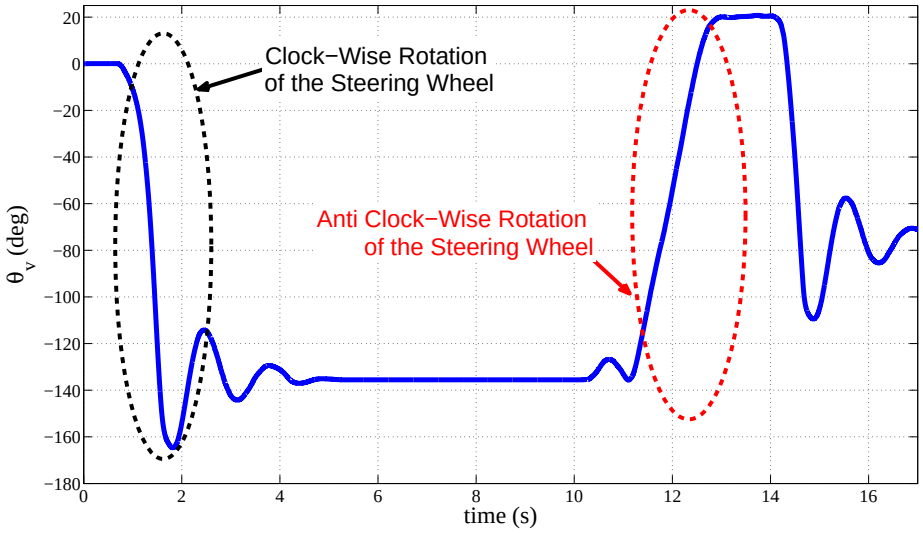


**Figure 5.9** – Trajectory applied from the operator on the steering wheel in closed loop.

possible to calculate the Fast Fourier Transform (FFT) of the measured torsion on the experimental setup. In Fig. 5.11, a comparison between FFTs of the torsions measured on the system in open loop and in closed loop is done. Also in frequency domain, the peak of oscillation that appears in open loop is completely filtered in closed loop.

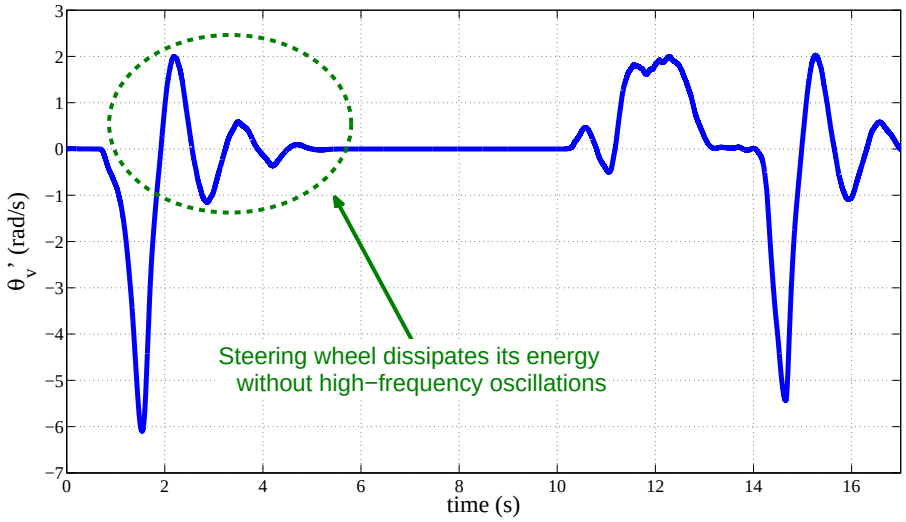


**Figure 5.10** – Angular rate of the steering wheel in closed loop. The system dissipates its energy without oscillations at low frequency.

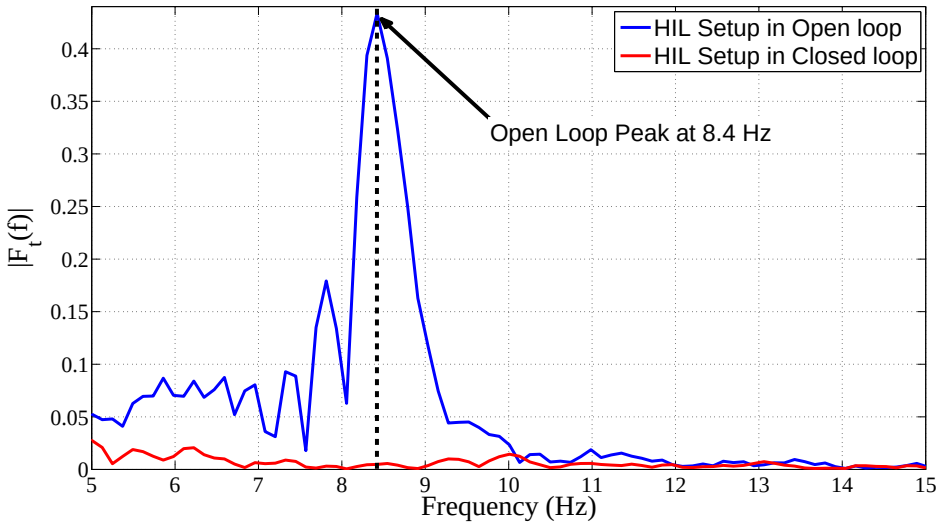


**Figure 5.11** – FFT of the signals of the torsion of the steering wheel in open (blue) and in closed loop (red).

## 5.5 Validation of performances of the torque observer

The torque observer synthesized in Chapter 3 plays an important role in the general context, because it allows to recover informations about inner states of the system and about exogenous inputs acting on it. Information about state variables are given in input to the LQ control for the oscillation annealing, while the estimate of the driver's torque

is given in input to the booster stage to provide the correct steering amplification. In other words, good results of the estimation contribute to make the entire system work properly.

The observer is designed under the hypothesis that it is possible to measure the angular rate $\dot{\theta}_s$ and the torsion $F_t = k(\theta_v - \theta_s)$ of the steering column. On the experimental setup, $\dot{\theta}_s$ and $F_t$ are simulated signal. The driver's exerted torque $\tau_v$, the steering-wheel position $\theta_v$ and the tire-road friction torque $\tau_a$, are measured on the experimental setup.

### 5.5.1 Performances of the observer with the simulated tire-road friction torque

To validate the performances of the observer, let us consider the case of a trajectory exerted by a driver, who can manoeuvre with two hands at 10 :10 in clock-code. The oscillation annealing control is active, but the steering assistance is inactive.
During these preliminary validation tests, NeCS-Car is not connected to the control station and the friction torque is simulated for a speed of the vehicle of 0 $\mathrm{km\,h^{-1}}$.

The applied trajectory on the steering wheel is shown in Fig. 5.12. The driver turns the steering wheel many times over a test period of about 40 s. The comparison between the

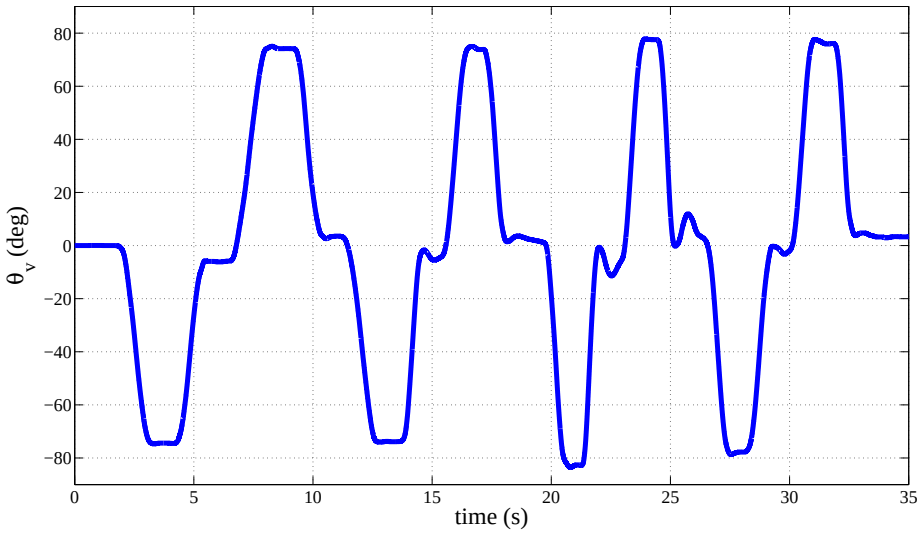


**Figure 5.12** – Trajectory applied from the operator on the steering wheel to validate performances of the observer.

estimated torque $\hat{\tau}_v$ and the measured one $y_2 = \tau_{v2}$ is shown in Fig. 5.13. The numerical noise, that affects the measure of $\dot{\theta}_s$, and the measure noise, that acts on $F_t$ do not modify the global performances observer. It is possible to calculate the estimation error

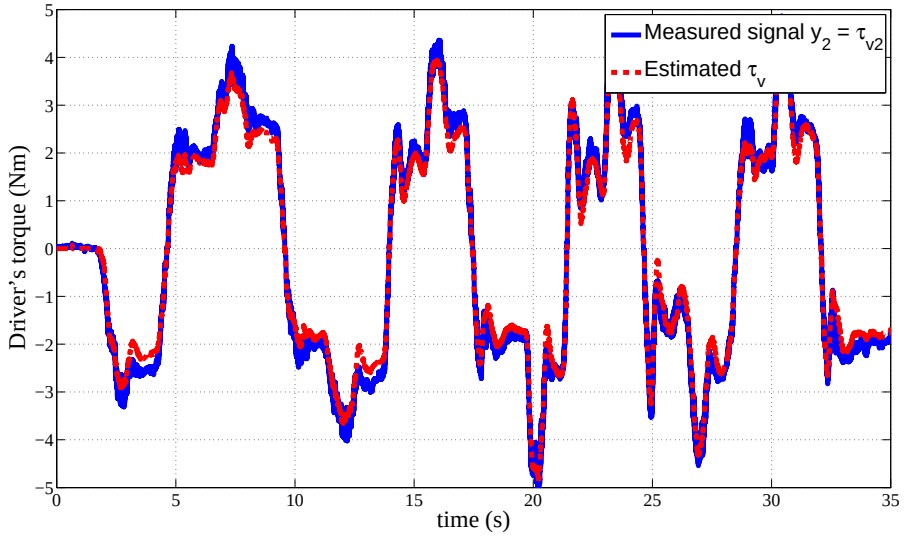


**Figure 5.13** – Comparison between the measured driver's exerted torque and the estimated one.

$E_1$, that is defined as the following difference

$$E_1 = \tau_{v2} - \hat{\tau}_v \tag{5.5.1}$$

This error is shown in Fig. 5.14. Even if the observation error increases when the angular speed of the steering column augment, it keeps in acceptable range. The angular speed of the steering wheel is shown in Fig. 5.15. This phenomenon is due to the influence of the mechanical noise of the steering wheel. As this noise depends from the angular rate, it is difficult to filter properly.

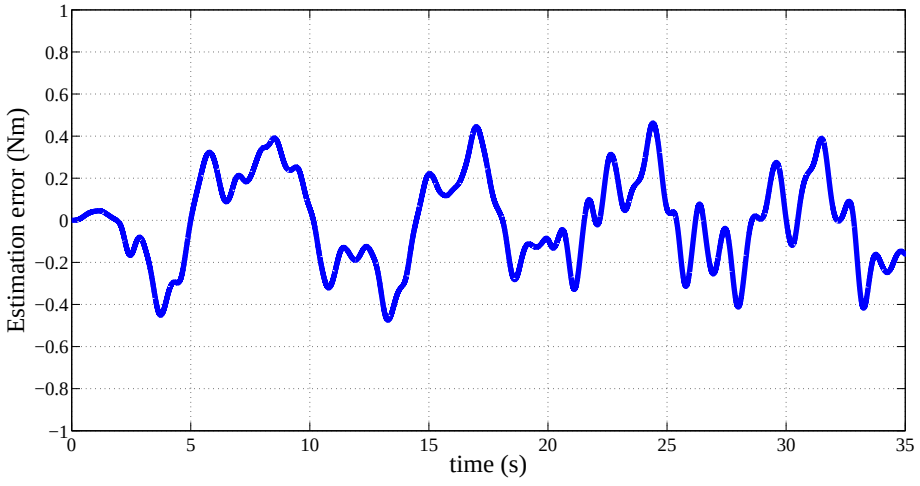


**Figure 5.14** – Error between the measured driver's torque and the estimated one.

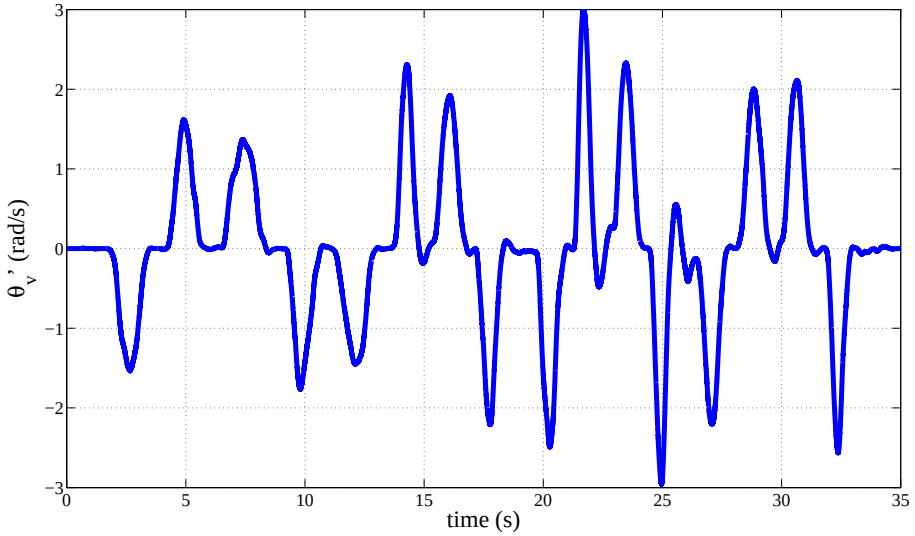


**Figure 5.15** – Angular rate of the steering wheel.

In Fig. 5.16, the comparison between the estimated tire-road friction torque $\hat{\tau}_a$ and the output of the simulated model $\tau_a$ is shown. This comparison allows to analyse performances of the observer in this case.

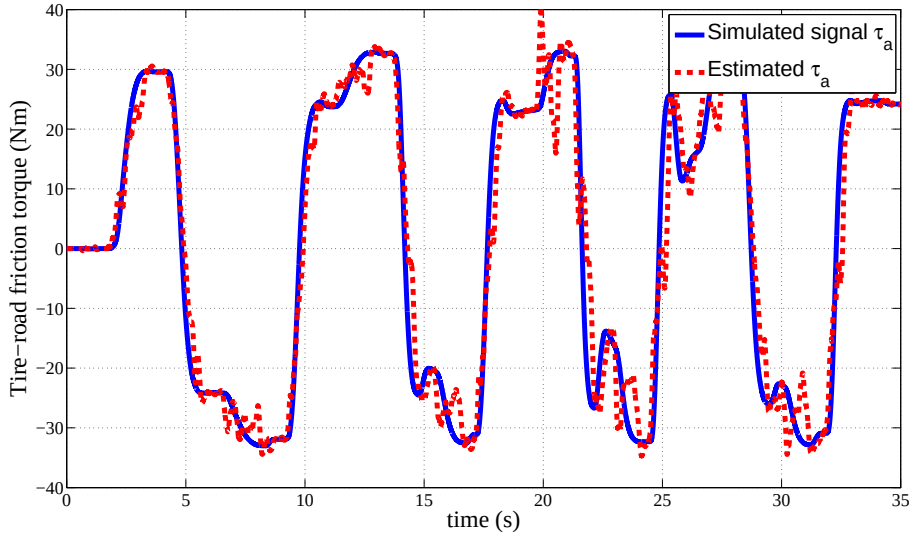


**Figure 5.16** – Comparison between the simulated tire-road friction torque and the estimated one.

In this case, the estimation error is defined as follows

$$E_2 = \tau_a - \hat{\tau}_a \tag{5.5.2}$$

In Fig. 5.17, it is possible to see that this error is negligible and the observer performance are satisfying.

Note also that, by dividing the value assumed by the friction torque at low frequency (about 30 N m) with the gear ratio $N_1 = 13.67$, it is possible to obtain the value of the driver's torque during at the same time instant (about 2.2 N m), meaning that the LQ control preserves the impedance relation between two torques. This property cannot be verified at high frequency, because of the influence of the angular speed and acceleration of the steering wheel.

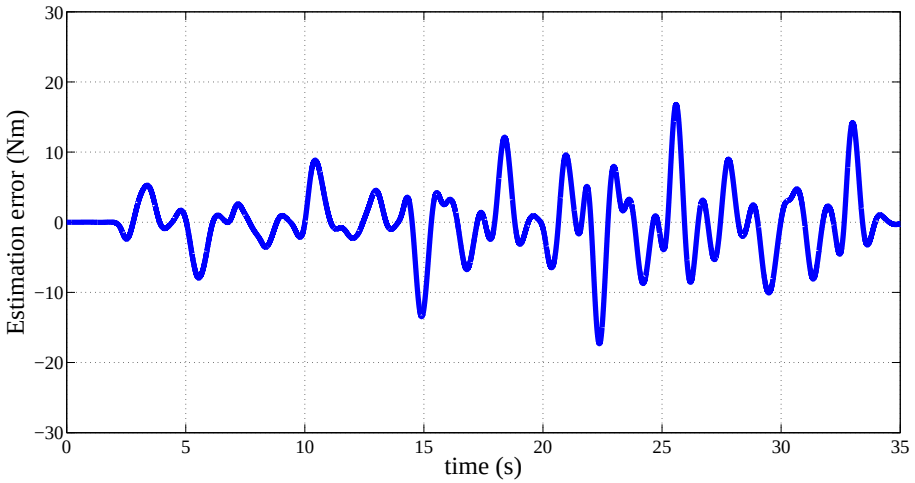


**Figure 5.17** – Error between the simulated tire-road friction torque and the estimated one.

### 5.5.2 Performances of the observer with the NeCS-Car

A further validation of the observer can be done using the torque input obtained with the NeCS-Car. These measures contribute also to validate experimentally the mathematical model used to simulate the tire-road friction torque.

First, let us consider performances of the observer w.r.t the real tire-road friction torque. In Fig. 5.18, the estimated torque is compared with the measured one. In spite of the measurement error, the observer performances are globally satisfying. It is possible to diminish the transient error at the cost of a high gain of the observer.

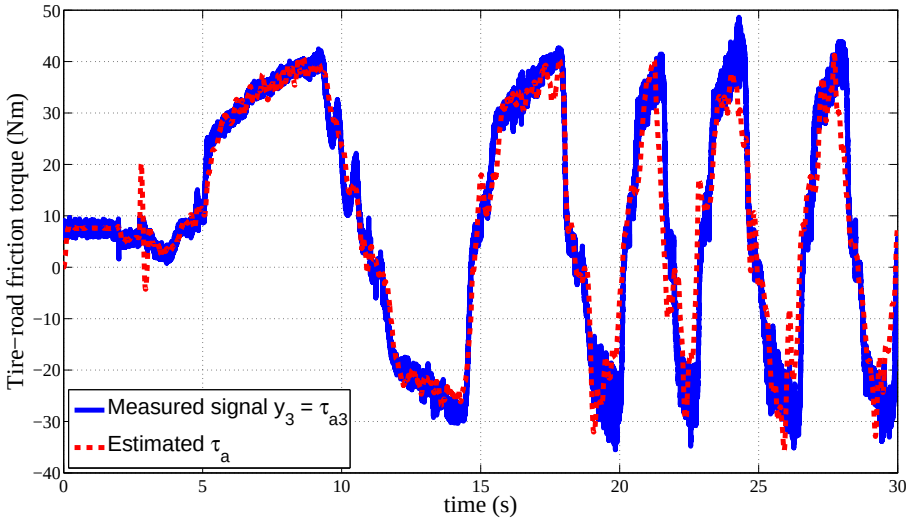


**Figure 5.18** – The friction torque obtained from measures on the NeCS-Car is compared with the estimated tire-road friction torque.

In Fig. 5.19, the comparison between the simulated friction torque and the real measures obtained from the NeCS-Car is proposed for the same input trajectory. It is possible to observe that the simulated torque is realistic, if compared to the measured one.

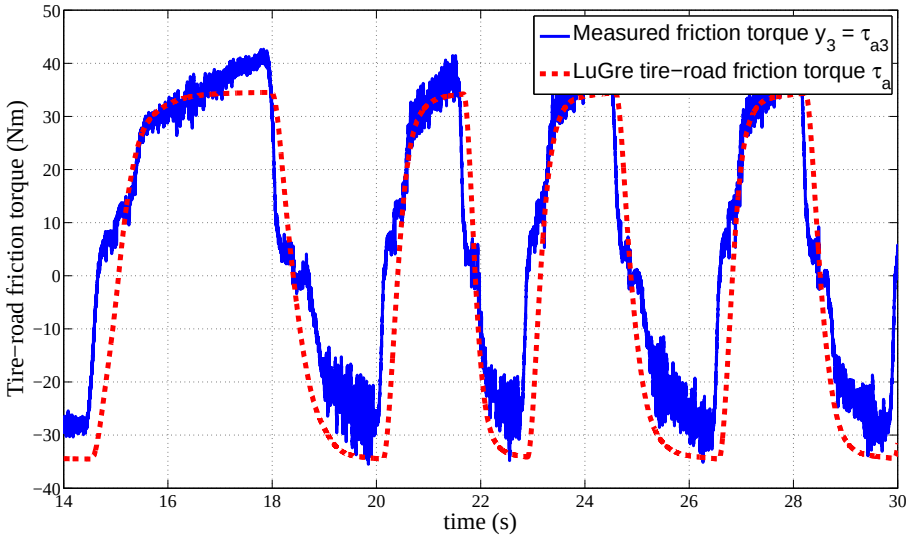


**Figure 5.19** – The tire-road friction torque, obtained from measures on the NeCS-Car, is compared with the tire-road friction torque obtained with the mathematical model of LuGre.

## 5.6 Experimental validation of the methodology to adapt the steering assistance to disabled drivers

Last remaining step of the proposed methodology is the experimental validation of the test scenarios. To perform this task, the proposed steering assistance is installed on the HIL setup. Nevertheless, the correct functioning of the proposed assistance requires an estimation of the mass of the upper limb.

In Chapter 4, an off-line estimation is proposed basing on a bio-mechanical model of the upper limb and on the use of anthropometric tables. In the following Section, an on-line estimation procedure is proposed and tested. After that, the measure of the estimated mass is used to test the steering assistance for scenarios of interest.

### 5.6.1 On-line estimation of the mass of the upper limb

This procedure makes use of the EPS electrical motor, simulated in our experimental setup. A Proportional Derivative (PD) controller is implemented on the pc-unit. It sends torque-input $u$ to the electrical motor, according to a reference trajectory. This torque causes the displacement of the steering wheel, according the predefined trajectory.

During this procedure, the operator is sit-down on the control-station with the upper limb relaxed. In this way, the only torque that is measured from the sensor is that one due to the weight of the upper limb.
Using estimations of the torque observer (i.e. the estimated position of the steering wheel $\hat{\theta}_v$ and the estimated driver's torque $\hat{\tau}_v$), it is then possible to obtain the proper value for the mass parameter of the upper limb with the relation

$$\hat{\tau}_v = \hat{m} g R \cos\Phi \cos\hat{\theta}_v \Rightarrow \hat{m} = \frac{\hat{\tau}_v}{g R \cos\Phi \sin\hat{\theta}_v} \tag{5.6.1}$$

To validate this procedure, 3 experiments are trained out with the reference signal with a frequency $f_r = 2.51\ \mathrm{rad\,s^{-1}}$. All the experiments are trained with the NeCS-Car connected to the control station.
The reference trajectory imposed for all the experiments is shown in Fig. 5.20. To avoid numerical instabilities ($\sin 0 = 0$), the trajectory is kept in a stable region of the steering wheel and varies between 30 and 150 °.

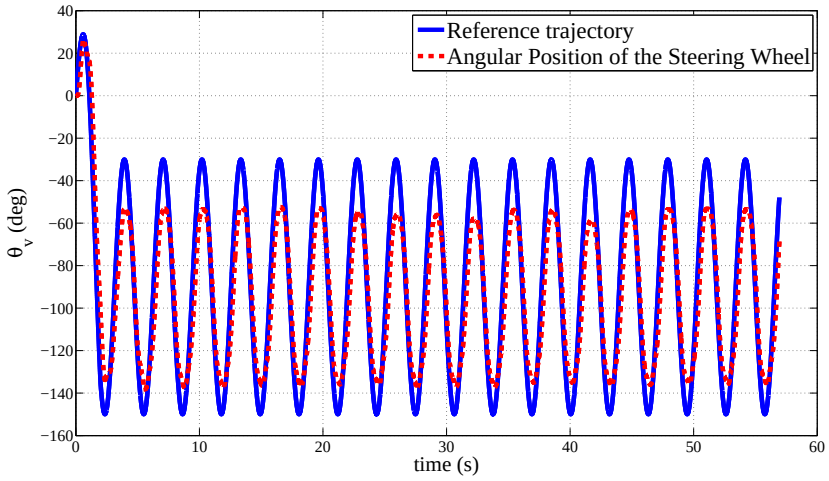


**Figure 5.20** – Trajectory on the steering wheel, that is used for the identification. The reference trajectory (blue) with the effective position of the steering wheel (red).

The first experiment has been trained out with the ball fixed on the steering wheel. Results of the estimations are shown in Fig. 5.21. In this figure, it is possible to see the profile of the estimated mass w.r.t. the position of the steering wheel.

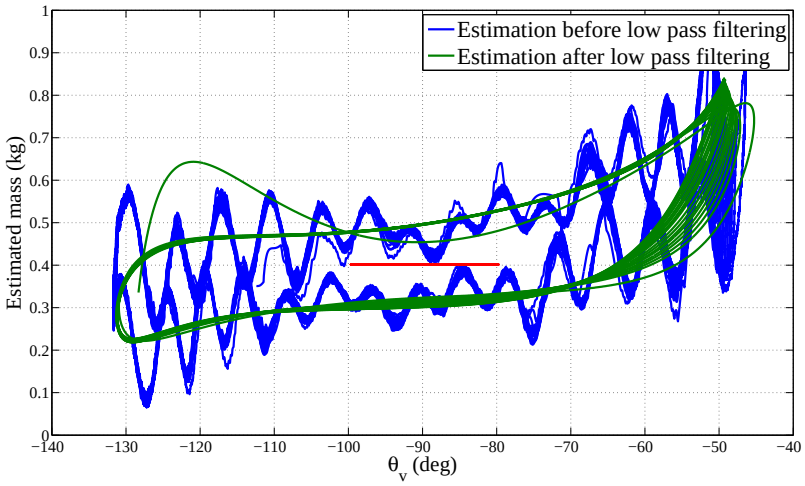


**Figure 5.21** – Estimation results of the Experiment 1. In blue, the signal of the estimated mass is not filtered, so the measure is affected by dry friction and mechanical disturbances. In green, the signal is filtered and provides an average value of 400 g (red line).

Let us analyse the estimation result, without any filter. This estimate is affected by 2 disturbances. The first one is the dry friction acting on the steering wheel. It depends from the angular speed of the steering wheel and behaves as an additive noise acting on the system. Filtering of this phenomenon is not easy to perform. Its value is about 0.1 N m.

The second disturbance is due to the mechanical noise , due to the asynchronous servo-motor used for the experimentations. Range of measures of this motor does not reach the accuracy demanded for these measures.
Let us consider the same signal, after the application of a low-pass filter of 4th order and cut-off frequency $Fc = 1$ Hz. The estimated value is stable around an average value of 0.400 g. This value has been calculated for the range of positions $\theta_v \in (-100\ ^\circ : -70\ ^\circ)$, where boundary effects are not present.

The second experiment is done adding a mass of 600 g on the previous ball, under the same conditions of the first one (same input trajectory and with the vehicle). Estimation results are shown in Fig. 5.22.
Let us analyse the estimation without filtering. Disturbances due to the dry friction and the mechanical noise of the motor are presents. Value of the dry friction is about 0.1 N m, meaning that the bigger weight does not influence the angular speed of the steering wheel.
The average value of the estimation is calculated for positions $\theta_v \in (-110\ ^\circ : -70\ ^\circ)$ on the filtered signal. It corresponds to 0.929 g.

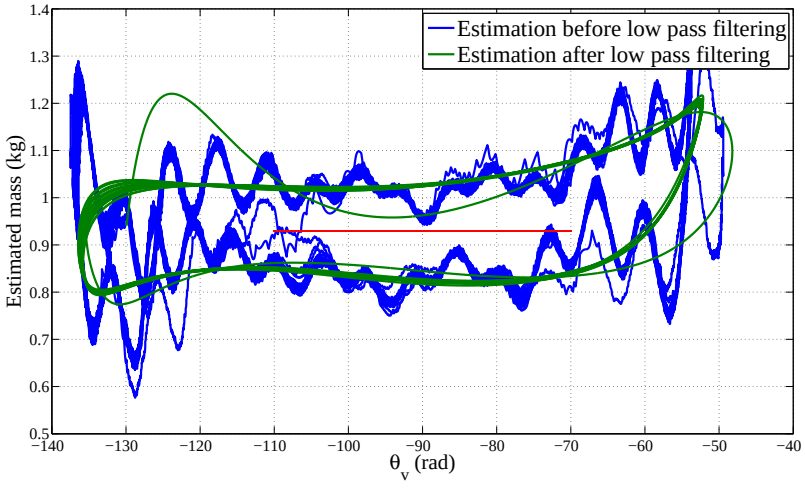


**Figure 5.22** – Estimation results of the Experiment 2. In blue, the signal of the estimated mass is not filtered, so the measure is affected by dry friction and mechanical disturbances. In green, the signal is filtered and provides an average value of 0.929 g (red line).

Third test is done with an human operator, 33 years old with a weight of 76 kg. The operator has its right upper limb linked on the steering wheel. We ask to the operator to be completely relaxed.
Results of the estimation of the mass parameter $\hat{m}$ of the right upper limb are shown in Fig. 5.23. The steering wheel moves on the same side of the arm, that we are testing. During the test, the configuration of the upper limb changes : the arm is outstretched on the steering wheel for positions $\theta_v \in (-80\ ^\circ : -70\ ^\circ)$, while the operator has the arm

close to his body for positions $\theta_v \in (-130\ ^\circ : -120\ ^\circ)$.
This effect influences the estimation of the mass parameter, because the ratio between $l_{CG}$ and $l$ in Eq. (4.3.11) changes during the test. The average value varies linearly between :
– upper limit = 1.608 kg for the outstretched configuration, $\theta_v \in (-80\ ^\circ : -70\ ^\circ)$ ;
– lower limit = 1.124 kg for the unextended configuration, $\theta_v \in (-130\ ^\circ : -120\ ^\circ)$ ;.

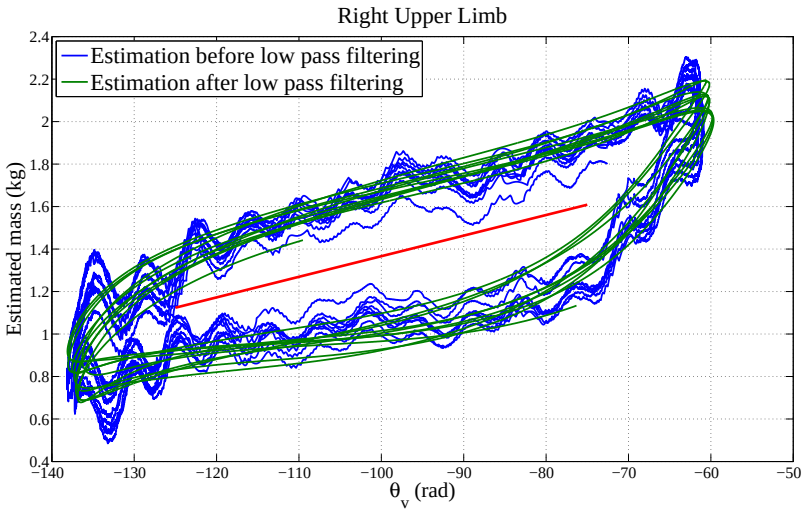


**Figure 5.23** – Estimation results of the Experiment 3. In blue, the signal of the estimated mass is not filtered, so the measure is affected by dry friction and mechanical disturbances. In green, the signal is filtered and provides an average value between 1.608 kg and 1.124 kg (red line).

Forth test is done with the same operator of the third experiment, but the left upper limb is linked to the steering wheel.
Being the left arm in opposite position w.r.t. the linking point to the steering wheel, the upper limb maintains always the same configuration front of the steering wheel, as it is shown in Fig. 5.24. So, results of the estimation settle around the average value of 1.617 kg for positions $\theta_v \in (-130\ ^\circ : -70\ ^\circ)$.

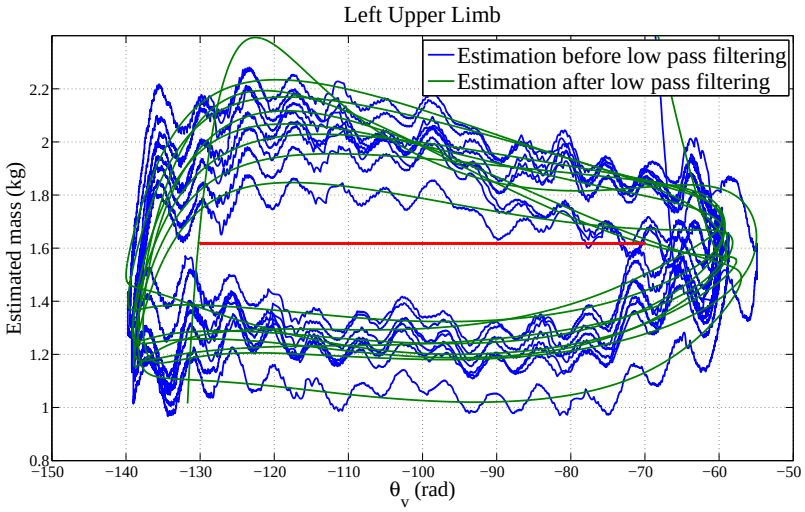


**Figure 5.24** – Estimation results of the Experiment 4. In blue, the signal of the estimated mass is not filtered, so the measure is affected by dry friction and mechanical disturbances. In green, the signal is filtered and provides an average value of 1.617 kg (red line).

.

Now, let us consider the estimation obtained from Eq. (4.3.13) using the bio-mechanical model of the upper limb. For a men of 76 kg, the anthropometric estimation provides a value of 1.78 kg. This value corresponds to the stable configuration of the upper limb.

Table 5.1 shows a comparison between estimated results and their real values for each test.

| Test | Measured value | Mass parameter value | Estimated value |
|---|---|---|---|
| Fixed ball | 400 g | N.A. | 400 g |
| Fixed ball + Inertia | 1000 g | N.A. | 929 g |
| Right upper limb | N.A.<br>N.A. | 1780 g | 1608 g outstretched config.<br>1124 g unextended config. |
| Left upper limb | N.A. | 1780 g | 1617 g |

**Table 5.1** – Comparison between estimated results and real values for each test.

As concluding remark, this estimation is strictly influenced by the configuration of the upper limb front to the steering wheel. Moreover, it is affected by musculoskeletal tensions of the upper limb and bases on the strong hypothesis that the subject is completely relaxed during the test. This hypothesis cannot be always verified. However, it is an on-line method that provides results, which are compatible with the anthropometric procedure. For safety reasons, the value of the mass parameter used in the assistance is approximated to the lower limit.
An alternative approach consists into saving all values of the estimation for all different positions ; the advantage is a more adapted steering assistance that keeps into account

the configuration of the upper limb w.r.t. the steering wheel.

### 5.6.2 Experimental validation of test scenarios

In this thesis, main goal of experimental validation of the proposed methodology is to give a quantitative proof of the applicability of the proposed assistance. The goal is not to provide a statistical campaign with many subjects. Only one subject has been studied.

During all tests the control loop to delete oscillations of the steering column is active, the torque observer is also active and the NeCS-Car is connected to the control station. This last element allows to monitor the steering assistance under a realistic road feedback. For each scenario, performance indexes are calculated using real measuring signals. Each test is done with the operator, who can turn the steering wheel with only one arm through the use of a ball.

#### 5.6.2.1 Parking manoeuvre

This test scenario is made with the vehicle at stand-still. We ask to the operator to turn the steering wheel from 0 ° to 90 ° in clockwise, then to keep the position for 2 s and finally to bring back the ball to its initial position.

This test is repeated twice. The first one, the operator makes to movement with the support of the standard steering assistance of Eqs. (1.2.2) and (1.2.3). The second one, the modified steering assistance of Eqs. (4.3.17) and (4.3.18) is used to help the movement. To be able to compare the two experiences, a constraint in terms of timing and speed of the movement has been required to the operator. A fast movement entails the growth of the angular speed of the steering wheel, with consequences on the measure of the mechanical power, because of a consequent augment of the dissipated energy on the tires.
Resulting trajectories are shown in Fig. 5.25. The weight of the arm is motor between time instants $t \in (t_0 : t_1)$, while it is braking for $t \in (t_2 : T)$. Test trajectories start at the same time instant, but they are translated each other, due to the difficulty to repeat exactly the same movement twice. However, two movements are equivalents.

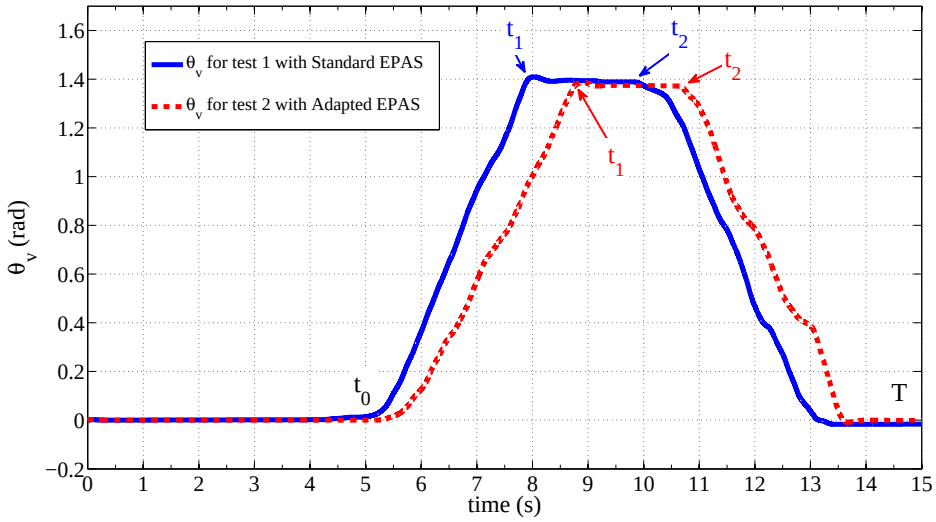


**Figure 5.25** – Profile of the trajectory that the operator makes on the steering wheel to test the steering assistance in the scenario of a parking. The solid (blue) trajectory is obtained during the test 1, when the standard steering assistance is activated. The dashed (red) trajectory is obtained during the test 2, when the modified steering assistance is activated. Despite the time traslation, the two movements are equivalents.

Experimental results concerning the driver's energy and power validate what it has been shown in simulation. Driver's energy is shown in Fig. 5.26, while the driver's power is shown on the steering wheel plane in Fig. 5.27.

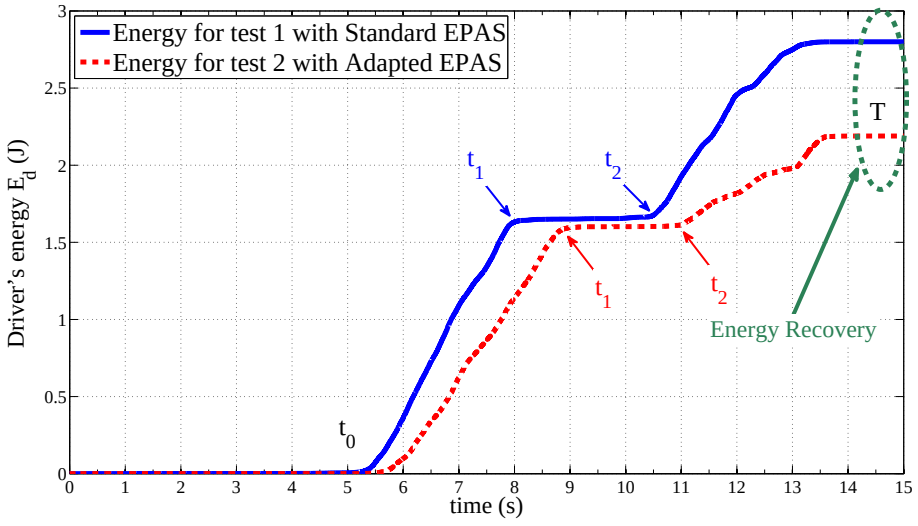


**Figure 5.26** – Profile of the driver's energy produced during the tests.

In Fig. 5.26, let us remark the diminishing of the driver's energy during the test 2, when the adapted steering assistance is active. This results confirm what it has been shown in

simulation and opens the perspective toward the applicability of the proposed assistance.

In Fig. 5.27, driver's power is shown during 2 parts of the movement : from 0 ° to 90 ° the movement is motor and is in the same direction as the bias, so the assistance does not compensate. When the movement is in the opposite sense despite the disturb, the assistance helps to diminish the steering power. The assistance brings to a global diminishing in terms of driver's power and this experimental test confirms what it has been shown in simulation.
Let us also remark that the magnitude of the power calculated during the experimental test is compatible with that one obtained in simulation.

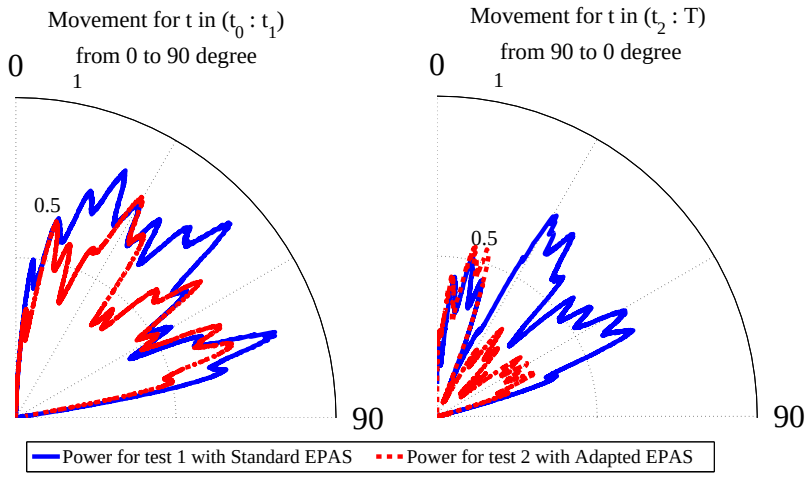


**Figure 5.27** – Driver's power during the experiment tests.

### 5.6.2.2 Cruise control

Test concerning the cruise control scenario implies that the operator is sit down and tries to drive with only one upper limb for a sufficiently long time duration. During this test nine EMG signals of the muscles of the upper limb are recorded with the method Seniam.

Test subject is the same, that has been introduced in the estimation procedure in Paragraph5.6.1. Choice of the muscles of his right upper limb has been done keeping into account experiments in [28]. The activity of the following muscles is recorded :
– biceps
– anterior and posterior triceps
– anterior, middle and posterior deltoid
– sternal and clavicular pectoralis
– teres

Time and frequency domain analysis is done on these recording, because an increasing of the mean root mean square value of the EMG with a constant effort implies an increasing of the muscular activity. Moreover, the displacement of the median frequency toward low frequencies shows the appearing of the muscular fatigue.

The following protocol is applied to perform this test :

1. Calibration tests : the subject is sit down front to the steering wheel and he is required first to pull and the to push the fixed ball for 5 s, in order to record the Maximum Voluntary Contraction (MVC) of his muscles.
2. Co-contraction tests : the subject is in the same position as in the previous test and he has to contract muscles of his upper limb, in order to provide a co-contraction measure.
3. The subject drives for 10 min with the hand on the ball on the steering wheel and the standard power steering assistance, that is active.
4. The subject is relaxed for 30 min.
5. Recalibration and co-contraction tests are performed, in order to verify that the subject may reach the same MVC as at the beginning of the experiment.
6. The subject drives for 10 min with the hand on the ball on the steering wheel and the modified steering assistance.

Most significant results concern the activity of the anterior deltoid. In Fig. 5.28, the recording of the EMG signals is shown during for the test with the standard and the adapted assistance. To perform the analysis, 3 time intervals of the signals are selected at the beginning, the middle and the end of the experiments.

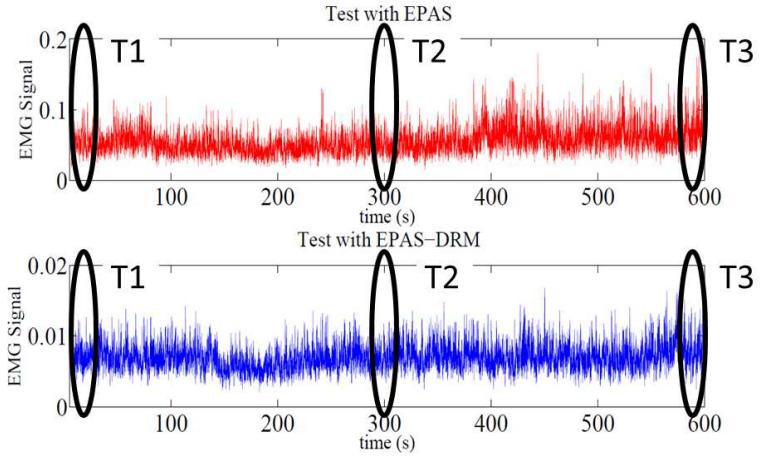


**Figure 5.28** – EMG signals of the anterior deltoid. Time $T_1$, $T_2$, $T_3$ show the interval of the signal where post-processing analysis are performed.

For the selected signals, the mean and the standard deviation are calculated and shown in Fig. **??**. In this figure, it is possible to note the difference in terms of amplitude of the signal : muscular activity with the standard assistance is about 10 times stronger than with the adapted one. In both cases, the increasing of the mean value of the EMG signal under a constant effort is shown, but the slope of the increasing is higher in the case of the standard assistance w.r.t. the adapted one.

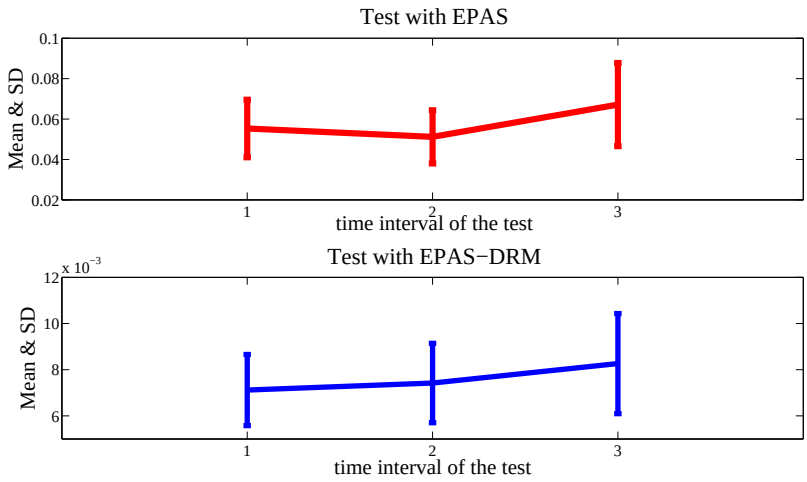


**Figure 5.29** – Evolution of the mean and the standard deviation of the EMG signal of the anterior deltoid.

The frequency analysis is also trained out on the same intervals of the EMG and it is

shown in Fig. **??**. The displacement of the median frequency toward low frequencies shows the appearing of the muscular fatigue in the subject, when he drives with the standard assistance. This is not the case of the test with the adapted one, where the median frequency is almost constant.

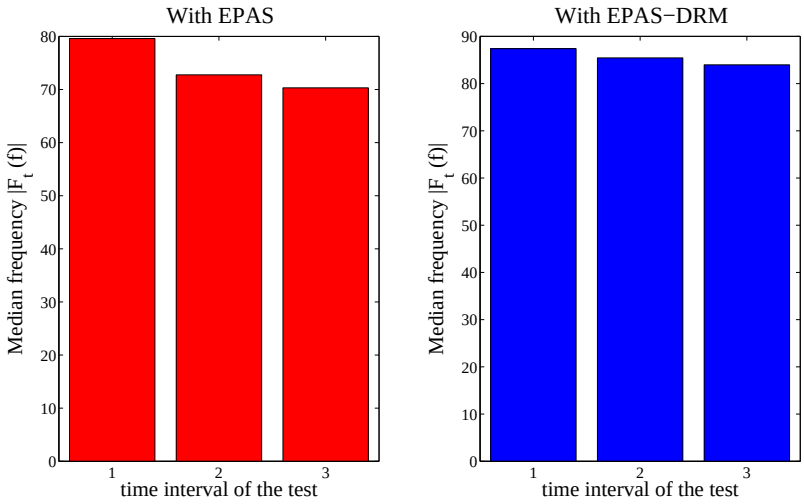


**Figure 5.30** – Evolution of the median frequency of the EMG signal of the anterior deltoid.

As concluding remark, it is possible to say that this test has not a statistical value, but it shows a clear energy recovery and fatigue reduction using the modified assistance.

#### 5.6.2.3 Obstacle avoidance

To test the scenario of an obstacle avoidance, the operator executes a step-wise reference trajectory on the steering wheel with the vehicle at 30 $\mathrm{km\,h^{-1}}$. We ask to the operator to turn the steering wheel from 0 ° to 90 ° in anti-clockwise, then to keep the position for 4 s and finally to bring back the ball to its initial position.

As in the case of the parking manoeuvre, this test is repeated twice. The first one, the operator makes to movement with the support of the standard steering assistance of Eqs. (1.2.2) and (1.2.3). The second one, the modified steering assistance of Eqs. (4.3.17) and (4.3.18) is used to help the movement.

On the experimental validation, this phenomenon is not evident, so as it happens in simulation. The requirement to reproduce exactly the same movement over a long period introduce many difficulties on the experiment and the driver's behaviour is probably different w.r.t. the model used in simulation. Anyway, it is possible to find some cases where the improvement due to the assistance contributes to improve driving precision. This is the case of the part of the experiment shown in Fig. 5.31. During all the test, it

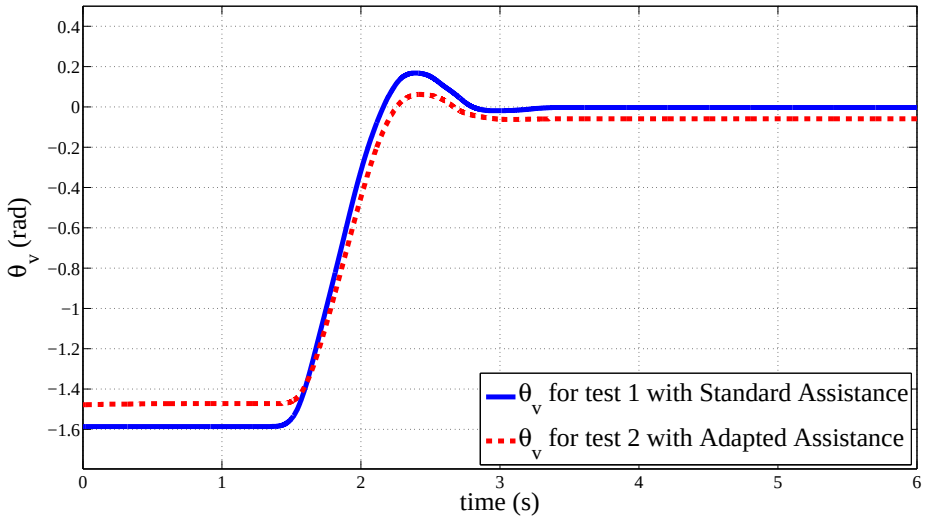


**Figure 5.31** – Part of the trajectories applied on HIL setup to test the obstacle avoidance, when the adapted steering assistance provides an improvement into the tracking control.

has been possible to recover a part where oscillations due to the asymmetry of the driver have been attenuated with the introduction of the adapted assistance.

## 5.7 Concluding remarks

This chapter ends the thesis, showing the experimental validation of all models and controls shown in this thesis.

The oscillation annealing control has been tested on the experimental setup, showing a similar behaviour w.r.t. the simulation results. Oscillations of the steering column can be eliminated through the use of the state controller.

The experimental validation of the torque observer shows that the observation error is negligible even in presence of real signals and the measurement error does not affect performances of the observer. Moreover, a comparison between the simulated tire-road friction torque and the real one shows that the model reproduces perfectly the real one. This element validates the mathematical model used in simulation.

An experimental procedure to estimate the mass parameter of the upper limb has been developed. Average results of this procedure are in accord with those obtained using the biomechanical model of the upper limb. The estimated value of the mass parameter is used as input to test the modified steering assistance.
Results concerning the parking manoeuvre show that it is possible to diminish the driver's energy during the manoeuvre even on the experimental setup. Moreover, preliminary

tests about the obstacle avoidance show that it is possible to obtain a better driving control thanks to the proposed assistance. These results validate the simulation results and proof the applicability of the proposed assistance.

# Chapitre 6

# General conclusions and perspectives

## 6.1 Main contributions

This thesis concerns the study and the analysis of EPAS system through the development of a general methodology to adapt this system to drivers with reduced mobility. The objectives are to improve driving comfort and control and to reduce driver's fatigue and strain. The main contributions are :

– The design of a general control architecture for the EPAS systems. Main advantage of this architecture are the flexibility and the possibility to adapt it to a various class of vehicles without hardware modifications.
– The introduction of a realistic model of the tire-road friction torque, with an original non-linear dependency of the friction from the velocity of the vehicle. This model has been validated experimentally, proving its extreme accuracy, which makes it suitable for simulation of vehicle dynamics.
– The synthesis of an optimal state-control to delete oscillations of the steering column in open loop and of a torque observer. This observer retrieves information about state-variables of the system and about the two exogenous inputs acting on it. This information can be used as an input for the EPAS system, thus avoiding the introduction of expensive torque sensors.
– The theoretical justification the standard booster curves, through a bio-mechanical study of the human movement. Indeed, hydraulic mimic standard booster curves turn out to be the solution of an optimization problem, minimizing the jerk criterion coupled with the Stevens' power law.
– A general methodology to adapt the standard steering assistance to drivers with reduced mobility, based on a bio-mechanical study of human movement. This methodology has been tested in the case of drivers affected by asymmetry of the upper limb.

– The experimental validation of the general control architecture on a HIL setup. Experimental results are in accordance with simulation results and they show the applicability of the control architecture on a real experimental setup.

## 6.2 Perspectives

As a perspective of these results, many interesting points may be exploited. Among others, according to the author, the followings seem to be of great interest :

– A better model for the upper limb. Our methodology to estimate the mass parameter of the upper limb assumes that the driver has the upper limb completely relaxed front to the steering wheel. Even under this strong assumption, the experimental results show a nice accordance with the model, but new more realistic models can lead to improved accuracy.
– Extension of the methodology to muscular asymmetries. In this thesis, only the gravitational asymmetry is taken into account. According to the author, the proposed assistance strategy can be applied also in the case of muscular asymmetry. This requires a finer bio-mechanical model of the upper limb and a careful experimental tuning of its parameters. Toward this goal, the characterization of the contribution of each upper limb to the resulting driver's exerted torque should be done. Upper limbs can be considered as a system agonist-antagonist w.r.t. the axis of the steering wheel. It is possible to make the assumption that the nervous system controls this system as the agonist-antagonist torques around the articulation. This model can be validated experimentally with EMG signals coupled with torque and force measures on the HIL setup.
– An extensive campaign of tests involving a large number of people, both healthy and with reduced mobility. These tests can be performed on the HIL setup which has been developed in this thesis. The test campaign would provide stronger validation of the proposed method and lead to its full acceptance in the community. A cross-validation with qualitative criteria (i.e. surveys about the steering feel during test with the steering assistance) can be also done.
– The implementation of the proposed steering assistance on car prototypes driving on the road, where the influence of the tire-road friction torque and the dry friction torque of the steering column may affect the driving steering feel.

# Annexe A

## A.1 Linear bicycle model

The model under consideration is well known in literature ([2], [60], [76]) and is based on the following assumptions :

– Linear lateral tire friction curve, i.e. :

$$\begin{cases} F_{tyf} = C_{yf}\beta_f \\ F_{tyr} = C_{yr}\beta_r \end{cases} \tag{A.1.1}$$

where $C_{yf}$ and $C_{yr}$ are the linear stiffness of the lateral tire characteristics at the front and rear, respectively.

– Small slip angles ($\beta_f$ and $\beta_r$) :

$$\begin{cases} \beta_f = \theta_v - \beta - \frac{l_f\dot{\psi}}{v} \\ \beta_r = \beta + \frac{l_r\dot{\psi}}{v} \end{cases} \tag{A.1.2}$$

where $\dot{\psi}$ denotes the vehicle yaw rate, $\beta_f$ and $\beta_r$ denote the slip angles at the front and rear, while $\theta_v$ is the steering angle of the front wheel.

Under these assumptions, the linearized model is given by (where $V$ is a model parameter) :

$$\begin{bmatrix} \ddot{\psi} \\ \dot{\beta} \end{bmatrix} = \begin{bmatrix} -\frac{l_f^2 C_{yf} + l_r^2 C_{yr}}{I_z V} & \frac{l_r C_{yr} - l_f C_{yf}}{I_z} \\ -1 + \frac{l_r C_{yr} - l_f C_{yf}}{MV^2} & -\frac{(C_{yf} + C_{yr})}{MV} \end{bmatrix} \begin{bmatrix} \dot{\psi} \\ \beta \end{bmatrix} + \begin{bmatrix} \frac{l_f C_{yf}}{I_z} \\ \frac{C_{yf}}{Mv} \end{bmatrix} \theta_v \tag{A.1.3}$$

Note that this model is not defined for speeds of the vehicle that are null. This is not a problem, because the Self-Alignment torque appears at high speeds. The values of the parameters are given in Table A.1.

## A.2 Tables of parameters

This section shows summarizing tables of all parameters used in this thesis. Table A.1 reports parameters of the EPAS system, while Table A.2 describes parameters of the tire-road friction models.

| Symbol | Description | Value |
|---|---|---|
| $B_0$ | Wheel real viscosity of the HIL setup | 0.039 $\mathrm{N\,m\,rad^{-1}\,s^{-1}}$ |
| $B_m$ | Motor shaft viscosity | 0.0032 $\mathrm{N\,m\,rad^{-1}\,s^{-1}}$ |
| $B_v$ | Steering wheel viscosity | 0.06 $\mathrm{N\,m\,rad^{-1}\,s^{-1}}$ |
| $C_{yf}$ | Front axle tire cornering | 28559 $\mathrm{N\,rad^{-1}}$ |
| $C_{yr}$ | Rear axle tire cornering | 40698 $\mathrm{N\,rad^{-1}}$ |
| $I_z$ | Vehicle inertia | 1975 $\mathrm{kgm^2}$ |
| $K_p$ | Proportional gain | 4 N |
| $k$ | Column stiffness | 100 $\mathrm{N\,m\,rad^{-1}}$ |
| $g$ | Gravitational constant | 9.81 $\mathrm{m/s^2}$ |
| $J_0$ | Wheel real inertia of the HIL setup | 0.0303 $\mathrm{kgm^2}$ |
| $J_c$ | Column inertia | 0.04 $\mathrm{kgm^2}$ |
| $J_m$ | Motor inertia | 0.0004 $\mathrm{kgm^2}$ |
| $J_v$ | Steering wheel inertia | 0.05 $\mathrm{kgm^2}$ |
| $J_w$ | Rack inertia | 0.000784 $\mathrm{kgm^2}$ |
| $l_f$ | Distance from the center of gravity to the front axle | 1.15 m |
| $l_r$ | Distance from the center of gravity to the rear axle | 1.38 m |
| $M$ | Vehicle total mass | 1621 kg |
| $N_1$ | Steering column-wheels gear ratio | 13.67 |
| $N_2$ | Motor-steering column gear ratio | 17 |
| $\Phi$ | Caster angle | 20 ° |
| $r_{sw}$ | Radius of the steering wheel | 0.18 m |
| $r$ | Radius of the road-wheel | 0.38 m |
| $T_d$ | Time constant of the derivative action | 0.04 s |
| $T_i$ | Time constant of the integral action | 1.2 s |
| $\tau_{\max}$ | Upper saturation limit | +10 N m |
| $\tau_{\min}$ | Lower saturation limit | -10 N m |

**Table A.1** – Parameters of the EPS system, the bicycle model and the HIL setup

| Symbol | Description | Value |
|---|---|---|
| $\alpha_1$ | Initial slope of the trapezoidal load distribution | 630000 $\mathrm{N\,m^{-1}}$ |
| $\alpha_2$ | Final slope of the trapezoidal load distribution | -55000 $\mathrm{N\,m^{-1}}$ |
| $\beta_2$ | Intercept of the trapezoidal load distribution | 8260 N |
| $\gamma$ | Steady-state constant | 1 |
| $F_{max}$ | Max value of normal load distribution | 1900 N |
| $F_n$ | Normal value of normal load distribution | 249.37 N |
| $\dot{\phi}_s$ | Stribeck angular relative velocity | 74 $\mathrm{rad\,s^{-1}}$ |
| $L$ | Patch length | 0.15 m |
| $\mu_{kx}$ | Kinetic friction coeff. x-axis | 0.75 |
| $\mu_{ky}$ | Kinetic friction coeff. y-axis | 0.75 |
| $\mu_{kz}$ | Kinetic friction coeff. z-axis | 0.76 |
| $\mu_{sx}$ | Static friction coeff. x-axis | 1.35 |
| $\mu_{sy}$ | Static friction coeff. y-axis | 1.40 |
| $\mu_{sz}$ | Static friction coeff. z-axis | 0.91 |
| $\sigma_{0y}$ | Normalized rubber stiffness (Self-Align.) | 6000 $\mathrm{m^{-1}}$ |
| $\sigma_{1y}$ | Normalized rubber damping (Self-Align.) | 0.3568 $\mathrm{s\,m^{-1}}$ |
| $\sigma_{2y}$ | Normalized viscous relative damping (Self-Align.) | 0.0001 $\mathrm{s\,m^{-1}}$ |
| $\sigma_{0z}$ | Normalized rubber stiffness (Stick.) | 20 $\mathrm{m^{-1}}$ |
| $\sigma_{1z}$ | Normalized rubber damping (Stick.) | 0.0023 $\mathrm{s\,m^{-1}}$ |
| $\sigma_{2z}$ | Normalized viscous relative damping (Stick.) | 0.0001 $\mathrm{s\,m^{-1}}$ |
| $\sigma_0$ | Rubber longitudinal stiffness (Dahl) | 40 $\mathrm{m^{-1}}$ |
| $\sigma_2$ | Viscous relative damping (Dahl) | 0.0018 $\mathrm{s\,m^{-1}}$ |
| $v_s$ | Stribeck linear relative velocity | 3.96 $\mathrm{m\,s^{-1}}$ |
| $\zeta_L$ | Left patch length | 0.0030 m |
| $\zeta_R$ | Right patch length | 0.1155 m |

**Table A.2** – Constant parameters of the friction models (Self-Alignment and Sticking models and Dahl's model)

## A.3 Analytic solution of the Dahl's model

To evaluate the analytic solution of the Dahl's model, let us consider Eq. (4.2.2) and let us make the hypothesis to have a positive speed signal during the time interval $t \in [0, t_1]$. At the time $t = 0$, the corresponding value for the angle is $\theta(0) = \theta_0$. This implies that $\text{sgn}\left(\dot{\theta}\right) = +1$ in Eq. (4.2.2) for $\theta \in [\theta_0, \theta]$. Let us make also the hypothesis to start from null initial conditions. Under these constraints, the following differential equation needs to be solved

$$\frac{\mathrm{d}F}{\mathrm{d}\theta} = \sigma_0 \left(1 - \frac{F}{F_c}\right) \tag{A.3.1}$$

with the initial condition $F(\theta_0) = 0$.
If both terms of Eq. (A.3.1) are divided by $\left(1 - \frac{F}{F_c}\right)$ and $F_c$, the following primitive is obtained

$$\frac{-\frac{1}{F_c}\left(\frac{\mathrm{d}F}{\mathrm{d}\theta}\right)}{\left(1 - \frac{F}{F_c}\right)} = -\frac{\sigma_0}{F_c} \tag{A.3.2}$$

To obtain the analytic solution of Eq. (A.3.2) for positive speeds, let us integrate both terms during the interval $\theta \in [\theta_0, \theta(t)]$

$$\int_{\theta_0}^{\theta(t)} \frac{-\frac{1}{F_c}\frac{\mathrm{d}F}{\mathrm{d}\theta}}{\left(1 - \frac{F}{F_c}\right)} \mathrm{d}\theta = -\frac{\sigma_0}{F_c} \int_{\theta_0}^{\theta(t)} \mathrm{d}\theta \tag{A.3.3}$$

The result of this integral is

$$\ln\left|1 - \frac{F(\theta(t))}{F_c}\right| - \ln\left|1 - \frac{F(\theta_0)}{F_c}\right| = -\frac{\sigma_0}{F_c}\left(\theta(t) - \theta_0\right) \tag{A.3.4}$$

By substituting the initial condition $F(\theta_0) = 0$, it is easily to obtain the solution for positive speeds

$$F(\theta(t)) = F_c \left[1 - \exp^{-\frac{\sigma_0}{F_c}(\theta(t) - \theta_0)}\right] \tag{A.3.5}$$

At the time instant $t = t_1$, the speed changes in sign and becomes negative ($\text{sgn}\left(\dot{\theta}\right) = -1$ in Eq. (4.2.2)) during the time interval $t \in [t_1, t_2]$. To guarantee the continuity of the function, it is required that the initial condition corresponds to the last values assumed from $F(\theta(t))$ during the interval $t \in [0, t_1]$, i.e. $F(\theta(t_1^-)) = F(\theta(t_1^+))$.
Under these hypothesis, the new Cauchy problem to solve is :

$$\frac{\mathrm{d}F}{\mathrm{d}\theta} = \sigma_0 \left(1 + \frac{F}{F_c}\right) \tag{A.3.6}$$

$$F(\theta(t_1^-)) = F(\theta(t_1^+)) \tag{A.3.7}$$

To solve this problem, let us proceed as for Eqs. (A.3.2) and (A.3.3) and let us integrate for $\theta \in [\theta(t_1), \theta(t)]$, as follows :

$$\int_{\theta(t_1)}^{\theta(t)} \frac{\frac{1}{F_c}\frac{\mathrm{d}F}{\mathrm{d}\theta}}{\left(1+\frac{F}{F_c}\right)}\mathrm{d}\theta = \int_{\theta(t_1)}^{\theta(t)} \frac{\sigma_0}{F_c}\mathrm{d}\theta \tag{A.3.8}$$

The solution of this integral is :

$$\ln\left|1+\frac{F(\theta(t))}{F_c}\right| - k_1 = \frac{\sigma_0}{F_c}(\theta(t)-\theta(t_1)) \tag{A.3.9}$$

where $k_1$ is a constant, depending from the initial conditions. By inverting this equation, it is possible to obtain :

$$F(\theta(t)) = F_c\left[-1+\exp^{\frac{\sigma_0}{F_c}(\theta(t)-\theta(t_1))}\cdot\exp^{k_1}\right] \tag{A.3.10}$$

To determine the constant $k_1$, let us introduce the initial condition $F(\theta(t_1^-)) = F(\theta(t_1^+))$ :

$$F(\theta(t_1^-)) = F_c\left[1-\exp^{-\frac{\sigma_0}{F_c}\theta(t_1)}\right] \tag{A.3.11}$$

$$F(\theta(t_1^+)) = F_c\left[-1+\exp^{\frac{\sigma_0}{F_c}(\theta(t_1)-\theta(t_1))}\cdot\exp^{k_1}\right] \tag{A.3.12}$$

It follows :

$$F_c\left[1-\exp^{-\frac{\sigma_0}{F_c}\theta(t_1)}\right] = F_c\left[-1+\exp^{k_1}\right] \tag{A.3.13}$$

By solving for $k_1$, it results :

$$k_1 = \ln\left[2-\exp^{-\frac{\sigma_0}{F_c}\theta(t_1)}\right] \tag{A.3.14}$$

So the solution for negative speeds is :

$$F(\theta(t)) = F_c\left[-1+\exp^{\frac{\sigma_0}{F_c}(\theta(t)-\theta(t_1))}\cdot\exp^{\ln\left[2-\exp^{-\frac{\sigma_0}{F_c}\theta(t_1)}\right]}\right] \tag{A.3.15}$$

By rearranging all terms, this expression can be simplified as follows :

$$F(\theta(t)) = F_c\left[-1+2\exp^{\frac{\sigma_0}{F_c}(\theta(t)-\theta(t_1))}-\exp^{\frac{\sigma_0}{F_c}(\theta(t)-2\theta(t_1))}\right] \tag{A.3.16}$$

Let us make the hypothesis that the speed changes in sign and becomes positive during the time interval $t \in [t_2, t_f]$, in this way it is possible to find the analytic solution $F(\theta)$ for this last interval, by repeating the same steps as for the previous cases. In this case, the boundary condition is $F(\theta(t_2^-)) = F(\theta(t_2^+))$, so following Cauchy problem needs to be solved :

$$\frac{\mathrm{d}F}{\mathrm{d}\theta} = \sigma_0\left(1-\frac{F}{F_c}\right) \tag{A.3.17}$$

$$F(\theta(t_2^-)) \;=\; F(\theta(t_2^+)) \tag{A.3.18}$$

Let us proceed as in previous cases and let us integrate the primitive between $[\theta_2, \theta(t)]$ :

$$\int_{\theta_2}^{\theta(t)} \frac{-\frac{1}{F_c}\frac{\mathrm{d}F}{\mathrm{d}\theta}}{\left(1-\frac{F}{F_c}\right)}\mathrm{d}\theta = -\frac{\sigma_0}{F_c}\int_{\theta_2}^{\theta(t)} \mathrm{d}\theta \tag{A.3.19}$$

The following analytic solution is obtained

$$F(\theta(t)) = F_c\left[1-\exp^{-\frac{\sigma_0}{F_c}(\theta(t)-\theta(t_2))}\cdot\exp^{k_2}\right] \tag{A.3.20}$$

The constant $k_2$ can be determined by introducing the boundary condition $F(\theta(t_2^-)) = F(\theta(t_2^+))$ :

$$F(\theta(t_2^-)) = F_c\left[-1+2\exp^{\frac{\sigma_0}{F_c}(\theta(t_2)-\theta(t_1))}-\exp^{\frac{\sigma_0}{F_c}(\theta(t_2)-2\theta(t_1))}\right] \tag{A.3.21}$$

$$F(\theta(t_2^+)) = F_c\left[1-\exp^{-\frac{\sigma_0}{F_c}(\theta(t_2)-\theta(t_2))}\cdot\exp^{k_2}\right] \tag{A.3.22}$$

It follows :

$$F_c\left[1-\exp^{k_2}\right] = F_c\left[-1+2\exp^{\frac{\sigma_0}{F_c}(\theta(t_2)-\theta(t_1))}-\exp^{\frac{\sigma_0}{F_c}(\theta(t_2)-2\theta(t_1))}\right] \tag{A.3.23}$$

From Eq. (A.3.23) the following expression for the constant $k_2$ can be obtained

$$k_2 = \ln\left[2-2\exp^{-\frac{\sigma_0}{F_c}(\theta(t_2)-\theta(t_1))}+\exp^{\frac{\sigma_0}{F_c}(\theta(t_2)-2\theta(t_1))}\right] \tag{A.3.24}$$

Let us substitute Eq. (A.3.24) in Eq. (A.3.20) and let us simplify, in this way, it is possible to get the solution for the friction torque when the speed is positive and the initial condition is different from zero :

$$F(\theta(t)) = F_c\Big[1-2\exp^{-\frac{\sigma_0}{F_c}(\theta(t)-\theta(t_2))}+2\exp^{-\frac{\sigma_0}{F_c}(\theta(t)+\theta(t_1)-2\theta(t_2))}-\exp^{-\frac{\sigma_0}{F_c}(\theta(t)+2\theta(t_1)-2\theta(t_2))}\Big] \tag{A.3.25}$$

## A.4 Pseudo-Code of the dichotomy loop

This Section shows the dichotomy loop used in Chapter 4 to find the optimal time instant that guarantees a null driver's torque at the final time.

```
%epsilon = 0.005; %precision of the optimization
%Tmin = Tfin/2; %definition of the first interval
%Tmax = Tfin;
%T21 = (Tmin+Tmax)/2;
%t = T21;
%solve optimization problem at time t = T21
%save fval_1, value of the cost function I(t = T21)
%save the solution of the problem coeff_1
% while (Tmax - Tmin) > epsilon
%  fval_1
%  coeff_1
%  %definition of the second interval
%  T22 = (3*Tmin + Tmax)/4;
%  t = T22;
%  solve optimization problem at time t = T22
%save fval_2, value of the cost function I(t = T22)
%save the solution of the problem coeff_2
%%definition of the third interval
%T23 = (Tmin + 3*Tmax)/4;
%t = T23;
%solve optimization problem at time t = T23
%save fval_3, value of the cost function I(t = T23)
%save the solution of the problem coeff_3
%%search for the minimum cost function over 3 intervals
%if fval_1 == min([fval_1, fval_2, fval_3], [], 2)
% Tmin = T22;
% Tmax = T23;
% coeff = coeff_1;
%elseif fval_2 == min([fval_1, fval_2, fval_3], [], 2)
% Tmax = T21;
% T21 = T22;
% fval_1 = fval_2;
% coeff_1 = coeff_2;
%else
% Tmin = T21;
% T21 = T23;
% fval_1 = fval_3;
% coeff_1 = coeff_3;
%  end
%end
%
```

# Bibliographie


[1] T. Acarman, K.A. Redmill, and U. Ozguner. A robust controller design for drive by wire hydraulic power steering system. In *Proceedings of American Control Conference*, volume 3, pages 2522–2527, 2002.

[2] J. Ackermann and D. Forschungsanstalt. Yaw disturbance attenuation by robust decoupling of car steering. *Control Engineering Practice*, 5 :1131–1136, 1996.

[3] I. L. Ashkenas and D. T. McRuer. A Theory of Handling Qualities Derived from Pilot-Vehicle System Considerations. *Aerospace Engineering*, 21 :60–102, 1962.

[4] J. Awrejcewicz and P. Olejnik. Analysis of Dynamic Systems With Various Friction Laws. *Applied Mechanics Reviews*, 2005.

[5] Armstrong-Hèlouvry B., P. Dupont, and C. Canudas-De-Wit. A survey of models, analysis tools and compensation methods for the control of machines with friction. *Automatica*, 30(7) :1083–1138, 1994.

[6] E. Bakker, L. Nyborg, and Pacejka H. Tyre modelling for use in vehicle dynamics studies. *SAE Paper*, 1987.

[7] G.P. Bertollini and R.M. Hogan. Applying driving simulation to quantify steering efforts preference as a function of vehicle speed. *SAE Paper*, 1999.

[8] D. P. Bertsekas. *Nonlinear Programming*. Athena Scientific, 2nd edition, 1999.

[9] A. Biess, D. G. Liebermann, and T. Flash. A computational model for redundant human three-dimensional pointing movements : integration of independent spatial and temporal motor plans simplifies movement dynamics. *The Journal of Neuroscience*, 27(48) :13045–13064, 2007.

[10] B. Bigland-Ritchie and J. J. Woods. Changes in muscle contractile properties and neural control during human muscular fatigue. *Muscle and Nerve*, 7(9) :691–699, 1984.

[11] S. Bittanti. *Identificazione dei modelli e controllo adattativo*. Pitagora, 2000.

[12] P.A. Bliman, T. Bonald, and M. Sorine. Hysteresis operators and tyre friction models application to vehicle dynamic simulation. In *Proceedings of ICIAM*, July 1995.

[13] P.A. Bliman and M. Sorine. A system-theoretic approach of systems with hysteresis. application to friction modelling and compensation. In *Proceedings of European Control Conference*, pages 1844–1849, Sept. 1993.

[14] P.A. Bliman and M. Sorine. Easy-to-use realistic dry friction models for automatic control. In *Proceedings of European Control Conference*, pages 3788–3794, Sept. 1995.

[15] A.W. Burton. Innovation drivers for electric power-assisted steering. *IEEE Control Systems*, 23 :30–39, 2003.

[16] F.M.M.O. Campos and J.M.F. Calado. Approaches to human arm movement control - A review. *Annual reviews in control*, 33(1) :69–77, 2009.

[17] C. Canudas-De-Wit. Comments on "A new model for control of systems with friction". *IEEE Transactions on Automatic Control*, 43 :1189–1190, 1998.

[18] C. Canudas-De-Wit. Fun-To-Drive By Feedback. In *Proceedings of 44th IEEE Conference on Decision and Control and European Control Conference (CDC-ECC)*, pages 1–24, Dec. 2005.

[19] C. Canudas-De-Wit, X. Claeys, and H. Bechart. Stability analysis via passivity of the lateral actuator dynamics of a heavy vehicle. In *Proceedings of IEEE International Conference on Control Applications*, pages 1371–1376, 1999.

[20] C. Canudas-De-Wit, S. Guegan, and A. Richard. Control design for an electro power steering system : Part I : The reference model. In *Proceedings of European Control Conference*, Sept. 2001.

[21] C. Canudas-De-Wit, S. Guegan, and A. Richard. Control design for an electro power steering system : Part II : The control design. In *Proceedings of European Control Conference*, Sept. 2001.

[22] C. Canudas-De-Wit, H. Olsson, K.J. Astrom, and P. Lischinsky. A new model for control of systems with friction. *IEEE Transactions on Automatic Control*, 40 :419–425, Mar. 1995.

[23] C. Canudas-De-Wit, P. Tsiotras, E. Velenis, M. Basset, and G. Gissinger. Dynamic friction models for road/tire longitudinal interaction. *Vehicle System Dynamics*, 39(3) :189–226, 2003.

[24] R.C. Chabaan. Optimal control and gain scheduling of electrical power steering systems. In *Proceedings of IEEE Conference of Vehicle Power and Propulsion*, pages 53–59, Sept. 2009.

[25] X. Chen, X. Chen, and K. Li. Robust control of electric power-assisted steering system. In *Vehicle Power and Propulsion, 2005 IEEE Conference*, pages 473–478, 2005.

[26] Y. Chunfang, W. Shaohua, and Z. Jinbo. Flexible pid control design in assistance condition of automotive EPS system. In *International Forum on Computer Science-Technology and Applications*, volume 2, pages 222–225, 2009.

[27] X. Claeys, C. Canudas-De-Wit, and Bechart H. Modeling and control of steering actuator for heavy duty vehicle. In *Proceedings of European Control Conference*, 1999.

[28] D. J. Cole, A. J. Pick, and A. M. C. Odhams. Predictive and linear quadratic methods for potential application to modelling driver steering control. *Vehicle System Dynamics*, 44(3) :259–284, 2006.

[29] M. Copelli, A. C. Roque, R. F. Oliveira, and O. Kinouchi. Physics of psychophysics : Stevens and Weber-Fechner laws are transfer functions of excitable media. *Physical Review E*, 2002.

[30] P.R. Dahl. A solid friction model. *Space and Missile Systems Organization Air Force Systems Command*, May 1968.

[31] P.R. Dahl. Solid friction damping of mechanical vibrations. *AIAA Journal*, 14 :1675–1682, 1976.

[32] P.R. Dahl and J.H. Ly. Dynamic hysteresis modeling. In *Proceedings of AIAA Conference on Modeling and Simulation Technologies*, pages 14–17, Aug. 2000.

[33] J. Deur, J. Asgari, and D. Hrovat. A dynamic tire friction model for combined longitudinal and lateral motion. In *Proceedings of ASME International Mechanical Engineering Congress and Exposition*, pages 1–8, 2001.

[34] R. H. Fitts. Cellular mechanisms of muscle fatigue. *Physiological Reviews*, 74(1) :49–94, 1994.

[35] T. Flash and N. Hogan. The coordination of arm movements : an experimentally confirmed mathematical model. *The Journal of Neuroscience*, 5(7) :1688–1703, 1985.

[36] B. W. Fling, C. A. Knight, and G. Kamen. Relationships between motor unit size and recruitment threshold in older adults : implications for size principle. *Experimental Brain Research*, 197(2) :125–133, 2009.

[37] M. Gafvert. Comparisons of two dynamic friction models. In *Proceedings of IEEE International Conference on Control Applications*, pages 386–391, Oct. 1997.

[38] G. Gim and P. E. Nikravesh. An analytical model of pneumatic tyres for vehicle dynamic simulations. Part I : pure slips. *International Journal of Vehicle Design*, 11(6) :589–618, 1990.

[39] K. Guo and H. Guan. Modelling of driver/vehicle directional control system. *Vehicle System Dynamics*, 22(3–4) :141–184, 1993.

[40] N. Hogan and D. Sternad. On rhythmic and discrete movements : reflections, definitions and implications for motor control. *Experimental Brain Research*, 181 :13–30, July 2007.

[41] W. Hoult and D. J. Cole. A neuromuscular model featuring co-activation for use in driver simulation. *Vehicle System Dynamics*, 46 :175–189, 2008.

[42] K. Ji Hoon and S. Jae Bok. Control logic for an electric power steering system using assist motor. *Mechatronics*, 12(3) :447–459, 2002.

[43] H. B. Jiang, J. B. Zhao, H. M. Liu, and L. Chen. Low-pass filter based on automotive EPS controller and comparative full-vehicle tests. In *Proceedings of Chinese Control and Decision Conference*, pages 4662–4665, July 2008.

[44] W. Jiang, C. Canudas-de Wit, O. Sename, and J. Dumon. A new mathematical model for car drivers with spatial preview. In *Proceedings of 18th IFAC World Congress*, 2011.

[45] Y. Jingang, L. Alvarez, and R. Horowitz. Adaptive emergency braking control with underestimation of friction coefficient. *IEEE Transactions on Control Systems Technology*, 10(3) :381–392, 2002.

[46] J.H. Johnson, S. Colodny, and D. Jackson. Human torque capability versus machine resistive torque for four eagle resistance machines. *Journal of Applied Sport Science Research*, 4(3) :83–87, 1990.

[47] R. Kalman. On the general theory of control systems. *IRE Transactions on Automatic Control*, 4(3) :110–110, 1959.

[48] R. Kalman. Mathematical description of linear dynamical systems. *Journal of the Society for Industrial and Applied Mathematics Series A Control*, 1(2) :1526–192, 1963.

[49] W. Kemmetmuller, A. Kugi, and S. Muller. Modeling and nonlinear control of an electrohydraulic closed-center power-steering system. In *Proceedings of 44th IEEE Conference on Decision and Control and European Control Conference (CDC-ECC)*, pages 5077–5082, 2005.

[50] W. Kemmetmuller, S. Muller, and A. Kugi. Mathematical modeling and nonlinear controller design for a novel electrohydraulic power-steering system. *IEEE/ASME Transactions on Mechatronics*, 12(1) :85–97, 2007.

[51] Khetisikho Agriculture info. Steering gear box. http ://khetisikho.com/ ?p=971, 2012.

[52] C.-J. Kim, J.-H. Jang, S.-K. Oh, J.-Y. Lee, C.-S. Han, and J. K. Hedrick. Development of a control algorithm for a rack-actuating steer-by-wire system using road information feedback. *Proceedings of the Institution of Mechanical Engineers, Part D : Journal of Automobile Engineering*, 222(9) :1559–1571, 2008.

[53] Kistler France. Kistler 4503A. http ://www.kistler.com/fr/en/product/torque/4503AxH., 2012.

[54] Kollmorgen. Servomotors. http ://www.kollmorgen.com/en-us/products/motors/servo/servomotors/, 2012.

[55] M. Kurishige, S. Wada, T. Kifuku, and N. Inoue. An analysis of a driver's control algorithm using neural network modelling. *SAE Technical Paper*, 1 :8–15, 2000.

[56] I.D. Landau and G. Zito. *Digital Control Systems : Design, Identification and Implementation*. Springer-Verlag, 2006.

[57] P.Y. Li and R. Horowitz. Control of smart exercise machines I. Problem formulation and nonadaptive control. *IEEE/ASME Transactions on Mechatronics*, 2(4) :237–247, Dec. 1997.

[58] P.Y. Li and R. Horowitz. Control of smart exercise machines II. Self-optimizing control. *IEEE/ASME Transactions on Mechatronics*, 2(4) :248–258, Dec. 1997.

[59] X. Li, X.-P. Zhao, and J. Chen. Controller design for electric power steering system using T-S fuzzy model approach. *International Journal of Automation and Computing*, 6(2) :198–203, 2009.

[60] S. Mammar and D. Koenig. Vehicle handling improvement by active steering. *Vehicle system dynamics*, 5 :211–242, 2002.

[61] A. Marouf, M. Djemai, C. Sentouh, and P. Pudlo. Driver torque and road reaction force estimation of an electric power assisted steering using sliding mode observer with unknown inputs. In *Proceedings of 13th International IEEE Conference on Intelligent Transportation Systems*, pages 354–359, 2010.

[62] A. Marouf, M. Djemai, C. Sentouh, and P. Pudlo. A new control strategy of an electric–power–assisted steering system. *IEEE Transactions on Vehicular Technology*, 61(8) :3574–3589, 2012.

[63] A. Marouf, M. Djemai, C. Sentouh, and P. Pudlo. Sensorless control of electric power assisted steering system. In *Proceedings of 20th Mediterranean Conference on Control Automation*, pages 909–914, 2012.

[64] A. Marouf, C. Sentouh, M. Djemai, and P. Pudlo. Control of an electric power assisted steering system using reference model. In *Proceedings of 50th IEEE Conference on Decision and Control and European Control Conference (CDC–ECC)*, pages 6684–6690, 2011.

[65] A. Marouf, C. Sentouh, M. Djemai, and P. Pudlo. Control of electric power assisted steering system using sliding mode control. In *Proceedings of 14th International IEEE Conference on Intelligent Transportation Systems*, pages 107–112, 2011.

[66] T. Meihua, P. Hingwe, and M. Tomizuka. Modeling and control of steering system of heavy vehicles for automated highway systems. *IEEE/ASME Transactions on Mechatronics*, 9(4) :609–618, 2004.

[67] W. Milliken. Merits of front, rear and four-wheel drive. *Race Car Vehicle Dynamics*, 1995.

[68] A. Modjtahedzadeh and R. A. Hess. A Model of Driver Steering Control Behavior for Use in Assessing Vehicle Handling Qualities. *Journal of Dynamic Systems, Measurement, and Control*, 115(3) :456–464, 1993.

[69] A. C. Newberry, M. J. Griffin, and M. Dowson. Driver perception of steering feel. *Proceedings of the Institution of Mechanical Engineers, Part D : Journal of Automobile Engineering*, 221(4) :405–415, 2007.

[70] K. Ohta, M. M. Svinin, Z. Luo, S. Hosoe, and R. Laboissière. Optimal trajectory formation of constrained human arm reaching movements. *Biological Cybernetics*, 91 :23–36, 2004.

[71] H. Pacejka and E. Bakker. The magic formula tyre model. In *Proceedings of 1st International Colloquium on Tyre Models for Vehicle Dynamics Analysis*, pages 1100–1105, Oct. 1991.

[72] H. Pacejka and E. Bakker. The Magic Formula Tyre Model. *Vehicle System Dynamics*, 21(1) :1–18, 1992.

[73] M. Parmar and J.Y. Hung. A sensorless optimal control system for an automotive electric power assist steering system. *IEEE Transactions on Industrial Electronics*, 51(2) :290–298, 2004.

[74] H. Peng. Evaluation of Driver Assistance Systems : A Human Centered Approach. In *Proceedings of 6th Symposium on Advanced Vehicle Control*, 2002.

[75] A. J. Pick and D. J. Cole. A mathematical model of driver steering control including neuromuscular dynamics. *Journal of Dynamic Systems, Measurement, and Control*, 130, 2008.

[76] C. Poussot-Vassal. *Commande robuste LPV multivariable de chassis automobile*. PhD thesis, Grenoble Institute of Technology, 2008.

[77] G. Prokop. Modeling human vehicle driving by model predictive online optimization. *Vehicle System Dynamics*, 35(1) :19–53, 2001.

[78] H.C. Qiu, Q. Zhang, J.F. Reid, and Wu D. Modelling and simulation of an electrohydraulic steering system. *International Journal of Vehicle Design*, 26 :161–174, 2001.

[79] E. Rabinowicz. The nature of the static and kinetic coefficients of friction. *Journal of Applied Physics*, pages 1373–1379, 1951.

[80] J. Richalet, A. Rault, J.L. Testud, and J. Papon. Model predictive heuristic control : Applications to industrial processes. *Automatica*, 14(5) :413–428, 1978.

[81] R. Rouhani and R.M. Mehra. Model algorithmic control : basic theoretical properties. *Automatica*, 18(4) :401–414, 1982.

[82] M. Sorine and J. Szymanski. A new dynamic multi degree of freedom tire model. *Transportation Systems*, 2000.

[83] N. Sugitani, Y. Fujuwara, K. Uchida, and M. Fujita. Electric power steering with h-infinity control designed to obtain road information. In *Proceedings of the American Control Conference*, volume 5, pages 2935–2939, 1997.

[84] L. Toulemon and S. Pennec. Combien de personnes résident seules en france ? *Population et Sociétés*, pages 1–6, Dec. 2011.

[85] H. Tsung Hsien, Y. Chih Jung, H. Shih Rung, H. Tsung Hua, and L. Ming Chih. Design of control logic and compensation strategy for electric power steering systems. In *Proceedings of IEEE Vehicle Power and Propulsion Conference*, pages 1–6, Sept. 2008.

[86] E. Velenis, P. Tsiotras, C. Canudas-De-Wit, and M. Sorine. Dynamic Tire Friction Models for Combined Longitudinal and Lateral Vehicle Motion. *Vehicle System Dynamics*, 43(1) :3–29, 2005.

[87] K. Walker-Bone, K. T. Palmer, I. Reading, D. Coggon, and C. Cooper. Prevalence and impact of musculoskeletal disorders of the upper limb in the general population. *Arthritis Care and Research*, 51(4) :642–651, 2004.

[88] J. Wang, Q. Wang, and J. Liqiang. Modeling and simulation studies on differential drive assisted steering for EV with four wheels independent drive. In *Proceedings of IEEE Vehicle Power and Propulsion Conference*, pages 1–7, Sept. 2008.

[89] G. N. Williams, M. J. Higgins, and M. D. Lewek. Aging skeletal muscle : Physiologic changes and the effects of training. *Physical Therapy*, 82(1) :62–68, 2002.

[90] D.A. Winter. *Biomechanics and Motor Control of Human Movement*. Wiley, 2009.

[91] L. Yao, J. Zhao, and J. Qian. An improved pseudo-random binary sequence design for multivariable system identification. In *The Sixth World Congress on Intelligent Control and Automation*, volume 1, pages 1768–1772, 2006.

[92] A.T. Zaremba, M.K. Liubakka, and R.M. Stuntz. Control and steering feel issues in the design of an electric power steering system. In *Proceedings of American Control Conference*, volume 1, pages 36–40, 1998.

[93] H. Zhang, Y. Zhang, J. Liu, J. Ren, and Y. Gao. Modeling and characteristic curves of electric power steering system. In *Proceedings of International Conference on Power Electronics and Drive Systems*, pages 1390–1393, Nov. 2009.

[94] W. Zhang and Q. Fan. Identification of abnormal driving state based on driver's model. In *Proceedings of International Conference on Control Automation and Systems*, pages 14–18, 2010.

[95] J.J. Zwislocki. *Stevens' Power Law*. Springer US, 2009.